STANDARD FORM 298

REPORT DOCUMENTATION PAGE

Form Approved
OMB NO. 0704-0188

1. AGENCY USE ONLY (Leave Blank)	2. REPORT DATE November 30, 2002	3. REPORT TYPE AND DATES COVERED 8/16/1998 - 8/16/2002 01 Sep 98 31 Aug 02

4. TITLE AND SUBTITLE
Experimental and Numerical Investigation of High-Speed High-Temperature Jet Interaction Flowfields

5. FUNDING NUMBERS
DAAG55-98-1-0479

6. AUTHOR(S) Rodney D. W. Bowersox

7. PERFORMING ORGANIZATION NAME(S) AND ADDRESS(ES)
The University of Alabama
Sponsored Research Office
P. O. Box 870104
Tuscaloosa, AL 35487-0104

8. PERFORMING ORGANIZATION REPORT NUMBER TAMU-HAL-2002-002

9. SPONSORING / MONITORING AGENCY NAME(S) AND ADDRESS(ES)

U. S. Army Research Office
P.O. Box 12211
Research Triangle Park, NC 27709-2211

10. SPONSORING / MONITORING AGENCY REPORT NUMBER

39115.1-EG

11. SUPPLEMENTARY NOTES
The views, opinions and/or findings contained in this report are those of the author(s) and should not be construed as an official Department of the Army position, policy or decision, unless so designated by other documentation.

12 a. DISTRIBUTION / AVAILABILITY STATEMENT

Approved for public release; distribution unlimited.

12 b. DISTRIBUTION CODE

13. ABSTRACT (Maximum 200 words)

An experimental analysis of the mean and turbulent flow properties for sonic and Mach 3 injection into a Mach 3 freestream was accomplished. The range of conditions included: MPR = 0.005-0.09, p_j / p_∞ = 0.6-19.0, T_j / T_∞ = 1.0-13.6, γ = 1.4 and 1.67, and p_{eb} / p_∞ = 0.19-6.15 (over, perfectly and underexpanded). Injection temperature had a small effect on the boundary layer separation distance. The effective backpressure was an accurate indicator of the jet flow condition. The interaction force increased almost linearly with increasing MPR. The amplification factor was inversely proportional to MPR. In general, the turbulence levels formed three distinct regions across the plume. Region 1 was defined as the upper region of the plume where the turbulence levels were moderate. Region 2 was the high turbulent level region located along the lower portion of the plume near the missile fuselage. Region 3 was the relatively low turbulence region along the plume core, where in the upper half, the turbulence levels were very low, and moving down towards the missile fuselage, the levels increased to those in region 2. The present data suggest a qualitative correlation between the shear strain rate field and the turbulence across the plume.

14. SUBJECT TERMS
Reaction Control Jet, Low Momentum Ratio Parameter, Hot Gas Effects, Mean Flow Measurements, Turbulence Measurements, Particle Image Velocimetry, Pressure Sensitive Paint

15. NUMBER OF PAGES
165

16. PRICE CODE

17. SECURITY CLASSIFICATION OR REPORT	18. SECURITY CLASSIFICATION ON THIS PAGE	19. SECURITY CLASSIFICATION OF ABSTRACT	20. LIMITATION OF ABSTRACT
UNCLASSIFIED	**UNCLASSIFIED**	**UNCLASSIFIED**	**UL**

NSN 7540-01-280-5500

Standard Form 298 (Rev.2-89)
Prescribed by ANSI Std. 239-18
298-102

CLAIMS NOT INCLUDED

PAGES iii + iv

FORWARD – EXECUTIVE SUMMARY

Development of rapid maneuvering control algorithms for Army supersonic missiles at low altitudes using low blowing ratio reaction jets is complicated by nonlinear, counterintuitive surface interactions, hot gas effects and poor predictability using modern computation fluid dynamic codes, where turbulence modeling is a key factor limiting the accuracy. The objectives of this research, which were directly tied to the Army low blowing ratio reaction control jet requirements, were documentation and improved understanding of (1) the surface flow interactions with hot gas effects and (2) the turbulent flow structure in the plume. An experimental analysis of the mean and turbulent flow properties for sonic and Mach 3 injection into a Mach 3 freestream was accomplished. The range of conditions included: MPR = 0.005-0.09, p_j / p_∞ = 0.6-19.0, T_j / T_∞ = 1.0-13.6 (helium was used to simulate the highest temperature), γ = 1.4 and 1.67, and p_{eb} / p_∞ = 0.19-6.15 (overexpanded, perfectly expanded and underexpanded jets were tested). Numerical simulations were not accomplished in the present effort. However, a full characterization of the high-speed jet interaction flowfield over a blended body missile fuselage (sharp-coned cylinder) was experimentally achieved, where specific pragmatic and scientific flowfield conclusions were drawn. For example, injection temperature, for a given overexpanded MPR, had a small but discernible effect on the boundary layer separation distance. The influence of the jet plume on the surface pressure distribution in the wake region of the flow was found to depend on MPR, where the wake region developed further downstream in terms of distance nondimensionalized by the jet exit port diameter. The effective backpressure concept was an accurate indicator of the jet flow condition (overexpanded, underexpanded or perfectly expanded). The upstream peak pressures associated with lambda shock and the horseshoe vortex increased with increasing MPR. The wake pressures decreased with increasing MPR. The interaction force increased almost linearly with increasing MPR. The amplification factor was inversely proportional to MPR. In general, progressing downstream, the turbulence levels formed three distinct regions across the plume. Region 1 was defined as the upper region of the plume, where the turbulence levels were moderate. Region 2 was defined as the high turbulent level region located along the lower portion of the plume near the missile fuselage. Region 3 was define as the relatively low turbulence region along the plume core, where in the upper half, the turbulence levels were very low, and moving down towards the missile fuselage, the levels increased to those in region 2. The present data suggest a strong qualitative correlation between the measured shear strain rate field and the turbulence across the plume, which supports the usage of the Boussinesq turbulence model approximation.

TABLE OF CONTENTS

COVER PAGE i
STANDARD FORM 298 ii
FORWARD – EXECUTIVE SUMMARY v
TABLE OF CONTENTS vi
NOMENCLATURE viii
LIST OF TABLES ix
LIST OF FIGURES x
1. PROBLEM STATEMENT AND SCIENTIFIC PERSONNEL 1
1.1 Problem Statement 1
1.1.1 Army Motivation 1
1.1.2 Army Research Challenges 3
1.1.3 Research Objectives 4
1.1.4 Research Approach 4
1.2 Scientific Personnel 5
2. BACKGROUND REVIEW 6
2.1 Continuous Injection into a Low-Speed Crossflow 6
2.2 Continuous Injection into a High-Speed Crossflow 7
2.2.1 Jets Issuing from a flat Surface into a Supersonic Stream 7
2.2.2 Jets Issuing from a Body of Revolution into a Supersonic Stream 11
3. FACILITIES AND INSTRUMENTATION 13
3.1 Wind Tunnel 13
3.1.1 High-Pressure Air Supply and Compressors 13
3.1.2 Stagnation Chamber 14
3.1.3 Mach 3 Nozzle & Operating Conditions 14
3.1.4 Test Section 14
3.1.5 Diffuser and Muffler 15
3.2 Missile Injector Models 15
3.2.1 Missile Fuselage and Injectors 15
3.2.2 Pebble Bed Heater 16
3.3 Measurement Apparatus 17
3.3.1 Surface Oil Flow Visualization (SOFV) 17
3.3.2 Five-hole Pitot /Cone-Static Pressure Probe 17
3.3.3 Two-Color Digital Particle Image Velocimetry (PIV) 18
3.3.4 Lavision Flowmaster3 PIV System for 2-D Turbulence Measurement 19
3.3.5 Pressure Sensitive Paint (PSP) 20
3.3.6 Schlieren/ Shadowgraph Optics 20
3.3.7 Pressure Transducers 21
3.3.8 Traverse System 21
3.3.9 High Temperature Thermocouple 22
3.3.10 Data Acquisition System 22
4. EXPERIMENTAL METHODOLOGIES 23
4.1 Five-Hole Probe 23
4.2 Pressure Sensitive Paint (PSP) 24
4.3 LaVision PIV 25

5. FLOWFIELD RESULTS 28
5.1 Flow Visualization 28
5.1.1 Surface Oil Flow Visualization (SOFV) 28
5.1.2 Mie-Scattering Visualization 32
5.1.3 Schlieren/ Shadowgraph Images 33
5.2 Mean Flow Measurements 34
5.2.1 Five-hole Probe 34
5.2.2 Pressure Sensitive Paint (PSP) 36
5.2.3 Particle Image Velocimetry (PIV) 39
5.3 Turbulent Flow Measurements (PIV) 42
5.3.1 Turbulence intensities 42
5.3.2 Turbulent Stresses 44
5.3.3 Turbulent Kinetic Energy 45
6. CONCLUSIONS AND PUBLICATIONS 46
6.1 Flow Visualization 47
6.2 Mean Flow 49
6.3 Turbulent Flow 50
6.4 Publications 52
REFERENCES 53
APPENDIX A FREESTREAM UNIFORMITY 59
APPENDIX B UNCERTAINTY ANALYSIS 60
B.1 Five-Hole Probe 60
B.2 LaVision PIV 62
B.3 Pressure Sensitive Paint 62
B.4 Separation Distance 62
TABLES 63
FIGURES 80

NOMENCLATURE

A_b	Missile Base Diameter
A_j	Jet Exit Area
C_F	Total Force Coefficient $[2F/(\rho_\infty u_\infty^2 A_b)]$
D	Missile Base Diamter (= 1.78 cm)
D_e	Jet Exit Diameter
D_j	Jet Throat Diameter
F	Total Reaction Force (= F_j + Interaction Force)
F_j	Jet Delivered (Momentum) Force
K_F	Force Amplification Factor (= F/F_j)
M	Mach Number
$\dot{m}$	Mass Flow Rate
MPR	Momentum Ratio Parameter (= $\gamma_j M^2_j P_j A_j / \gamma_\infty M^2_\infty P_\infty A_b$)
P	Pressure
T	Temperature
TKE	Turbulent Kinetic Energy
u	Axial Velocity
v	Transverse Velocity
x,y,z	Cartesian Coordinates
Δ	Separation Distance
γ	Ratio of Specific Heats
ρ	Density

Subscripts

c	Cone
eb	Effective Back
j	Jet
t	Stagnation
∞	Freestream
1	Local Property
2	Property Downstream of a Normal Shock

Superscripts

$( )'$	Fluctuating Quantity
$\overline{( )}$	Time Averaged Quantity

LIST OF TABLES

Table 1 Range of Jet Parameters 63
Table 2 Freestream Conditions 64
Table 3 Tunnel Operating Conditions 65
Table 4 Diffuser Dimensions 66
Table 5 Injector Dimensions 67
Table 6 Injector Operating Conditions 68
Table 7 Range of Temperature Ratios 69
Table 8 Flowmaster3 Camera Specs 70
Table 9 LaVision PIV Laser Specs 71
Table 10 Transducer Specifications 72
Table 11 Five-Hole Probe Calibration 73
Table 12 Five-Hole Probe Calibration Data 74
Table 13 Parameters used to process PIV images and vectors 75
Table 14 Boundary Layer Separation Distance 76
Table 15 Pressure Transducers and Uncertainties 77
Table 16 High Temperature Thermocouple and Uncertainty 78
Table 17 Measurement Uncertainty Summary 79

LIST OF FIGURES

Figure 1 Low-Speed Jet Interaction Flowfield 80
Figure 2 Supersonic Jet Interaction Flowfield (Flat Plate & Blended Missile Body) 81
Figure 3 Mach 3.0 Wind Tunnel (schematic and photograph) 82
Figure 4 Flow Straightener (schematic) 83
Figure 5 Sketch of the Mach 3 Nozzle 84
Figure 6 Test section with a model (schematic and photograph) 85
Figure 7 Diffuser 86
Figure 8 Missile Model Schematic 87
Figure 9 Model Photographs 88
Figure 10 Pebble bed heater (schematic) 89
Figure 11 Pebble Bed Heater 90
Figure 12 Photograph of 5-hole Pitot Probe 91
Figure 13 LaVision PIV Apparatus 92
Figure 14 Five-Hole Probe Calibration 93
Figure 15 General Flow Features 94
Figure 16 Surface Oil Flow Visualizations for Model M1A 95
Figure 17 Surface Oil Flow Visualizations for Model M3A-LP 96
Figure 18 Surface Oil Flow Visualizations for Model M3A-HP 97
Figure 19 Surface Oil Flow Visualizations for Model M3H 98
Figure 20 Boundary layer separation distance vs. MPR 99
Figure 21 Boundary layer separation distance versus jet Pressure (Model M3A) 100
Figure 22 Change in Boundary layer separation distance vs. Change in Temperature 101
Figure 23 Mie-scattering image, Model M1A, MPR 0.006 102
Figure 24 Instantaneous Mie-scattering images (Model M1A, MPR 0.006) 103
Figure 25 Average Mie-scattering images (Model M1A, MPR 0.006) 104
Figure 26 Instantaneous Mie-scattering images (Model M3A-LP, MPR 0.06) 105
Figure 27 Average Mie-scattering images (Model M3A-LP, MPR 0.06) 106
Figure 28 Instantaneous Mie-scattering images (Model M3A-LP, MPR 0.03) 107
Figure 29 Average Mie-scattering images (Model M3A-LP, MPR 0.03) 108
Figure 30 Shadowgraph images 110
Figure 31 Color Schlieren Images 111
Figure 32 Mach Number Contours 114
Figure 33 Contours of the total pressure ratio (P_{t2}/P_{t1}) across the Pitot probe shock 117
Figure 34 Total Pressure ($P_{t1}/P_{t\infty}$) Contours 120
Figure 35 Pitot Pressure ($P_{t2}/P_{t\infty}$) Contours 123
Figure 36 Cone-Static Pressure ($P_c/P_{t\infty}$) Contours 126
Figure 37 Surface pressure contour (Model M1A) 127
Figure 38 Surface pressure contour (Model M3A-LP) 128
Figure 39 Surface pressure contour (Model M3A-HP) 129
Figure 40 Surface pressure contour (Model M3H) 130
Figure 41 Effect of jet MPR on the centerline surface pressure 131
Figure 42 Effect of jet pressure ratio on the centerline surface pressure 132
Figure 43 Total Force Coefficient vs. MPR 133
Figure 44 Amplification Factor vs. MPR 134

Figure 45 Mean axial velocity contours, $\overline{u}/u_\infty$ (Model M1A, MPR = 0.006) 135
Figure 46 Mean transverse velocity contours, $\overline{v}/u_\infty$ (Model M1A, MPR = 0.006) 136
Figure 47 Mean axial contours, $\overline{u}/u_\infty$ (Model M3A-LP, MPR = 0.06) 137
Figure 48 Mean transverse velocity contours, $\overline{v}/u_\infty$ (Model M3A-LP, MPR = 0.06) 138
Figure 49 Axial Velocity Contours, $\overline{u}/u_\infty$ (Model M3A-LP, MPR = 0.03) 139
Figure 50 Mean Transverse Velocity, $\overline{v}/u_\infty$ (Model M3A-LP, MPR = 0.03) 140
Figure 51 Vorticity, $(\partial\overline{u}/\partial y - \partial\overline{v}/\partial x)\cdot D/u_\infty$ (Model M1A, MPR = 0.006) 141
Figure 52 Vorticity, $(\partial\overline{u}/\partial y - \partial\overline{v}/\partial x)\cdot D/u_\infty$ (Model M3A-LP, MPR = 0.06) 142
Figure 53 Vorticity, $(\partial\overline{u}/\partial y - \partial\overline{v}/\partial x)\cdot D/u_\infty$ (Model M3A-LP, MPR = 0.03) 143
Figure 54 Shear Strain, $(\partial\overline{u}/\partial y + \partial\overline{v}/\partial x)\cdot D/u_\infty$ (Model M1A, MPR = 0.006) 144
Figure 55 Shear Strain, $(\partial\overline{u}/\partial y + \partial\overline{v}/\partial x)\cdot D/u_\infty$ (Model M3A-LP, MPR = 0.06) 145
Figure 56 Shear Strain, $(\partial\overline{u}/\partial y + \partial\overline{v}/\partial x)\cdot D/u_\infty$ (Model M3A-LP, MPR = 0.03) 146
Figure 57 Axial Turbulence Intensity, $\sqrt{\overline{u'^2}}/u_\infty$ (Model M1A, MPR = 0.006) 147
Figure 58 Transverse Turbulence Intensity, $\sqrt{\overline{v'^2}}/u_\infty$ (Model M1A, MPR = 0.006) 148
Figure 59 Axial Turbulence Intensity, $\sqrt{\overline{u'^2}}/u_\infty$ (Model M3A-LP, MPR 0.06) 149
Figure 60 Transverse Turbulence Intensity, $\sqrt{\overline{v'^2}}/u_\infty$ (Model M3A-LP, MPR 0.06) 150
Figure 61 Axial Turbulence Intensity, $\sqrt{\overline{u'^2}}/u_\infty$ (Model M3A-LP, MPR 0.03) 151
Figure 62 Transverse Turbulence Intensity, $\sqrt{\overline{v'^2}}/u_\infty$ (Model M3A-LP, MPR 0.03) 152
Figure 63 Reynolds Stress, $\overline{u'v'}/u_\infty^2$ (Model M1A, MPR 0.006) 153
Figure 64 Axial Stress, $\overline{u'u'}/u_\infty^2$ (Model M1A, MPR 0.006) 154
Figure 65 Transverse Stress, $\overline{v'v'}/u_\infty^2$ (Model M1A, MPR 0.006) 155
Figure 66 Reynolds Stress, $\overline{u'v'}/u_\infty^2$ (Model M3A-LP, MPR 0.06) 156
Figure 67 Axial Stress, $\overline{u'u'}/u_\infty^2$ (Model M3A-LP, MPR 0.06) 157
Figure 68 Transverse Stress, $\overline{v'v'}/u_\infty^2$ (Model M3A-LP, MPR 0.06) 158
Figure 69 Reynolds Stress, $\overline{u'v'}/u_\infty^2$ (Model M3A-LP, MPR 0.03) 159
Figure 70 Axial Stress, $\overline{u'u'}/u_\infty^2$ (Model M3A-LP, MPR 0.03) 160
Figure 71 Transverse Stress, $\overline{v'v'}/u_\infty^2$ (Model M3A-LP, MPR 0.03) 161
Figure 72 TKE, $(\overline{u'^2}+\overline{v'^2})/2u_\infty^2$ (Model M1A, MPR 0.006) 162
Figure 73 TKE, $(\overline{u'^2}+\overline{v'^2})/2u_\infty^2$ (Model M3A-LP, MPR 0.06) 163
Figure 74 TKE, $(\overline{u'^2}+\overline{v'^2})/2u_\infty^2$ (Model M3A-LP, MPR 0.03) 164
Figure 75 Freestream Mach Number Contour 165

1. PROBLEM STATEMENT AND SCIENTIFIC PERSONNEL

1.1 Problem Statement

1.1.1 Army Motivation

Jets have the potential to be an effective means of controlling aerodynamic characteristics of high-speed vehicles and weapon systems. One Army application is the use of reaction control jets for rapid maneuvering of high-speed intercept missiles. Hypersonic interceptor designs typically include several lateral jets used for divert and/or altitude control. Air-to-air interceptors usually require a continuous and long duration reaction control jet for accuracy and rapid maneuverability. In addition, confined space firing (e.g., anti-tank or Guerilla warfare) missile control systems are required to be effective at low-speed with good maneuverability and very short response time [Champigny and Lacau (1994)].

Accurate aerodynamic characterization of the jet interaction with the missile body is essential for the design of an autopilot. One important parameter of jet interaction is the amplification factor, which is defined as the ratio of the effective force to the vacuum thrust. Vacuum thrust is the net reaction force created when a jet is fired in a vacuum; this force is equivalent to the thrust of a rocket engine. However, in a sensible atmosphere, the net force produced between the jet and free stream can be higher or lower than the vacuum thrust of the rocket engine. In the extreme case, the net force on an axisymmetric body can be the opposite of what is expected, a situation known as control reversal [Chamberlain et al (2000)]. When a jet is first fired into a supersonic crossflow, a shock wave upstream of the jet is created. The high pressures associated with the shock causes a positive amplification. A portion of the shock that wraps around the missile fuselage

creates a high-pressure region under the axisymmetric body causing a de-amplification on the net force. Also, the low-pressure wake region downstream of the jet causes de-amplification factor is further decreased. If the total de-amplification is higher than the total amplification, the net force will be opposite than what is anticipated. The most severe de-amplification happens at low altitudes, low Mach numbers, and low angle of attack.

At high altitude, typical reaction control jets produce several thousand pounds of thrust in less than 10 ms [Roger (1999)]. The forces involved at high altitude are fundamentally of action-reaction type in the usual Newtonian sense. However, at lower altitudes, jet interaction is confined to be near the surface, and hence produces very complicated nonlinear surface interactions, which can adversely affect the vehicle control. These nonlinear, and often unsteady, interactions must be understood in order to develop effective and accurate vehicle control schemes.

A number of parameters have been listed that can affect thruster control effectiveness. A subset of salient parameters are [Roger (1999)]: the freestream Mach number (M_∞), the jet Mach number (M_j), the jet Momentum-Parameter-Ratio (MPR), the jet pressure ratio (P_j/P_∞), the jet temperature ratio (T_j/T_∞), the Reynolds number (Re), and the jet gas ratio of specific heats (γ_j). In addition to these parameters, jet geometry, and chemical reactions within the plume were also identified as important, especially for flow separation.

1.1.2 Army Research Challenges

Flight control of supersonic Army missiles at low altitudes using low blowing ratio reaction jets is complicated due to (1) nonlinear, counterintuitive surface interactions, (2) hot gas effects and (2) poor predictability using modern computation fluid dynamic codes, where turbulence modeling is a key factor limiting the accuracy [Doligalski (1997)]. Furthermore, it has been documented [Champigny and Lacau (1994), Chamberlain et al (1999), Dash et al (1999), Graham et al (1999), Hsieh (1999), Thoenes (1999), and Roger (1999)] that jet interaction experimental data is lacking, and high quality systematic experimental studies to build a database are needed. Numerous three-dimensional vortex features, unsteadiness, turbulence, large thermal gradients, and real gas effects characterize the flowfield associated with a jet into a high-speed crossflow. These features make the flowfield very complicated. A detailed description of the up-to-date research contributions on the flowfield is provided in Chapter 2. The poor flowfield understanding and predictability are underscored by reported computational fluid dynamic calculations that predicted the normal force in the wrong direction [Doligalski (1997)]. Appropriate turbulence modeling is the key factor that limits numerical accuracy.

Currently, engineers and scientists rely on an approximate form of the governing equations of motion to predict the overall meanflow character of these flows. The Reynolds and Favre averaged forms of the Navier-Stokes equations are universally used to compute low-speed and high-speed flows, respectively. Some recent studies [Graham and Weinacht (1999), Hsieh (1999), Kikumoto and Sentoh (2001), Graham and Weinacht

(2000)] (using Reynolds averaged N-S technique, Baldwin-Lomax, k-ε, GASP, PARCH, etc) showed that existing turbulence models fail near the recirculation region in front of the jet and near the recompression shock. To correct these shortcomings, there is a need for high quality, high fidelity experimental data that will allow for verification of current and future computational fluid dynamic results [Margason (1993)].

1.1.3 Research Objectives

The overarching objective of the present research is to improve the understanding and predictability of high-speed high-temperature jet interaction flowfields. Specific Army requirements are low Mach, low altitude, and low blowing ratio operating conditions missile flight control. Therefore, the following objectives were established for this research.

1. Documentation and improved understanding of the missile surface interactions for low MPR jets, with elevated injection temperature.
2. Documentation and improved understanding of turbulent flow structure of the jet plume for the low MPR jet interaction flows.

1.1.4 Research Approach

A three-year research program was fully dedicated to experimental characterization of the jet interaction flowfield over a 3-D blended missile fuselage model. A full gamut of experimental techniques was used to characterize the mean and turbulent flow properties. The tunnel was operated to simulate Mach 3.0 flight at an

altitude of 17-km. The range of jet parameters studied here is listed in Tables 1, and the freestream flow conditions are given in Table 2.

In summary, surface oil flow visualization and pressure sensitive paint experiments were performed to provide a global picture of the flow/surface interaction and aerodynamic loading. Schlieren/shadowgraph techniques were used to quantify the shock structure. Instantaneous and time averaged Mie-scattering imaging was used characterize the jet plume trajectories. Mean flow mapping was accomplished using a 5-hole pressure probe and particle image velocimetry. Particle image velocimetry also provided documentation of the turbulent flow structure in the plume.

1.2 Scientific Personnel

The PI for this project was Dr. Rodney D. W. Bowersox, Associate Professor of Aerospace Engineering. This project supported the PhD dissertation research of Mr. Zakaria Mahmud, who successfully defended his dissertation, in the Department of Aerospace Engineering and Mechanics at the University of Alabama, on November 8, 2002.

2. BACKGROUND REVIEW

2.1 Continuous Injection into a Low-Speed Crossflow

The flowfield for injection in a cross flow research has received considerable attention because of the many important practical applications in both military and civil disciplines. Margason (1993) summarized the evolution of jet into a cross flow research for the time span between 1932 and 1993. Over 300 articles were included in this review. A brief synopsis of the salient features is presented here with the inclusion of results from recent work.

The numerous studies on transverse jets into low-speed crossflows [Keffer et al (1963), Kamotani (1972), Moussa (1977), Perry (1993), Fric and Roshko (1994), Findlay (1999)] provide detailed documentation of the mean flowfield structure and qualitative insight into the vortical flow features. The flowfield structure for injection into a low-speed crossflow is shown schematically in Fig. 1. There appears to be at least four vortical flow motions created by the transverse jet in a crossflow [Fric and Roshko (1994)]. As the jet emerges into the crossflow, it is curved downstream by the crossflow. The jet plume acts as a cylindrical obstacle to the crossflow and creates an adverse pressure gradient, which eventually generates a wraparound horseshoe vortex on the surface. Then, the jet plume evolves into a "kidney-bean" shape, which is due to the counter rotating vortex pair. This counter rotating vortex pair dominates the downstream flow [Kamotani (1972)]. The origin of this vortex pair is believed to be near the jet exit and caused by the lateral shearing along the plume edges and the pressure gradient due to turning the flow into the freestream direction. Another ring-like vortex structure appears

in the wake region. These alternating vertical vortices, in many papers named as the wake vortices, give the appearance of a "Karman-vortex-street"[Perry et al (1993)].

Yasuhiro and Isaac [Kamotani et al (1972)] used hot-wire anemometry to map the velocity, temperature, and turbulence intensities for a low-speed JI flow. They discerned that the momentum ratio significantly affects the jet velocity, and turbulence intensity; while the entrainment process is independently controlled by the normal and parallel components of the velocity. Perry et al [Perry et al (1993)] studied the entrainment and mixing processes of a low-speed jet in a cross flow. The results from the flying hot-wire and flow visualization revealed that there exists many vortex systems and they are inter-connected; the karman vortex street like structure come from the vorticity generated at the wall. Findlay et al [Findlay et al (1999)] employed three-component LDV to study the flowfield characteristics. The paper further proved the accepted flowfield characteristics.

2.2 Continuous Injection into a High-Speed Crossflow

The compressibility effects associated with injection into a high-speed crossflow create additional flowfield complications. An extensive literature review for high-speed jet interaction flow was performed as part of this study. Over 100 articles were examined. A synopsis of the flowfield, built from this review for flat and axisymmetric surfaces, is described below.

2.2.1 Jets Issuing from a flat Surface into a Supersonic Stream

Many of the mean flow features of injection into supersonic crossflows are similar to those described above for a low-speed crossflow. However, compressibility creates additional features that do not have incompressible counterparts [Schetz and Billig

(1966), Schetz et al (1967), Billig et al (1971), Heister and Karagozian (1989), Grasso and Magi (1995), Santiago et al (1995) and Chenault et al (1998)]. Figure 2(a) presents the accepted 3-D structure of a highly under expanded jet into a supersonic cross flow on a flat surface. The transverse jet causes an obstruction to the freestream flow and a bow shock is created upstream of the jet; typically termed as the interaction shock. For injector configurations where the injector diameter is greater than the boundary layer thickness, a separation bubble and a lambda shock form upstream of the injector port [Schetz and Billig (1966)]. For most applications, the jet is operated in an underexpanded condition. Hence, the jet fluid undergoes a Prandlt-Meyer expansion, recompresses through a barrel shock, and then terminates into a normal shock, which is called the Mach disk. As the jet plume curves downstream due to the crossflow, the shape of the plume is transformed into the kidney bean shape, which is attributed to the counter rotating vortex pair. As the freestream flow wraps around the jet, a recompression shock is created. Chenault et al (1999) suggested that the recompression shock was a new mechanism adding to the strength of the vortex pair.

The effective backpressure plays an important role on the structure of the jets in a supersonic crossflow [Schetz et al (1967)]. In addition to underexpanded jets, the present research also examined overexpanded and perfectly expanded cases. For the overexpanded case, the flowfield structure is slightly different. Here, the jet plume terminates through an oblique shock cone. The angles of the conical shock system depend on the blowing ratios. Heister and Karagozian (1989) studied the perfectly expanded transverse jets into the supersonic crossflow, where terminating shocks were absent.

In 1960s, the flowfield structure was documented using schlieren photographs, mean flow measurements, concentration measurements, and mass flow rates. Schetz et al [Schetz et al (1967), Schetz et al (1968)] investigated the relationship between the highly under expanded jet into a supersonic (Mach 2.1) freestream, as well as for the jet issuing into a quiescent medium to determine the penetration height and the horizontal displacement of the mach disk. The papers concluded that for a fixed M_j and fixed jet geometry, the displacement of the Mach disk varies as $P_j^{1/2}$; and the penetration height is proportional to the half power of the mass flow rate at each Mach number. The penetration height increased with increasing jet Mach number, however the effect is not very significant beyond Mach 2.0. Billig et al (1971, 1994) later developed a model to account for different jet injection angles and the turbulent mixing after the Mach disk using a modified effective backpressure concept.

The effects of compressibility on free shear layers are also important area of research [Samimy et al (1990), Samimy et al (1992), Papamoschou and Roshko (1988), Bradshaw (1966), Papamoschou and Roshko (1986), Samimy et al (1989)]. The concept of the convective Mach number is well agreed upon to be the most effective compressibility factor. In summary, these papers documented the non-dimensionalized shear layer, vorticity and momentum growth rates as a function of convective Mach number, ranging from subsonic to supersonic.

McCann and Bowersox (1996) investigated air injection (Mach 1.8) at an angle of 25 degree into a freestream of Mach 2.9. Using cross film anemometry and conventional mean flow probes, the paper provided detailed compressible turbulence and mean flow measurements. The turbulent kinetic energy had two peaks, which were nearly co-located

with the counter rotating vortex pair. The compressibility terms ($\overline{u\rho'v'}/\overline{\rho u'v'}$ and $\overline{u\rho'w'}/\overline{\rho u'w'}$) were also found to be significant, and were estimated as 67.0 – 75.0% of the total Reynolds shear stress. Bowersox (1996) further investigated the anisotropy coefficients (e.g.; $A_{xy} = \sqrt{\overline{(\rho v)'^2}}/\sqrt{\overline{(\rho u)'^2}}$, A_{xz} and A_{zy}) across plume for the same parametric conditions. The distribution of A_{zy} was asymmetric, with the maximum in one vortex and the minimum in the other. The results of the experiment were later simulated with the second order Reynolds stress turbulence modeling [Chenault et al (1999)]. The analysis was physically consistent, where accurate prediction for both the mean and turbulent flow quantities was achieved.

Santiago et al (1995) mapped the instantaneous velocity distribution of sonic transverse jet into a Mach 1.6 free stream. A two-component frequency pre-shifted LDV system was used to provide over 2200 measurement locations in the transverse midline plane. A potentially important suggestion from that study was that for underexpanded jets, counter sinking the jet exit holes to let it fully expand before it encounters the cross flow might increase the penetration height and mixing.

Gruber et al (1997) in 1997 used pressure sensitive paints to measure surface pressure in a supersonic transverse injection flowfields. Both circular and elliptical nozzles were investigated at different momentum flux ratios (0.99 to 3.95), and it was found that momentum flux ratios as well as injector geometries have significant effects on the surface pressure distribution. The research was conducted with two different pressure sensitive paints, where the PtOEP based paint was found to be more temperature sensitive than the pyrene based paint.

2.2.2 Jets Issuing from a Body of Revolution into a Supersonic Stream

The flowfield structure of a jet issuing from a curved body of revolution is qualitatively similar to that over a flat surface. The quantitative information varies due to the three-dimensional effect of the curved surface. Figure 2(b) presents the 3-D structure of a jet emerging from an axisymmetric body (this sketch was based on the present study).

A number of studies [Champigny and Lacau (1994), Chamberlain et al (1999), Dash et al (1999), Graham and Weinacht (1999), Hsieh (1999), Thoenes (1999), Roger (1999), Naumann et al (1993), Kikumoto et al (2001), Graham and Weinacht (2000), Brandeis and Gill (1998), Srivastava (1997), Srivastava (1998) and Srivastava (1999)] investigated the influence of jets issuing from a curved surface into a supersonic cross flow. Champigny and Lacau [(1994)] reported on the importance of lateral jet control for tactical missiles and the associated difficulties with the wind tunnel testing. The hot gas effects were of fundamental concern for a wind tunnel test in comparison to the reactant jet fluids at flight conditions. It was stated that low molecular weight gas (e.g.; helium) could improve the simulation, where for the same jet momentum parameter ratio (MPR), the jet velocity is much higher than the cold air jet. As a result, helium at ambient temperatures can be used to simulate air at approximately 2000K.

Graham and Weinacht (1999) numerically simulated lateral control jets in supersonic flow for an axisymmetric body. Surface pressure measurements downstream of the jet were found to be in good agreement with the experimental results. Using the existing Reynolds averaged Navier-Stokes computational technique, the paper also concluded that the flight velocity and jet mass flow appeared to be the most significant on

the force and moments control, while nose shapes and angle of attack produced relatively small effects. In a second numerical study, Hsieh (1999) found that the thrust coefficient and jet Mach number should be identical in order to have the satisfactory numerical simulation of missile control jets.

Roger (1999) summarized nearly fifty years of research on flight and wind tunnel tests of thruster control for supersonic and hypersonic interceptors. Some of the salient findings were: (1) for 90^0 jets, there is essentially no change in amplification factor with jet Mach number; (2) attitude moment amplifications factors are always positive and can be larger than three, while lateral amplification factors can be negative; (3) force and moment measurements can be affected if the jet plume interacts with the wind tunnel wall boundary layer, and (4) a methodology to determine jet interaction performance for modern hit-to-kill designs is lacking.

Recently, it was reported that Reynolds averaged CFD surface pressure distribution predictions were within the experimental accuracy [Graham and Weinacht (2000) and Kikumoto and Sentoh (2001)]. However, both of these studies showed discrepancies in the recirculation region in front of the jet and at the end of the body near the recompression shock.

3. FACILITIES AND INSTRUMENTATION

3.1 Wind Tunnel

This research project started at a very preliminary stage, where as a first step the wind tunnel was designed and constructed in-house. A schematic drawing of the wind tunnel is shown in Fig. 3(a). Figure 3(b) shows a photograph of the wind tunnel. The free stream flow conditions are listed in Table 2. A detailed specification of the compressors, storage tank, nozzle block, models, test section, and diffusers are provided in the following sub sections.

3.1.1 High-Pressure Air Supply and Compressors

The storage tank volume was 28-m^3 with a maximum allowable design pressure of 1.38 MPa. The Century Electric Co. compressors simultaneously filled up the storage tank to 1.25 MPa. The compressors were run by two 20 hp squirrel-case induction poly-phase motor (model number: SC-286U-FC3-3). Both compressors at full running condition usually took about 90 minutes to fill up the tank. An Aerolab heater was used to dry the compressed air to a dew point of –70 ^{0}C. The heater had two tanks filled with silica-gel desiccants. The compressed air passed through one tank while the desiccant in the other tank was heated. After a six-hour cycle, the dryer tanks were manually switched. About midway through the project, two new compressors (Ingersoll-Rand model SSR-HXP50SE) were purchased at no additional cost to the ARO. The compressors rated operating pressure was 1.38 MPa. The motor used for each of the compressors was 50 hp (3 phase/ 60 Hz). An automatic air-cooled Ingersoll-Rand dryer,

model TZ300HP-EMS-3V-LDP (Desiccant- activated alumina, dew point of –73 ^{0}C, was also installed. The pump-up time with the new compressors was about 30 minutes.

3.1.2 Stagnation Chamber

The stagnation chamber consisted of flow straightening tubes, a damping screen and a Pitot probe. The flow straightening tubes were 10.16 cm long and 1.27 cm in diameter. The steel tubes were metal-jacketed with an upstream-perforated cone and a downstream damping screen. A schematic drawing of the flow straightener is shown in Fig. 4.

3.1.3 Mach 3 Nozzle & Operating Conditions

The Mach 3 nozzle was made of aluminium. The measured Mach number was 2.97±0.04 (see Appendix A). The nozzle block was 25.4 cm long, with a 1.65 × 7.62 cm^2 throat area. A schematic drawing is given in Fig. 5. A Pitot tube was inserted through the nozzle block to measure the upstream total pressure. The upstream total temperature was monitored with an Omega brand type K thermocouple (the uncertainty was ± 2K). The tunnel operating pressure was regulated by the compressed air (from a different source) that was coupled with a 7.62 cm (3 inch) LESLIE control valve. The nominal operating pressure of the tunnel was 0.64 ± 0.005 MPa for the mean flow measurements using five-hole probe. For the PIV, and shadowgraph/schlieren measurements the nominal pressure was 0.61 ± 0.021 MPa. The tunnel operating conditions are summarized in Table 3.

3.1.4 Test Section

The dimensions of the test section were 7.62 × 7.62 × 30.5 –cm^3 [Fig. 6(a)]. The wind tunnel models were bolted to the floor of the test section, as shown in Fig. 6(b). The

sidewalls contained optical glass windows. A test section ceiling made of solid optical grade Plexiglas was used for the PIV, PSP and surface oil flow visualization. A slotted solid aluminium ceiling was used for the mean flow measurement using the five-hole Pitot/cone-static probe. The ceiling was slotted in two different longitudinal locations such that the probe tip could be traversed at 0.86 cm and at 6.35 cm downstream of the injector port. The five-hole probe was attached to the stepper motor slide for the vertical traverse and the motor was mounted on a rail for horizontal traverse. The axial position uncertainty was ±0.8 mm, and the spanwise traverse location uncertainty was ±0.4 mm.

3.1.5 Diffuser and Muffler

The variable area supersonic diffuser was designed to operate over a range of Mach numbers, 1.5 – 4.0. The diffuser design was a part of an undergrad student project, and later was used for this research work. The inlet and the exit area of the diffuser were fixed at 7.62 cm × 7.62 cm and 12.7 cm × 7.62 cm, respectively. The hinged plate was pinned to the walls and could be adjusted with variable Mach number supersonic wind tunnel test sections. Diffuser dimensions are listed and shown in the Table 4 and Fig. 7. A silencer was constructed and attached to the wall.

3.2 Missile Injector Models

3.2.1 Missile Fuselage and Injectors

The wind tunnel models were half-body 3-D blended-wall missile fuselages (Fig. 2b). A single port circular injector was machined into each model. The models were 19.05 cm long, 1.78 cm in diameter (D), and 13^0 half-cone angles. A schematic of the models can be seen in Fig. 8. Four models with different injectors were used for the

current research. The models were designated M3A-HP (Mach 3, air injectant, high injection pressure), M3A-LP (Mach 3, air injectant, low injection pressure), M3H (Mach 3, helium injectant), and M1A (Mach 1, air injectant). A fifth model (M1A-L, Mach 1, air injectant, and Larger injector diameter of 0.953 cm) was also examined in few preliminary experiments, but the disturbances were too large for the present experimental apparatus. Figure 9 shows a photograph of all the models. Model M3H was operated with compressed Helium gas and the rest were with compressed air. Detailed injector dimensions are listed in Table 5 and the injector operating conditions are summarized in Table 6. The injector operating conditions as well as the free stream conditions were set to achieve a range of low MPRs, 0.005 to 0.09.

3.2.2 Pebble Bed Heater

A pebble bed heater was designed and constructed for high temperature injection. The heater dimensions are shown in Fig. 10. The hot jet injection surface oil flow visualization was performed at 1190 ^{o}F (916 K). The pebble bed heater and the electric furnace (Fisher Scientific Model-14, Cat No. 10-750-14 & 14A) used for this experiment are shown in Fig. 11. The ceramic pebbles were first heated in the electric furnace to 2000 ^{o}F and then poured into the home-built heater. The heater was then placed under the tunnel test section [Fig. 11(d)]. Due to safety concerns, this hot jet interaction flowfield visualization was performed only for the sonic model. The temperature of the air passing through the hot pebble bed heater was recorded with two thermocouples. One of the thermocouples measured the hearth temperature of the pebble bed heater and the other measured the exit air temperature (i.e.; the jet total temperature). As suggested in Chapter

2, helium was used to simulate higher temperatures than were available with the pebble bed. The available temperature operating conditions are listed in Table 7.

3.3 Measurement Apparatus

3.3.1 Surface Oil Flow Visualization (SOFV)

Dow Corning 200 fluid (1000CST) was used for surface oil flow visualization. The oil, mixed with orange fluorescent dye (Day-Glo color corporation, pigment sample T-15 blaze orange), was smeared onto the test surface and illuminated by an ultraviolet lamp. A CCD camera (Kodak Professional DCS 460c, resolution 3060×2036 with a Nikon N90- 50mm lens) mounted on top of the test section was used to collect the images of the flow structure during the tunnel run condition. The camera was attached on to the tri-pod and images were taken through the transparent test-section ceiling made of optical grade solid Plexiglas. The camera was connected (by a SCSI port and a cable) to an NEC Intel Pentium II PC running Microsoft Windows 98. An Adaptec AVA-1502 SCSI Host Adapter with a SCSI2 port transferred the digital image recorded by the CCD imager to the computer. The image was then acquired and displayed through the Kodak TWAIN driver into the Adobe Photoshop 4.0 application software for Windows.

3.3.2 Five-hole Pitot /Cone-Static Pressure Probe

An Aeroprobe Inc. Brand L-shaped five-hole Pitot/cone-static pressure probe with half cone angle of 19° was used to measure the mean Mach number. Figure 12 shows the 5-hole probe. A stepper motor with velmex bi-slide rail was used to traverse the probe in the vertical y-direction. The traverse distance was about 5.0 cm from the test-section

floor. A Linear Voltage Displacement Transducer (LVDT), Omega model LD100 with a SP200A controller was used to record the probe height. The analog output of the LVDT transducer was set to 0.0 – 5.0 volts for a range of movement of 0.0 – 5.0 cm. The x and z locations were manually set.

3.3.3 Two-Color Digital Particle Image Velocimetry (PIV)

The digital two-color PIV system consisted of two Continuum brand Surelite Nd:YAG lasers that were powered by two Continuum Model SLI-10 lasers. The surelite lasers each produce coherent green (532 nm, 225 mJ) laser beams. One of the green laser beams was routed through a red dye laser (607 nm). A 12-volt DC motor driven gear pump was used to circulate the dye (sulfarhodamin 640 dissolved in methanol). The dye laser was about 20-30% efficient. The red and green beams were then co-located in space and converted into a single sheet by a series of optical components. The time delay between the red and green beams was controlled with an ISSI, Inc. custom control circuit. Model DG535 four-channel digital delay/pulse generator (included with the complete PIV system) was used to set a time delay of 400 ns. The optics that directed the beams into the test section were mounted on to the nearby wall to avoid vibration during tunnel runs. A Kodak model 460c CCD camera with a Nikon N90 (150 mm) lens was placed apart from the wind tunnel table (base) to prevent vibration. The CCD camera captured the image through optical grade glass windows in the test section sidewalls. Because of safety concerns with the high-pressure seeding; only the sonic missile models were used for the PIV measurement.

Atomized olive oil was used as the seed material. A TSI brand model 9306 six-jet atomizer was used. The atomizer was placed in a compressed air chamber [Fig. 13(a)] to

ensure proper seeding capability at higher than recommended pressures. The flow tracking capability, 3-dB point frequency response of 60-200 kHz is described in Bowersox (1996). In-house software (b-PIVbeta-1.08) was used to perform the post processing of the data and to calculate the instantaneous velocity distribution.

Due to camera framing rate limitations (1–2 images per tunnel run), this system was not suitable for turbulence measurements. Hence, PIV measurements were acquired with a newer alternate PIV system, as described in the next section.

3.3.4 Lavision Flowmaster3 PIV System for 2-D Turbulence Measurement

The LaVision PIV system uses a Flowmaster3 CCD camera with a New Wave Research Nd-Yag laser. The 1280 × 1024 pixel, 12-bit CCD camera provided a maximum of 8 single frame images per second. Detailed camera specifications are documented in Table 8. The 532 nm class IV laser (detailed specifications are listed in Table 9) and the camera interface were all linked together with an externally triggered Programmable Timing Unit (PTU) and a PC. Figure 13(b) shows the components of LaVision PIV system. The laser power was set at 60% with the time delay between the two exposures of 600ns. Double frame/ double exposure cross correlation mode was used to capture images. The focal point of the laser sheet was placed on top of the measurement plane surface that provided about a maximum of 1.0 mm sheet thickness throughout. The PIV optics and the camera were mounted onto the lab wall and floor, respectively, so that the minimal tunnel vibration would not affect the measurements. Olive oil was seeded with a TSI Model 9306 six-jet atomizer. The atomizer (seeder) was placed in a tank as described in Section 3.3.3. When the smoke-full tank reached the required pressure, the tank outlet valve was released, and thus allowed the smoke to pass

through the injector port. Davis6.04 software and the vector analysis 3.0 software were used to post process the images.

3.3.5 Pressure Sensitive Paint (PSP)

ISSI, Inc. brand Uni-FIB Pressure Sensitive Paint (PSP) was used. The paint contained two parts: an oxygen permeable flouroacrylic co-polymer (FIB) binder and a fluorinated Platinum porphyrin *meso*-Tetra-pentaflourophenyl porphrine [Pt(TfPP)] oxygen sensitive probe molecule. The PSP was applied using an airbrush sprayer. The temperature sensitivity was 0.6%/°C. The paint was illuminated with two blue (464 nm) LED light sources (0.25 W each). The luminescence output (650 nm) was acquired with a Pixelvision SpectraVideo 16-bit CCD camera (model SV512V1A/PFT-95). The paint calibration stemmed from the Stern-Volmer relationship, where the pressure was expressed as a function of I_{ref}/I. As suggested by the manufacturer, the calibration data were fit with a second order polynomial. The uncertainty for the PSP, as provided by the manufacturer was ±2.0% of the measured value. The overall uncertainty is described in Appendix B.

3.3.6 Schlieren/ Shadowgraph Optics

The schlieren/shadowgraph system consisted of two concave mirrors (20.32cm Dia, 99.06cm FL), one light source, a screen, a CCD camera, a color knife-edge, and a PC. Shadowgraph setup was relatively simple. A single concave collimating mirror was used to create a collimated light beam that passed through the test section sidewall windows and onto a screen. The Kodak 460dcs camera system (described above) was used to capture the image on the screen. For the schlieren images, the collimated beam that passes through the test section was projected onto a second mirror. The color knife-

edge was located at the focal point of the reflected beam. The diverging beam was viewed on the screen, and the CCD camera captured the color image.

3.3.7 Pressure Transducers

A number of pressure transducers were employed for the pressure measurements at different locations. For the upstream total pressure and the test-section static pressure measurements Omega brand model PX302 (range: 0-100 psi) and PX 202 (range: 0-15 psi) were used. DP25 signal conditioners were used for both of these transducers. For the mean flow measurement using the five-hole Pitot/cone-static pressure probe four 0-15psi-range Omega model PX139-015A4V and one 0-100psi-range omega model PX139-100A4V transducers were used. Transducer specifications are given in Table 10. Calibration of each transducer and the detailed uncertainty analysis are described in Appendix B.

3.3.8 Traverse System

The traverse system consisted of a Linear Voltage Displacement Transducer (LVDT) with a signal conditioner, a stepper motor, a motor controller, a velmex bi-slide, mounting to hold the probe, and the horizontal rail for the manual horizontal traverse. Omega Model LD100-150 LVDT with nominal linear range 152.4mm was used to record the vertical position of the probe. The LVDT consisted of a precision variable inductor with frequency response up to 15khz, and an aluminum core that moved in a polyimide tube. The core movement transmitted equivalent amount of inductance to the signal processor, Omega Model SP200A. The raw voltage produced from the signal processor was linearly proportional to the inductance. The uncertainty of the LVDT was 0.07 mm.

3.3.9 High Temperature Thermocouple

For high temperature surface oil flow visualization, the pebble bed heater was equipped with two Omega model XTA-W5R26-U-125-30-H-HX-6 thermocouples. The maximum operating temperature of each thermocouple was 2300^0C. Thermocouple uncertainties, as specified by the manufacturer, were 0.4 ^{0}C.

3.3.10 Data Acquisition System

The data acquisition system contained an Analog to Digital (A/D) conversion card, an A/D board (16-channel TSI model ADCWIN-16), a Gateway2000 pentium PC, and the TestPoint software provided by the Keithley Instruments. A program in the TestPoint software environment was written to record the pressure and temperature data. For SOFV and PIV, the static and the upstream total pressure measurements were taken at a sampling rate of 1000 Hz for a total of 12000 points (tunnel runtime of 12 seconds). For the five-hole Pitot/cone-static mean flow measurement, a sampling rate of 1000 Hz was set for a total of 12000 points during the vertical traverse from on top of the missile model, and a total of 15000 points were set while traversing from on top of the test section floor.

4. EXPERIMENTAL METHODOLOGIES

4.1 Five-Hole Probe

The upstream total pressure $P_{t\infty}$, four cone surface pressures (P_{c1}, P_{c2}, P_{c3} and P_{c4}), and Pitot pressure (P_{t2}) were recorded. Two axial locations were selected for the mean flow measurement; one at 15.34 mm downstream of the injector center and the other was at 46.96 mm downstream in the wake region. At each axial location, the probe was traversed spanwise at 15 locations. The spanwise locations at the center of the test section were 0.318 cm apart. A FORTRAN program was written to post-process these raw voltage data. The program first averaged and calibrated the LVDT data. The program produced 180 data points across the height of about 4.7 cm from the test-section floor, where each point consisted of an average of 80 data samples.

Absolute pressure data were obtained using the transducer calibration equations (listed in Appendix B). For a range of different supersonic Mach numbers spanning that initially expected in the present experiments, the ratio of cone surface pressure (P_c) and Pitot pressure (P_{t2}) was obtained from the numerical solution of Taylor-Maccoll conical flow equation. The result is given in Table 11. From this theoretical result a least squares curve fit solution for the Mach number as a function of P_c/P_{t2} was obtained as

$$\frac{1}{M_1} = -1.424 + 24.873\left(\frac{P_c}{P_{t2}}\right) - 158.089\left(\frac{P_c}{P_{t2}}\right)^2 + 566.284\left(\frac{P_c}{P_{t2}}\right)^3 - 1124.770\left(\frac{P_c}{P_{t2}}\right)^4 + 1165.510\left(\frac{P_c}{P_{t2}}\right)^5 - 491.796\left(\frac{P_c}{P_{t2}}\right)^6 \qquad (4.1)$$

The Taylor-Maccoll conical flow solution was valid for attached shock, but the five-hole probe tip was blunt, so a detached shock wave was produced. Thus, the theoretical solution was not directly applicable. To minimize errors, experimental results were combined with the theoretical results and plotted in Fig. 14 for a range of available

Mach numbers 1.72, 3, 4, 5.0 and 5.5. Based on these data, a refined calibration equation was found as

$$M = (-0.0606\,M_1 + 1.2299)M_1 \qquad (4.2)$$

A comparative study on the results from the conical theory solution, normal shock solution and the recalibrated solution are shown in Table 12.

A FORTRAN program later computed other local mean flow quantities using the usual compressible flow relations [Anderson (1990)]. The Mach number contour, the upstream total pressure ratio ($P_{t1}/P_{t\infty}$) contour, and the downstream total pressure ratio ($P_{t2}/P_{t\infty}$) contour were plotted with Tecplot version 8.0. The upstream total pressure P_{t1} was found from the fundamental shock-wave relationships. The uncertainty associated with the Mach number measurement by the five-hole probe was estimated as ±0.13. The uncertainty calculations are described in Appendix B.

4.2 Pressure Sensitive Paint (PSP)

Pyrene based (PtOEP) pressure sensitive paint was used to map the surface pressure distribution over the missile model. The Pixelvision SpectraVideo CCD camera was used to capture the background, wind-off and wind-on images. For the 12-second tunnel run time, five images were taken. ISSI Inc. PSP_Analysis_2 software was used to average the images. Averaged background image was then subtracted from both the averaged wind-off and averaged wind-on images. The ratio of the subtracted wind-off and the subtracted wind-on images was then converted into the surface pressure. The PSP_Analysis_2 was also equipped with the calibration file, so that the software directly converted the ratio file into the surface pressure (psiA) using the estimated surface

temperature of about 10 ^{0}C (±5.0°). The overall uncertainty was 3.6% of the measured value (see Appendix B).

4.3 LaVision PIV

The LaVision Inc flowmaster3 PIV system was used to obtain axial and transverse velocity turbulence information. The measurements included longitudinal contours of the mean velocity field, the mean vorticity field, the mean shear streain rate field, velocity component turbulence intensities, turbulent stresses, Turbulent Kinetic Energy (TKE) and the mean dissipation. For each model tested, x-y plane contours were acquired at z = 0, 1.59mm, and 3.18mm. Davis 6.04 software (integrated with the PIV system) was used to acquire and process the Mie-scattering images. Due to the small lateral extent of the plumes, no particles were present in the plane located at z = 4.76 mm. The sonic model (model M1A at atmospheric pressure) and the Mach 3 model (model M3A-LP at pressures, 377 kPa and 694.3 kPa) were investigated using this PIV system. At each measurement location about 30 tunnel-runs were performed, where each run provided 40 instantaneous velocity field measurements. Due to continuous seeding, the smoke particles accumulated and liquefied inside the tubing. Images that were splashed with seeder oil were unusable. During image processing the contaminated images were deleted.

Davis6.04 software was used to obtain the instantaneous velocity field information at each run. Cross correlation mode was used to process the PIV images. Standard I1*I2 [via FFT, no zero padding] correlation function with 32 × 32 interrogation window size and 50% overlap were employed to obtain the vector field. The detailed

parameters that were set to process the raw images and to post process the vectors are presented in Table 13. The vector post processing was done in two steps. The filters were first applied to the instantaneous vector field, and then the vector length cut-off was used to obtain the correct instantaneous vectors. The valid vectors were then saved in ASCII data file format. Each data file consisted of 5120 (80 × 64) data points, corresponding to an image area of about 67 mm × 53 mm. The data files were then used to obtain the turbulence information using an in-house FORTRAN program that was written for this purpose.

The FORTRAN program first computed the average velocity at each grid point. The average was computed if the total number of valid vectors at a point exceeded the number of at least 70% of the total number of possible vectors at that point. To estimate the gradients in the transport equations a first order central difference approximation was used within the plume area and the forward and backward difference approximations were used at the plume upper and lower edges, respectively. The turbulence quantities were estimated using the following equations:

Instantaneous velocities	$u_i = \overline{u}_i + u_i'$	(4.3)
Mean Velocities	$\overline{u}_i = \frac{1}{n} \cdot \sum_n u_i$	(4.4)
Turbulent velocities	$\sqrt{\overline{u_i'^2}}$	(4.5)
Reynolds stresses	$\overline{u_i' u_j'}$	(4.6)
Vorticity	$\Omega_z = \left(\frac{\partial \overline{u}}{\partial y} - \frac{\partial \overline{v}}{\partial x} \right)$	(4.8)

Strain-Rate $$S_{xy} = \left(\frac{\partial \overline{u}}{\partial y} + \frac{\partial \overline{v}}{\partial x} \right) \quad (4.9)$$

The freestream velocity and missile diameter (D = 1.78 cm) were used to nondimensionalize the turbulence results.

5. FLOWFIELD RESULTS

The injector operating conditions are summarized in Tables 1, 6 and 7. The tunnel operating conditions are summarized in Tables 2 and 3. As indicated in Table 6, a wide range of injector conditions was examined. Of particular importance to the subsequent results is the effective backpressure ratio [Schetz and Billig (1967)] that varied over a range of 0.19-6.15, which indicated that underexpanded ($p_{eb}/p_\infty > 1$), perfectly expanded ($p_{eb}/p_\infty = 1$) and overexpanded ($p_{eb}/p_\infty < 1$) injection conditions were present. The majority of the low-blowing ratio cases studied here were overexpanded.

5.1 Flow Visualization

5.1.1 Surface Oil Flow Visualization (SOFV)

The flow surface interaction topologies were discerned from the Surface Oil Flow Visualization (SOFV) experiments. The salient flow features include (1) the missile body shock at the tip of the missile fuselage, (2) the boundary layer separation, (3) the jet interaction region, (4) the interaction shock, (5) the horseshoe vortex, (6) the re-compression shock and (7) the wake region. These features are annotated in Fig 15 for the sonic injection case at an MPR of 0.006. For this case, the jet exit is nearly perfectly expanded (effective back pressure ratios listed in Table 6 was very close to unity). In Fig. 15, the freestream flow is directed from left to right and the jet flow is directed outward from the paper. Flowfield symmetry is clearly depicted from the image. The missile-body shock angle of 24^0 was estimated from the image, while the shock angle calculated from conical theory was 23.8^0. When the crossflow, downstream of the missile shock, encountered the expansion edge of the missile fuselage, it deflected and marched parallel

to the cylindrical missile fuselage. The jet plume acted as an obstacle to the crossflow; this resulted in the boundary layer separation upstream of the jet and created the interaction shock. The round thick line of oil accumulation represents the separation line due to the interaction shock. The lambda shock in between the boundary layer separation point and the interaction shock cannot be identified in SOFV images. However, in shadowgraph and schlieren images (discussed later), the lambda shock is clearly distinguished. The next thin oil line that wrapped around the jet was interpreted as the horseshoe vortex [Everett et al (1998)]. Two other distinct oil lines were observed downstream of the jet. These lines were created due to the wake vortices [Fric and Roshko (1994)]. The crossflow stream that wrapped around the jet merged to create the compression shocks that appeared downstream of the jet.

A comparison of the SOFVs for model M1A is presented in Figs. 16(a – c). The flow features for this model at MPR 0.006 have already been discussed above; the jet total pressure used for this case was 101.35 kPa. Figure 16(b) shows the same model at an MPR of 0.005. This reduced MPR was achieved by operating the injector at a lower jet total pressure of 87.56 kPa. Although the jet flow in Fig. 16(b) was overexpanded (see Table 6), the surface flow features were very similar to those for an MPR of 0.006 [Fig. 16(a)]. Figure 16(c) shows the high temperature injection case. Again, the flow features are very similar to those in Fig. 16(a). Champigny and Lacau (1994) reported that higher jet temperatures shift the separation line further upstream, however in the present study, a 300% increase in the injection static temperature resulted in only a 4.0% increase in the boundary layer separation distance. The most likely cause for this discrepancy is that the low-blowing ratio data in Fig. 16 are either perfectly expanded or slightly overexpanded,

and most of the cases presented in the literature are for high blowing ratios, which are highly underexpanded. Underexpanded jets create larger upstream flow disturbances than overexpanded jets, thus the temperature effects are likely to be more significant. The separation distance is discussed in more detail later in this section.

The SOFV for model M3A-LP is presented in Fig. 17. Figure 17(a) corresponds to an MPR of 0.03 and Fig. 17 (b) to 0.06. For these two cases, the injector was significantly overexpanded. (see Table 6). The flow features are analogous to those seen for sonic injection case. The primary differences were observed are in the wake region. Specifically, the oil lines in Fig. 17(a) immediately downstream of the jet moved further apart while progressing downstream until about $2.5D_e$ from the injection port. Then, the two lines merged ($\sim 4.5D_e$ downstream of the exit) creating a diamond shaped structure.

The SOFV for model M3A-HP is given in Figure 18. High jet-to-freestream pressure ratios of 9.4 and 18.8 were used for this Mach 3 injector, which provided momentum ratios (MPR) of 0.05 and 0.09, respectively. Here, the jet flows were underexpanded. Aside from separation distance, the differences between the low and high MPR images were only discernible in the wake region. For the higher MPR, the jet penetration was higher, and the wake region developed further downstream. This is evident from the wake lines that moved downstream at small angle until about $10D_e$ downstream of the injector port [Fig 18(b)], and then the angle expanded outward indicating a developed wake region. However, for the low MPR case [Fig 18(a)], the small angle prevailed until about $7D_e$ downstream.

Like for the M3A-LP model, two momentum ratios, 0.03 and 0.05, were examined for the Mach 3.0 helium injection with model M3H. The results are presented in Figs

19(a and b), respectively. The SOFVs for model M3H in Fig. 19, strongly resembled those for model M3A-LP, as shown in Fig 17, where the injector operating conditions were matched. For this case, the use of helium resulted in an equivalent air injection temperature, based on velocity ratio, of 1250 K.

To simulate an even higher temperature air injection, the M1A injector was operated at MPR 0.015 with helium. Air was also used for comparative purposes. The use of helium simulated air injection at a temperature of 1900 K. Again, the injector operating conditions are summarized in Tables 6 and 7. Figures 19(c - d) present the air and helium SOFV, respectively. The flow structures looked similar. The impact of temperature on separation distance is discussed in the next paragraph.

The separate distances, as inferred from the SOFVs in Figs. 16-19, are summarized in Table 14. The uncertainties are described in Appendix B. Figure 20 presents the variation of the separation distance, normalized by injector diameter, with respect to the MPR, for all of the test cases. Overall, the expected trend of increasing of the separation distance with increasing MPR was observed. However, MPR alone is not a sufficient correlation parameter, where systematic increases in separation distance with increasing injection pressure and temperature were discerned. For example, the M3A-HP separation distances were significantly above the M3A-LP trend. An explanation for this trend can be found by referring back to Table 6. Specifically, the M3A-HP cases were underexpanded, and hence the plume expanded upon entering crossflow. Thus, the size of the obstruction increased, as compared to the M3A-LP case, where the flow was overexpanded. Figure 21 shows the variation in the separation distance (normalized by D_e) with the jet-to-freestream pressure ratio for the M3A models. Figure 22 shows the

effect of injection temperature on separation distance. Over the range of conditions tested here, the separation distance, for a given MPR, increased at a rate of approximately 0.013 with the jet-to-freestream temperature ratio. It is anticipated that if the high temperature jets were operated in an over expanded condition, the influence of temperature would have been more substantial.

5.1.2 Mie-Scattering Visualization

Mie scattering images were obtained for models M1A (MPR = 0.006) and M3A-LP (MPR = 0.03 and 0.06). Mie-scattering images were taken using both the ISSI and LaVision brand PIV systems. Due to the limitations discussed earlier, the former system was used only for the sonic model (M1A) for the flow visualization purposes.

Depicted in Fig. 23 is the Mie-scattering image of model M1A for the MPR of 0.006 obtained with the digital two-color PIV system. Figures 24 (a - c) show the Mie-scattering images for the same model with the LaVision PIV system at the three spanwise locations. The appearance of the plume was nearly identical as acquired by the two systems [comparing Fig. 23 to Fig. 24(a)]. Hence, the subsequent discussion will be in reference to the images obtained with the LaVision system. At about $6.5D_e$ downstream (visual inspection) of the injector port, the jet-plume surface interaction is clearly observed. Large-scale turbulence structures are clearly visible in these images. Figure 25 (a - c) presents the time-averaged Mie-scattering images for the sonic model at the three measurement planes. These data show the mean penetration and where the plume interacted with the missile fuselage.

The instantaneous and average images for the model M3A-LP are presented in Figs 26 - 27 (a – c) for an MPR of 0.06 at the three spanwise planes. The plume, upon exiting

the injector port, was turned downstream by an oblique shock cone. The terminating oblique shock system was also observed in the shadowgraph and schlieren images (next section). Figures 28 - 29(a – c) present the instantaneous and average Mie-scattering images for the model M3A-LP at lower MPR of 0.03. Due to lower MPR, the plume penetration was lower than that for the higher 0.06 MPR, which resulted earlier jet-surface interaction. For this case, the terminating oblique shock was almost normal to the jet exit port; this was also observed in shadowgraph images discussed in the next section. The importance here is that the overexpanded flow structure turned the flow downstream, and thus reduced the angle and size of the jet plume induced flow blockage. This explains the above observed difference in the shock separation distance when comparing the underexpanded and overexpanded cases.

5.1.3 Schlieren/ Shadowgraph Images

Shadowgraph and schlieren images were acquired for qualitative assessment of the shock structures for the different injectors. The salient features in the images include (1) the structure of the missile body shock, (2) the interaction shock, (3) the lambda shock, (4) the recompression shock, and (5) the exit port shock structure (barrel shock for underexpanded injection and the shock cone for the overexpanded condition). Also noticeable were weak waves (close to the freestream Mach angle) that were generated due to the surface imperfections in the nozzle and test section. The shadowgraph and the schlieren images are presented in Fig 30(a - j) and Fig. 31 (a - f), respectively. The flow features (annotated in the figures) are identical in both the shadowgraph and schlieren images. Both air and helium injection models (M1A, M1A-L, M3A-HP, M3A-LP, and M3H) were examined using the shadowgraph technique. Because of the strong similarity

between the shadowgraph and schlieren images, schlieren photographs were only acquired for the M1A, M3A-LP, and M3A-HP models. In Figs. 30 and 31, the freestream flow was from right to left, and the jet flow direction was vertically upward in the positive y-direction. The wave angles at the nozzle exit in the images (19.5-20.0 degrees) agreed well with the Mach wave angle of 19.7 degrees. The left images in each row correspond to the lower MPR case. With the exception of model M3A-HP, jet plume barrel-shocks were not visible in the images. Instead, the plume was terminated by the oblique conical shock system. A barrel-shock and Mach disk are faintly visible in the high-pressure model M3A-HP schlieren [Fig. 31(f)]].

5.2 Mean Flow Measurements

5.2.1 Five-hole Probe

The five-hole probe was used to measure the Mach number contours, and the pressure ratio contours (P_{t2}/P_{t1}, $P_{t2}/P_{t\infty}$, $P_c/P_{t\infty}$, and $P_{t1}/P_{t\infty}$) in two transverse locations, 15.34 mm and 46.96 mm downstream of the injector port. The coordinate axes and key flow features are labeled in the Mach number contours of model M1A [Fig 32(a)]. The contour plots, for both the upstream and downstream measurement locations, are drawn in the same coordinate axes to better display the flowfield evolution. The freestream flow in all of these contour plots is from left to right; the jet flow is in the positive y-direction with the injection port centered at (0,0,0); the co-ordinate axes are labeled in inches. The M3H model was not examined using five-hole probe because the presence of helium contaminates the probe Mach number calculation.

Presented in Figures 32 are the Mach number contour plots for models M1A (MPR = 0.006, 0.005), M3A-LP (MPR = 0.03, 0.06), and M3A-HP (0.05, 0.06); these cases correspond to nearly perfectly expanded, underexpanded and overpanded, respectively. Figures 33 - 36 present pressure ratio contour plots (P_{t2}/P_{t1}, $P_{t1}/P_{t\infty}$, $P_{t2}/P_{t\infty}$ *and* $P_c/P_{t\infty}$ respectively) of models M1A, M3A-LP, and M3A-HP. At the upstream location, the flow features are very distinct and uniform. The general flow features are annotated in Fig. 32 (a), which presents Mach number contour of model M1A at MPR 0.006. The wake region, jet plume area, and the interaction shock are labeled in the figure. The flow features are identical in the pressure ratio plots. The plume and the interaction shock locations were verified with the Mie-scattering and shadowgraph images. The horseshoe vortices at both sides of the jet plume near the missile surface were also noticeable. A small region in the wake at the upstream station was manually set to zero because of flow reversal that caused lower Pitot pressures (P_{t2}) than the cone static pressures (p_{c1}, p_{c2}, p_{c3}, or p_{c4}), which in turn resulted erroneous Mach number and pressure ratio estimations. However, Figs. 35–36 present the five-hole probe measurements (Pitot and cone-static pressures, $P_{t2}/P_{t\infty}$ *and* $P_c/P_{t\infty}$) without any modification. The pressure ratios as normalized by the freestream total pressure, eliminate the errors associated with the stagnation pressure control deviations.

The contour plots for model M1A at MPR 0.005 and model M3A-LP at MPR of 0.03, demonstrated similar flow features to those as described above. Presented in Fig 32 (d) is model M3A-LP at MPR 0.06, where the flow features were similar to those as seen in the sonic injection case, except the interaction shock was at an elevated location, which

indicated higher penetration for the Mach 3 injection case. At the downstream location, the wake merged with the plume to create a large circular region of low Mach number.

Mach contours for model M3A-HP can be seen in Figs 32 (e – f). Due to the high-pressure injection, the penetration height increased and the interaction shocks were observed only at the upstream location. In the downstream contour, the plume shape was not clearly discernable, and the wake region appeared to be the most prominent structure. This result was evident for the higher penetration of the plume. The low MPR model M3A-LP mean flow was more complicated in the downstream location. This was because the jet remained confined close to the surface, which caused irregular and complicated surface interactions.

5.2.2 Pressure Sensitive Paint (PSP)

The pressure sensitive paint contours for the same cases discussed above, with the addition of the M3H case, are shown in Figs. 37-40. The freestream flows from top to bottom in all the images. A common scale with a range from 0 to 6 psiA was employed for all models, so that direct comparisons could be made. The entire painted image area was 35.56 mm × 83.35 mm. This region covered about 29.7 mm upstream and about 53.7 mm downstream of the injection center. The images were taken through the ceiling of the test-section, so a two-dimensional projection of the curved surface (missile fuselage) was imaged onto the CCD camera.

The general flowfield features, such as boundary layer separation point, interaction shock, horseshoe vortex, and the low-pressure wake region, are labeled in Fig 37. Surface pressure contours for the model M1A at MPR 0.006 and 0.005 are shown in the figure. Two high-pressure regions upstream of the jet were observed, which is

consistent with Gruber et al (1997). The compression due to the interaction shock and the horseshoe vortex created these high-pressure areas. Upstream of the interaction shock, boundary layer separation occurred, and thus a re-circulation region was created, which can be seen as the first thick semicircular high pressure region upstream of the jet. For model M1A, the surface pressure upstream of the boundary layer separation point was measured higher (13.92 kPa) compared to the other models, which was due to the higher tunnel stagnation pressure (724 kPa) for this case.

Figures 38 - 39 show the surface pressure contours for models M3A-LP and M3A-HP, respectively. In each figure, the first image corresponds to the low MPR case and the second image is for the high MPR injection. The pressure contours for all the models are qualitatively similar. However, the pressure in the separation region was observed to increase with increasing MPR (injection pressure), and the boundary layer separation point moved further upstream with increased MPR. The size of the wake region and the decrease in the wake pressure both increased with increasing MPR.

Figure 40 shows pressure contours for model M3H with helium injection. Because of the potential inaccuracies due to the presence of helium on the oxygen sensitive probe molecules, the pressure results for model M3H are considered qualitative. The jet MPR and jet total pressures used for this model are identical with model M3A-LP. As discussed earlier, helium as a lighter gas was expected to simulate higher temperature air injection. It can be gleaned from the PSP images that, the boundary layer separation occurred at almost the same location in absolute distance as seen with the model M3A-LP, but the jet exit diameter for model M3H was about 16% lower than

model M3A-LP. The high-pressure region near the interaction shock is much thinner in model M3H. A larger low-pressure wake region is also observed in model M3H.

Plotted in Figs. 41(a - d) are the centerline axial pressure profiles. The figures compare the effect of MPR on the pressure distribution for the same injector geometry, same injectant, and the same injection Mach number. Two high-pressure peaks upstream of the jet were observed, as discussed earlier these peaks resulted from the compression due to the interaction shock and the horseshoe vortex. Previous studies [Champigny and Lacau (1994), Graham et al (1999), Hsieh (1995), Graham et al (2000)], both experimental and numerical, demonstrated similar trends in the longitudinal surface pressure distribution. The data plotted in this format provides a clearer documentation of the trends listed in the previous paragraph. Also from these data, the recompression shock appeared to move downstream for higher values of MPR.

Figure 42 compares the effect of jet-to-freestream pressure ratio on the surface pressure for the models M3A-LP at MPR 0.06 and M3A-HP at MPR 0.05. Due to significantly different injector geometry, this comparison was not quite justifiable. However, the shapes of the curves were qualitatively similar.

The jet interaction performance is generally expressed in terms of the force amplification factor [Champigny and Lacau (1994)], K_F. The amplification factor is defined by the ratio of the total reaction force (F) and the total jet delivered force (F_j) at the freestream pressure. For the present study, the following relations were used

$$F = \dot{m}_j v_j + \left(p_{ej} - \bar{p}_e\right) \cdot A_e + p_{avg} \cdot \left(A_{total} - A_e\right) \tag{5.1}$$

$$F_j = \dot{m}_j v_j - p_\infty A_e \tag{5.2}$$

$$K_F = \frac{F}{F_j} \tag{5.3}$$

$\dot{m}_j v_j$ is the jet momentum; p_{ej} is the jet exit pressure; $\overline{p}_e$ is the average pressure around the circumference of the exit port; p_{avg} is the average pressure on the entire painted image; A_{total} is the total painted area that was used to plot the surface pressure contour, and p_∞ is the freestream pressure.

The jet thrust force coefficient (C_F), defined here as the force in Eqn. 5.1 normalized by the freestream dynamic pressure force ($\rho_\infty u_\infty^2 A_b / 2 = \gamma p_\infty M_\infty^2 A_b / 2$) is plotted in Fig. 43 against the jet MPR. An almost linear increase in the jet thrust force with increasing of MPR was evident from these data, where $C_F \approx 0.76 MPR$. The helium data are inaccurate, and hence omitted; the presence of helium results in a lower concentration of oxygen for a given pressure, which results in an erroneous pressure reading. The amplification factor (K_F) was computed as listed in Eqns 5.1-5.3. The resulting data had hyperbolic shape. Hence, $1/K_F$ is plotted in Fig. 44, and the trend is very nearly linear, where $K_F \approx 0.29 / MPR$.

5.2.3 Particle Image Velocimetry (PIV)

PIV measurements were performed for the models M1A (MPR = 0.006) and M3A-LP (MPR = 0.06 and 0.03). Seeder pressure limitations prohibited measurements for the underexpanded cases. The PIV measurements were obtained in *x-y* planes at three spanwise locations (z = 0 mm, 1.59 mm, and 3.18 mm, respectively). The mean flow measurements include the mean velocity, vorticity and strain rates (see Chapter 4). The data were nondimensionalized with the missile diameter and the freestream velocity.

The total number of images (i.e., samples) used to obtain the statistical averages for model M1A was nominally 1200 (varied from 1173-1204 across the three on measurement planes). For the model M3A-LP, the number of images ranged from approximately 500-800. This lower number of samples was due to difficulties associated with pressurizing the seeder for the Mach 3 injection. The contours were plotted on 5120 (80 × 64) grid points, where each cell was 0.85 mm × 0.85 mm in size. The average at each point in the domain was computed with at least 70% of the total number of valid vectors.

The mean velocity contours for the three measurement planes are summarized in Figs. 45-50. The freestream flow is from left to right. The jet flow is vertically upward and the injector center is located approximately at $x = 0.0$, $y = 0.0$, and $z = 0.0$. For model M1A (Figs. 45 and 46), the maximum average velocity ratio $\overline{u}/u_{\infty}$ in the plume was measured at approximately 0.97. The maximum vertical velocity ratio $\overline{v}/u_{\infty}$ in the jet plume was measured at about 0.33 near the jet exit. Thus, the sonic velocity at the jet exit was confirmed. For model M3A-LP at MPR 0.06 (Figs. 47 and 48), the maximum average velocity ratio in the freestream direction was again about 0.97. The vertical velocity, normalized by the freestream velocity was measured as about 0.32 after the terminating oblique shock. The maximum velocity ratio of 0.97 – 0.99 was obtained for the model M3A-LP at MPR 0.03 (Figs. 49 and 50) in the freestream direction.

Focusing on the mean axial velocity contour for model M1A [i.e., Fig. 45(a)], a relatively large region of high velocity flow was seen to emanate from $x \approx 15$ mm and $y \approx 6$. The lower boundary of this region extends to the contour maximum ($x \approx 53$ mm, $y \approx 10$), and upper bound reaches the plume edge at $x \approx 25$. Similar regions with slightly

different boundaries were seen for the two off centerline planes [Figs. 45(b) and (c). The flow accelerated forward of this region. Below this region (between the plume core and the wake), a strong velocity gradient was present. The vertical velocity component (Fig. 46) demonstrated was more interesting. First, along the centerline [Fig. 46(a)], the vertical velocity was positive coming out of the injector and remained positive along the upper edge until $x \approx 40$, $y \approx 15$. The lower boundary (almost a line between extending from $x \approx 4$, $y \approx 3$ to $x \approx 40$, $y \approx 15$) of the positive vertical velocity is clearly indicated on the contour. A trapezoidal region of negative velocity existed below the upper region of positive velocity; this region approximately coincides with the recompression shocks seen in the shadowgraph. Lastly, below this negative (downward) velocity region is a lower, aft triangular region of upward velocity. Moving outward in the spanwise direction [i.e., moving from Fig. 46(a) to (c)], a large negative flow region forms along the missile fuselage ($y \approx 0$), which indicates that flow moved down and around the fuselage. Models M3A-LP (MPR = 0.06 and 0.03) displayed similar trends. The main difference was the clearly defined line of downward velocity (e.g., the region centered on the line between $x \approx 25$, $y \approx 10$ and $x \approx 53$, $y \approx 18$) that coincided with the recompression shocks.

Mean vorticity contours, normalized by D/u_∞, are shown in Figs 51-53. For model M1A (Fig. 51), slightly negative/clockwise rotation (~ -0.7) about the z-axis was observed along the upper edge of the plume, and anti-clockwise rotation of approximately 5 - 10 was seen along the bottom edge of the plume. Both clockwise and anti-clockwise rotation increased at the off-centerline planes. However, the highest rotation was observed near the trailing edge of the barrel shock, where the plume turned toward the freestream direction. For model M3A-LP at MPR 0.06 (Fig. 52), a slight

rotation (<1.0) was observed along the plume core. The highest rotation was near the oblique shock where the plume suddenly turned toward the freestream direction. For model M3A-LP at MPR 0.03 (Fig, 53), the highest rotation was near the bottom of the plume. Slight (-0.2 to –0.7) clockwise rotation was observed near the upper edge of the plume; near the jet exit higher clockwise rotation (-1.7 to –0.5) existed.

The mean shear strain rate plots, normalized by D/u_∞, are shown in Figs 54-56. Common attributes for all cases were (1) the high positive shear strain rate just above the jet exit, (2) the high positive shear strain near the surface downstream of the injector, (3) negative strain along the upper boundary of the plume, (4) the relatively low magnitude shear in the upper half of the plume core, and (5) relatively high positive strain downstream of the recompression shock. These strain rate observation tie closely to the turbulence discussion below.

5.3 Turbulent Flow Measurements (PIV)

Turbulent statistical flow properties were obtained from the PIV data described in Section 5.2.3. The statistical properties include the velocity component turbulence intensities and the turbulent shear stresses. The data were normalized by the freestream velocity.

5.3.1 Turbulence intensities

The turbulence intensity contours for model M1A (MPR 0.006) are given in Figs. 57 and 58. Focusing first on the axial component along the tunnel centerline [Fig. 57(a)], the jet flow produced high levels of turbulence just above the jet exit port. Progressing downstream, the turbulence levels form three distinct regions. Region 1 corresponds to

the upper edge of the plume, were the turbulence levels were nominally 5.0%. Region 2 was defined here as the high turbulence region along the lower edge of the plume that appears to be connected to the high level turbulence at the jet exit. In this region, the turbulence levels were approximately 15.0-20.0%. The third region was comprised of the plume core, where in the upper half, the turbulence levels were very low (1.0–3.0%), and moving down towards the missile fuselage ($y = 0$), the level increased to those in region 2. Referring back to Fig. 54, these regions coincided with regions of high and low strain rate, which is indicative of a strain rate turbulence level causal relationship. Specifically, turbulence was produced in region 1 due to the shear layer between the plume and the tunnel crossflow. The low levels in region 3 were the result of low strain (Fig. 54) and potentially turbulence stabilization due to the rotation associated with the counter rotating vortex pair. In region 2, the strain rates were the largest, and thus, the turbulence production was expected to be the largest. In addition, region 2 corresponds to the low-pressure wake, which ingested highly turbulent low momentum boundary layer fluid.

The trends described for Fig. 57(a) prevailed for the two off-centerline contours [Figs. 57(b) and (c)] as well. However, the levels in the three regions varied. At $z = 1.59$ mm, the average turbulence was about 5 percent at the upper edge and about 30.0% along the bottom edge. At $z = 3.18$ mm, the region 1 levels were about 10.0-15.0%, the region two levels were nominally 30.0% along the bottom edge.

The contour plot of the vertical component of the turbulence is presented in Figs 58 (a – c). The overall structure was found to be similar to that in Fig. 57. However, the transverse levels were in general 50-70% lower than the axial levels.

The turbulence velocity contours for the Mach 3 model M3A-LP (MPR 0.06 and 0.03) is presented in Figures 59 – 62. Again, the overall structure was similar to that described in regards to Figs. 57-58, where the high concentration of turbulence at the jet exit and the three regions were observed.

5.3.2 Turbulent Stresses

The turbulent stress contours (normalized by the freestream velocity squared) for the sonic injection (model M1A, MPR 0.006) are plotted in Figs 63 –65. The normalized Reynolds shear stress ($\overline{u'v'}/u_\infty^2$) contour [Fig. 63(a)] showed the same overall structure as described in regards to Fig. 57. However, here the signs were significant. Just above the injector port the turbulent shear stresses was positive at the peak positive values. In region 1, the shear stresses start out positive, but progressing downstream, the values became negative [this trend was most clearly seen in Fig. 63(c), however it was present for all three locations]. Region 2 contained highly negative shear stress levels. The highest negative values appeared in downstream region (x > 30 mm); the recompression shock occurs in this region. The second measurement plane [Fig. 63 (b)] shows similar structure with lower peak intensities. Also, the peak negative intensity in region 2 was further upstream than along the centerline. At the third measurement plane [Fig. 63(c)], the peak negative shear stresses in region 2 were further upstream than for the second plane. Hence, the peak shear levels in region 2 progressed downstream as the flow wrapped around the missile. Again, a strong qualitative correlation between the shear strain and the turbulent shear stress was observed. The axial and transverse shear stress contours (Figs. 64 and 65) mimic those for the turbulence intensity plots.

The normalized turbulent shear stresses for Mach 3 model M3A-LP (MPR = 0.06 and 0.03) are contoured in Fig. 66 –71. Overall, the turbulent shear stress structure for the Mach 3 was similar to the sonic model. Aside from magnitude differences, the only discrepancy was found at the centerline plane for the model M3A-LP at MPR 0.06. The shear stress structure shows complicated structure with both positive and negative high-intensities along the plume edges near the surface (region 2). This was most likely the result of only using about 500 samples to achieve these second order statistics.

5.3.3 Turbulent Kinetic Energy

A 2-D turbulent kinetic energy was defined here as $(\overline{u'^2}+\overline{v'^2})/2u_\infty^2$. The resultant plots for Models M1A (MPR = 0.006), M3A-LP (MPR = 0.06) and M3A-LP (MPR = 0.03) are shown in Figs. 72 – 74. Because these TKE was constructed from the normal stresses, the trends in the TKE echo those previously discussed in regards to the turbulence intensities and normal stresses.

6. CONCLUSIONS AND PUBLICATIONS

The development flight control methods for Army supersonic missiles at low altitudes using low blowing ratio reaction jets is complicated by (1) nonlinear, counterintuitive surface interactions, (2) hot gas effects and (3) poor predictability using modern computation fluid dynamic codes, where turbulence modeling is a key factor limiting the accuracy. The objectives of this research, which were directly tied to the Army low blowing ratio reaction control jet requirements, were documentation and improved understanding of (1) the surface flow interactions with hot gas effects and (2) the turbulent flow structure in the plume. To meet these objectives, an experimental analysis of the mean and turbulent flow properties for sonic and Mach 3 injection into a Mach 3 freestream was accomplished. The range of conditions included: MPR = 0.005-0.09, p_j / p_∞ = 0.6-19.0, T_j / T_∞ = 1.0-13.6 (helium was used to simulate the highest temperature), γ = 1.4 and 1.67, and p_{eb} / p_∞ = 0.19-6.15 (overexpanded, perfectly expanded and underexpanded jets were tested). Numerical simulations were not accomplished in the present effort. However, a full characterization of the high-speed jet interaction flowfield over a blended body missile fuselage (sharp-coned cylinder) was experimentally achieved, where specific pragmatic and scientific flowfield conclusions were drawn. The conclusions, which are separated into three categories based on measurement technique (flow visualization, mean flow, and turbulent flow), are summarized below.

6.1 Flow Visualization

Quantitative and qualitative information concerning the flow topology, e.g., the locations of the interaction shock, horseshoe vortex, recompression shock, and wake region, were discerned from the flowfield visualizations. From these data, the following observations were deemed important. First, the surface oil flow visualization provided qualitative insight into the surface topology and quantitative measurement of the upstream separation distance, which have important implications relative to the amplification factor for flight missiles. From the surface oil flow visualizations, the following conclusions were drawn:

- Injection temperature, for a given MPR, had a small but discernible effect on the boundary layer separation distance, where for a given MPR, the separation distance increased with temperature ratio at a rate of approximately 0.013. This increase was smaller than expected from previous overexpanded studies, however the present high temperature cases were all overexpanded, and hence the upstream influence was smaller.
- The boundary layer separation increased significantly with MPR, however MPR was not a sufficient correlating parameter. For example, for a given MPR, the separation distance increased when the jet condition transitioned from overexpanded to underexpanded.
- The influence of the jet plume on the surface pressure distribution in the wake region of the flow was found to depend on MPR, where the wake region developed further downstream in terms of distance nondimensionalized by the jet exit diameter.

Second, the shadowgraph and schleiren photographs provided documentation of the shock structure along the flow centerline. The following observation were drawn from the shadowgraph and schlieren images:

- The effective backpressure concept was an accurate indicator of the jet flow condition (overexpanded versus underexpanded), where, for example, a terminating Mach cone was observed for all of the cases that were deemed overexpanded using this criterion.
- The jet interaction bow-shock strength increased with increased MPR.
- For a given MPR, overexpanded jets produced weaker shocks than underexpanded jets, where the overexpanded shock structure turned the flow downstream, thus lessoning the flow disturbance.

Third, the Mie-scattering flow visualizations provided qualitative insight into the turbulent structure of the plume, the location of the plume surface interaction and the penetration of the plume into the crossflow. The following observations were deemed important:

- Large-scale turbulent structures were present in the plumes.
- The surface interaction location moved closer to the jet exit with decreasing MPR.
- The penetration height increased with increasing MPR.

6.2 Mean Flow

Detailed mean flow documentation was achieved with pressure sensitive paint, the five-hole pressure probe and particle image velocimetry. First, The PSP images provided both qualitative flow visualization and quantitative mean surface static pressure measurements. From the PSP data the following observations were drawn:

- The upstream peak pressures associated with lambda shock and the horseshoe vortex increased with increasing MPR.
- The wake pressures decreased with increasing MPR (or injection pressure).
- The interaction force increased with almost linearly increasing MPR (i.e., $C_F \approx 0.76 \cdot MPR$).
- The amplification factor was inversely proportional to MPR (i.e., $K_F \approx 0.29 / MPR$).

Second, the five-hole probe provided the detailed contours of Pitot pressure, Mach number, total pressure, and static pressure. From the five-hole probe, data the following additional conclusions were drawn

- The mean flow features (plume, wake region, interaction shock, counter rotating vortex pair and the horseshoe vortex) were documented.
- The counter-rotating-vortex pair became more prominent with increasing MPR.

Third, the PIV provided the contours of the mean velocity, z-component of vorticity, and mean x-y shear strain rate at three z-locations for models M1A (MPR = 0.006), M3A-LP (MPR = 0.03 and 0.06). From the PIV data, the following observations were drawn:

- The mean axial and transverse velocity components across the plume were influenced by both the plume vorticity and surface curvature, where in the upper region of the plume where the counter rotating vortex pair resided, the axial velocity peaked a value nearly that of the freestream, and the data showed that jet fluid moved down and around the missile fuselage.
- Clockwise vorticity (z-component) was observed along the upper edge of the plume, while anti-clockwise vorticity was observed near the bottom edge of the plume.
- The shear strain rate fields were complicated, where a region of high positive shear strain rate was seen in the jet plume just above the injector port, where the plume first interacted with the high momentum crossflow. A layer of high shear strain rate existed along the missile fuselage. The shear strain had relatively low magnitudes in the upper half of the plume core, and it increased across the recompression shock.

6.3 Turbulent Flow

Turbulent flowfield was documented with PIV for models M1A (MPR = 0.006), and model M3A-LP (MPR = 0.03 and 0.06). The measurements included velocity component turbulent intensities, turbulent stresses, and turbulent kinetic energy. From these data, the following conclusions were made:

- In general, progressing downstream, the turbulence levels formed three distinct regions across the plume.
    - Region 1 was defined as the upper region of the plume where the turbulence levels were moderate (turbulence intensities ~ 5.0-10.0%). In this region, the Reynolds shear stress started out positive and transitioned to negative progressing downstream.
    - Region 2 was defined as the high turbulent level (turbulence intensities ~ 15.0-30.0%) region located along the lower portion of the plume near the missile fuselage. The Reynolds shear stresses had large magnitude negative values in this region.
    - Region 3 was defined as the relatively low turbulence region along the plume core, where in the upper half, the turbulence levels were very low (turbulence intensities ~ 1.0–3.0%), and moving down towards the missile fuselage, the levels increased to those in region 2.
- The moderately high turbulence levels in region 1 were due production that resulted from the strain rates across the shear layer between the plume and the tunnel crossflow.
- In region 2, the strain rates were the largest, and thus, the turbulence production was expected to be the largest. In addition, region 2 corresponded to the low-pressure wake, which ingested highly turbulent low momentum boundary layer fluid.

- The low levels in region 3 were the result of low strain rates and turbulence stabilization due to the rotation associated with the counter rotating vortex pair.
- The present data suggest a strong qualitative correlation between the shear strain rate field and the turbulence across the plume. This finding supports the usage of the Boussinesq turbulence model approximation.

6.4 Publications

The following two conference papers were generated from a subsection of the results described above:

- Mahmud, Z. and Bowersox, R., "Supersonic Missile Body Jet Interaction Flowfields at Low Momentum-Ratio-Parameter," to be presented at the 41st AIAA Aerospace Sciences Meeting, Reno NV, Jan 2003.
- Mahmud, Z., and Bowersox, R., "Experimental Investigation of Low Blowing Ratio Blended Body Supersonic Injection Flowfields," AIAA 2001-0886, 39th AIAA Aerospace Sciences Meeting, Reno NV, Jan 2001.

REFERENCES

Anderson J.D., *Modern Compressible Flow With Historical Perspective,* 2nd edition, McGraw-Hill Inc, 1990.

Billig F.S., Orth R.C. and Lasky M., "A Unified Analysis Of Gaseous Jet Penetration," *AIAA Journal*; Vol. 9, No. 6, June 1971, pp. 1048-1058.

Billig F.S. and Schetz, J.A., "Penetration And Mixing Of Gas Jets In Supersonic Cross Flow," *AIAA Journal*, Vol. 32, No 7, Feb 1994, pp.1533-1535.

Bowersox, R.D.W., "Turbulent Flow Structure Characterization of Angled Injection in a Supersonic Cross Flow," *Journal of Spacecraft and Rockets*, Vol. 34, No. 2, 1996, pp. 205-313.

Bowersox R. D. W., "Combined Laser Doppler Velocimetry and Cross-Wire Anemometry Analysis for Supersonic Turbulent Flow," *AIAA Journal*, Vol. 34, No. 11, November 1996, pp. 2269-2275

Bradshaw P., "The Effect Of Initial Conditions On The Development Of A Free Shear Layer," *Journal of Fluid Mechanics* (1966), Vol. 26, Part 2, pp. 225-236.

Brandeis J. and Gill J., "Experimental Investigation of Super- and Hypersonic Jet Interaction on Missile Configurations," *Journal of Spacecraft and Rockets*; Vol. 35, No. 3, May-June 1998, pp. 296-302

Chamberlain R., Dang A. and McClure D., "Effect of exhaust chemistry on reaction jet control," AIAA-99-0806, *37th AIAA Aerospace Science Meeting and Exhibit*, Jan 11, 1999, Reno, NV.

Chamberlain, R., McClure, D., and Dang, A., "CFD analysis of lateral jet interaction phenomena for the THAAD interceptor," AIAA Paper 2000-0963, 38th AIAA Aerospace Sciences Meeting and Exhibi, Reno, NV, Jan. 10-13, 2000.

Champigny P. and Lacau R. G., "Lateral Jet Control For Tactical Missiles," *AGARD Special Course on Missile Aerodynamics*, June 1994.

Chenault, L., Beran, P., and Bowersox, R., "Second-Order Reynolds Stress Turbulence Modeling of Three-Dimensional Oblique Supersonic Injection," *AIAA Journal,* Vol. 37, No. 10, 1999, pp. 1257-1269.

Dash S.M., Perrell E. R., Kenzakowski D.C., Chidambaram N. "Turbulent Effects On Missile Lateral Control/Divert Jet Interactions," *37th AIAA Aerospace Sciences Meeting and Exhibit*, Jan 11 1999, Reno, NV.

Doligalski, T., *Personal Communication*, ARO, 1997.

Everett D. E., Woodmansee M. A., Dutton J. A., and Morris M. J., "Wall Pressure Measurement For A Sonic Jet Injected Transversely Into A Supersonic Crossflow," *Journal of Propulsion and Power*, Vol. 14, No. 6, Nov-Dec 1998.

Findlay M. J., Salcudean M., and Gartshore I. S., "Jets In A Crossflow: Effects Of Geometry And Blowing Ratio," *Journal of Fluids Engineering*, ASME, June 1999, Vol 121, pp. 373-378

Fric T. F. and Roshko A., Vortical Structure in The Wake of a Transverse Jet; *J. Fluid Mech.*, Vol. 279, 1994, pp. 1-47.

Gogineni S., Goss L. P., Pestian D. and Rivir R., "Two-Color Digital PIV Employing A Single CCD Camera," *Experiments in Fluids*, Vol. 25, 1998.

Graham M. J. and Weinacht P., "Numerical Simulation Of Lateral Control Jets," *37th AIAA Aerospace Sciences Meeting and Exhibit*, Jan 11 1999, Reno, NV.

Graham M. J. and Weinacht P., "Numerical Investigation of Supersonic Jet Interaction for Axisymmetric Bodies," *Journal of Spacecraft and Rockets*; Vol. 37, No. 5, September-October 2000, pp. 675-683

Grasso F. and Magi V., "Simulation Of Transverse Gas Injection In Turbulent Supersonic Air Flows," *AIAA Journal*, Vol. 33, No.1, Jan 1995, pp. 56-60.

Gruber M.R., Nejad A. S. and Goss L. P., "Surface Pressure Measurements In Supersonic Transverse Injection Flowfields," *33rd AIAA Joint Conference*, July 1997, Seattle, WA.

Heister S. and Karagozian A., "The Gaseous Jet In Supersonic Crossflow," *AIAA 25th Joint conference*, AIAA 89-2547, July, 1989.

Hsieh T., "Analysis Of The Scaling Effects For Missile Configuration With Lateral Thruster," *37th AIAA Aerospace Sciences Meeting and Exhibit*, AIAA-99-0810, Jan 11, 1999, Reno, NV.

Kamotani Y. and Greber I., "Experiments On A Turbulent Jet In A Cross Flow," *AIAA Journal*, Vol. 10, No. 11, Nov 1972, pp. 1425-1429

Keffer J.F., Baines W. D., The round turbulent jet in a cross-wind; *Journal of Fluid Mechanics*, Vol 15, 1963, pp. 481-496

Kikumoto K., Sentoh E., "Sidejet Aerodynamic Interaction Effects of the Missile," *AIAA Journal*, Vol. 39, No. 4, April 2001, pp.611-617

Margason R. J., "Fifty Years of Jets in Cross-Flow Research," *AGARD-CP-534*, Nov. 1993, pp1.1-1.41.

McCann*, G., and Bowersox, R., "Measurements Across the Plume of a Low-Angled Supersonic Gaseous Injection into a Supersonic Free Stream," *AIAA Journal,* Vol. 34, No. 2, 1996, pp. 317-323.

Moussa Z.M., Trischka J. W. and Eskinazi S., "The Near Field In The Mixing Of A Round Jet With A Cross-Stream," *Journal of Fluid Mechanics*, Vol 80, Part 1, 1977, pp. 49-80.

Naumann K.W.,Ende H., Mathieu G. and George, A., "Experiments On Interaction Force Of Jets In Hypervelocity Cross-Flow In A Shock Tunnel," *AGARD Meeting On Computational And Experimental Assessment Of Jets In Cross Flow*, April 1993.

Papamoschou D. and Roshko A., "The Compressible Turbulent Shear Layer: An Experimental Study," *Journal of Fluid Mechanics*; (1988), Vol.197, pp. 453-477.

Perry A.E., Kelso R. M. and Lim T. T., "Topological Structure Of A Jet In A Cross Flow," *AGARD Meeting On Computational And Experimental Assessment Of Jets In Cross Flow*, April 1993.

Roger R.P., "The Aerodynamics Of Jet Thrusted Control For Supersonic/Hypersonic Endo-Interceptors: Lessons Learned," *37th AIAA Aerospace Sciences Meeting and Exhibit*, AIAA-99-0810, Jan 11, 1999, Reno, NV.

Samimy M., Erwin D. E. and Elliott G. S., "Compressibility And Shock Wave Interaction Effects On Free Shear Layers," *AIAA/ASME/SAE/ASEE 25th Joint Propulsion Conference*, Monterey, CA July10, 1989.

Samimy M. and Elliott G. S., "Effects of Compressiblity on the Characteristics of Free Shear Layers," *AIAA Journal*, Vol. 28, March 1990, pp. 439-445.

Samimy M., Reeder M. F. and Elliott G. S., "Compressibility Effects On Large Structures In Free Shear Flows," *Phys. Fluids* A 4(6), June 1992, pp. 1251-1258.

Santiago J.G. Dutton J. C., "Velocity Measurements For A Sonic Underexpanded Tranverse Jet Into A Supersonic Flow," AIAA 95-0525, *3rd Aerospace Sciences Meeting and Exhibit*, Jan 1995, Reno, NV.

Schetz J.A. and Billig F.S., "Penetration Of Gaseous Jets Injected Into A Supersonic Stream," *Journal of Spacecraft*, Vol. 3, Sep 1966, pp. 1658-1665

Schetz Joseph A., Hawkins P. F. and Lehman H., "Structure Of Highly Underexpanded Transverse Jets In A Supersonic Stream," *AIAA Journal*, Vol. 5, May 1967, pp. 882-884.

Schetz Joseph A., Weinraub R. A. and Mahaffey R. E., "Supersonic Transverse Injection Into A Supersonic Stream," *AIAA Journal*, Vol. 6, No. 5; 1968, pp. 933-934.

Srivastava B., "Computational Analysis and Validation for Lateral Jet Controlled Missiles," *Journal of Spacecraft and Rockets*; Vol. 34, No. 5, September-October 1997, pp. 584-592.

Srivastava B., "Lateral Jet Control of a Supersonic Missile: Computational and Experimental Comparisons," *Journal of Spacecraft and Rockets*, Vol. 35, No. 2, March-April 1998, pp. 140-146.

Srivastava B., "Axisymmetric Divert Jet Performance of a Supersonic Missile: Computational and Experimental Comparisons," *Journal of Spacecraft and Rockets*; Vol. 36, No. 5, September-October 1999, pp. 621-632.

Thoenes, J., "Semi-Empirical Prediction Of Lateral Control Jet Flowfield Features In Hypersonic Flow," *37th AIAA Aerospace Sciences Meeting and Exhibit*, AIAA-99-0810, Jan 1999, Reno, NV.

VanLerberghe W.M. Santiago J.G., Dutton J.C. and Lucht R.P., "Mixing Of A Sonic Transverse Jet Injected Into A Supersonic Flow," *AIAA Journal*, Vol. 38, No 3, march 2000, pp. 470-479.

APPENDIX A FREESTREAM UNIFORMITY

The five-hole probe was used to measure the freestream Mach number contour (Fig. 75). The average Mach number was 2.97±2.0%. The freestream turbulence level was measured as 3 – 4% using the PIV technique. The freestream was seeded through a hole in the settling chamber. The seeder pressure was about 20 – 30% higher than the settling chamber pressure. Hence, the accuracy of this measurement is suspect.

APPENDIX B UNCERTAINTY ANALYSIS

B.1 Five-Hole Probe

Pressure transducer uncertainties include manufacturer uncertainty (linearity & hysteresis, and repeatability, calibration uncertainty, and resolution uncertainty of the data acquisition card. The manufacturer uncertainties, as tabulated in Table 15, are converted into pressure values. Calibration uncertainties were computed from the differences between the actual pressure reading and the estimated pressure values using the calibration equations. The resolution uncertainty of the acquisition card of 0.0024 volts was converted into the corresponding pressure value using the transducer calibration equations. The transducer calibration equations are described below.

$$p_{t2}\,(psiA) = 25.029 * Volts - 6.2268$$

$$p_{c1}\,(psiA) = 3.7421 * Volts - 0.5223$$

$$p_{c2}\,(psiA) = 3.7724 * Volts - 0.9121$$

$$p_{c3}\,(psiA) = 3.7663 * Volts - 0.6494$$

$$p_{c4}\,(psiA) = 3.7681 * Volts - 0.4492$$

$$p_{t\infty}\,(psiA) = 19.19 * Volts - 0.0866 + p_{atm}$$

$$p_{\infty}\,(psiA) = 2.9551 * Volts + 0.3303$$

Detailed transducer uncertainties are listed Table 15. The Thermocouple uncertainties are listed in Table 16.

The total uncertainty in Mach number measurement includes the uncertainties due to the pressure transducer, 5-hole probe Mach number calinration, and probe inclination. The pressure transducer uncertainties are described above. The Mach number uncertainty of ± 0.03 is documented for the probe misalignment of ± 6 degree [Volluz (1961)]. The overall L2-norm of the uncertainty was computed following Holman (1978); that is

$$1/M_1 = M' = f(P_c / P_{t2})$$

$$\omega_{M'} = \left[\left(\frac{\partial M'}{\partial P_c} \right)^2 \left(\omega_{P_c} \right)^2 + \left(\frac{\partial M'}{\partial P_{t2}} \right)^2 \left(\omega_{P_{t2}} \right)^2 \right]^{1/2}$$

$$\omega_{M_1} = \left[\left(\frac{\partial M_1}{\partial M'} \right)^2 \left(\omega_{M'} \right)^2 \right]^{1/2}$$

$$M_{rcal} = (-0.0606 M_1 + 1.2299) M_1$$

$$\omega_{rcal} = \left[\left(\frac{\partial M_{rcal}}{\partial M_1} \right)^2 \left(\omega_{M_1} \right)^2 \right]^{1/2}$$

$$\omega_{M_{total}} = (\omega_{rcal}^{\ 2} + \omega_{angle}^{\ 2} + \omega_{cal}^{\ 2})^{1/2}$$

where, M_1 = Mach number from the Taylor-Mccoll conical from theory approximation; $\omega_{M'}$ = Uncertainty for $M'(= 1/M_1)$; ω_{M_1} = Uncertainty for M_1; M_{rcal} = Mach number based on experimental re-calibration; ω_{rcal} = Uncertainty for M_{rcal}; ω_{angle} = Uncertainty of Mach number for probe inclination angle; ω_{cal} = Uncertainty for the curve-fit solution of the conical flow theory, and $\omega_{M_{total}}$ = Total uncertainty of Mach number from the 5. The inviscid solution was curve fit by Eqn (4.1), the hence the derivatives were given by

$$\frac{\partial M'}{\partial p_c} = \left(\frac{1}{P_{t2}}\right)\left[24.873 - 316.178\left(\frac{P_c}{P_{t2}}\right) + 1698.852\left(\frac{P_c}{P_{t2}}\right)^2 - 4499.08\left(\frac{P_c}{P_{t2}}\right)^3 + 5827.55\left(\frac{P_c}{P_{t2}}\right)^4 - 2950.776\left(\frac{P_c}{P_{t2}}\right)^5\right]$$

$$\frac{\partial M'}{\partial p_{t2}} = \left(\frac{P_c}{(P_{t2})^2}\right)\left[-24.873 + 316.178\left(\frac{P_c}{P_{t2}}\right) - 1698.852\left(\frac{P_c}{P_{t2}}\right)^2 + 4499.08\left(\frac{P_c}{P_{t2}}\right)^3 - 5827.55\left(\frac{P_c}{P_{t2}}\right)^4 + 2950.776\left(\frac{P_c}{P_{t2}}\right)^5\right]$$

The Pitot pressure uncertainty includes both probe angle effects and transducer calibration. The static and total pressure uncertainties were computed following the above analysis using the compressible flow relation. The resulting uncertainties are listed in Table 17.

B.2 LaVision PIV

The PIV uncertainty stemmed from the assumption that the particle position uncertainty was 0.3 pixels [Gogineni et al (1998)]. With this, the uncertainties for the measured quantities were estimated as listed in Table 17.

B.3 Pressure Sensitive Paint

The pressure sensitive paint uncertainty estimate included system (calibration and camera) as provided by the manufacturer (2.0% of the measured value), and surface temperature. The surface temperature was known to approximately ±5K, and the temperature sensitivity was 0.6%/K. Hence, the overall L2 norm was computed as 3.6% of the measured value.

B.4 Separation Distance

The separation distance was measured with a dial caliper that has a resolution of 25.4 μm. This resolution was taken as the measurement uncertainty.

TABLES

Table 1 Range of Jet Parameters

Jet Mach, M_j	MPR	P_j / P_∞	T_j / T_∞	γ_j
1.0 – 3.0	0.005 – 0.09	0.6 – 18.8	1.0 – 13.6	1.4, 1.67

Table 2 Freestream Conditions

Mach	Velocity, m/s	Temperature, K	Pressure, KPa	Re/m	$\sqrt{\overline{u'^2}}$
3.0	616	105	17.3	48.5	3.0%

Table 3 Tunnel Operating Conditions

$P_{t\infty}$, Mpa	$T_{t\infty}$, K
0.6067 ± 0.0207	285 ± 2.2

Table 4 Diffuser Dimensions

H1	Mach	A	H1-A	ϕ	L1	L1/W	φ	L2	H2	L2/W	α	β	H
3	4.0	2.00	1	9.50	6	3.006	8.98	19	5	9.52	14.07	4.41	1.48
	3.0	2.14	0.86	8.15	6	2.802	8.56	19	5	8.87	12.72	3.98	1.34
	2.0	2.45	0.55	5.26	6	2.451	7.66	19	5	7.76	9.83	3.08	1.03
	1.5	2.73	0.27	2.61	6	2.2	6.82	19	5	6.97	7.18	2.25	0.75

(see figure 3.5 for clarity)

Table 5 Injector Dimensions

Model	Exit Mach	Throat diameter, D_j, mm (in)	Exit diameter, D_e, mm (in)	D_e/D_j
M3A-HP	3.0	1.191 (3/64)	2.453	2.06
M3A-LP	3.0	3.969 (5/32)	8.176	2.06
M3H	3.0	3.969 (5/32)	6.863	1.73
M1A	1.0	4.763 (3/16)	4.763	1
M1A-L	1.0	9.525 (3/8)	9.525	1

Table 6 Injector Operating Conditions

Model	M_j	Injectant	P_{tj} MPa	P_j/P_∞	P_j/P_{eb}	γ_j	$\gamma_j M_j^2 / \gamma_\infty M_\infty^2$	A_b/A_j	MPR
M3A-HP	3.0	Air	5.96	9.38	3.07	1.4	1.00	210.2	0.05
			12.9	18.82	6.15				0.09
M3A-LP	3.0	Air	0.377	0.60	0.19	1.4	1.00	18.9	0.03
			0.694	1.09	0.36				0.06
M3H	3.0	He	0.365	0.66	0.22	1.67	1.19	26.9	0.03
			0.670	1.21	0.40				0.05
M1A	1.0	Air	0.088	2.68	0.88	1.4	0.11	55.8	0.005
			0.101	3.10	1.01				0.006
			0.263	8.04	2.06				0.015
M1H	1.0	He	0.224	6.31	2.06	1.67	0.13	55.8	0.015
M1A-L	1.0	Air	0.088	2.68	0.88	1.4	0.11	13.9	0.021
			0.101	3.10	1.01				0.024

$MPR = \gamma_j M_j^2 P_j A_j / \gamma_\infty M_\infty^2 P_\infty A_b$; $P_{eb} = 0.8P_2$; A = Air; H = Helium

Table 7 Range of Temperature Ratios

Model	MPR	T_{tj}, K	T_j/T_∞
M3A-HP/LP	0.03-0.06	294.0	1.0
M1A	0.005-0.015	294.0	2.3
M1A-L	0.021, 0.024	294.0	2.3
M1A	0.006	920.0	7.3
M3H	0.006	1250.0[b]	11.9
M1H	0.015	1900.0[b]	13.6

[a]Pebble bed heated air injection, [b]Simulated temperature based on light gas (helium) injection

Table 8 Flowmaster3 Camera Specs

Model	Flowmaster3S
Sensor	SONY ICX 085
Pixel (h × v)	1280 × 1024 (square format)
Pixel Size (h × v)	6.7 μm × 6.7 μm
Active Area (h × v)	8.6 mm × 6.9 mm
Fill Factor	60% (with microlens)
Dynamic Range	12 bit
Single Frames per Second	8
Min Interframing Time	300 ns

Table 9 LaVision PIV Laser Specs

Wavelength	532 nm
Gemini PIV15	120mJ
Energy Stability	±3.5%
Pulse width	3–5ns
Beam divergence	<1 mrad
Beam pointing	<200 μrad
Jitter	±0.5 ns

Table 10 Transducer Specifications

PX139 series	**PX139 series**
Excitation Voltage	5 Vdc
Output:	0.25 to 4.25 volts
Linearity and Hysteresis:	±0.1% FS
Repeatability:	±0.3% FS
Proof pressure:	> 3 × FS Pressure
Burst Pressure:	> 5 × FS Pressure
PX202-100GV, and PX302-015AV	**PX202-100GV, and PX302-015AV**
Excitation Voltage	10 Vdc
Output:	100mV ± 1mV
Linearity, Hysteresis, and Repeatability	± 0.25% FS
Response Tine	1msec
Vibration:	PX202 – 35g peak @ 5 – 2000Hz PX302 – 15g peak @ 10 – 2000Hz
Proof pressure:	PX202 - 150% PX302 – 200%
Burst Pressure:	400%

Table 11 Five-Hole Probe Calibration

Mach	p_c/p_{t2} [1]	*%error* [2]
1.20	0.6284	0.85
1.30	0.5491	0.73
1.40	0.498	0.37
1.50	0.4568	0.47
1.75	0.3794	0.62
2.00	0.3256	0.20
2.25	0.2868	0.07
2.50	0.258	0.02
2.75	0.2359	0.25
3.00	0.2187	0.50
3.25	0.2051	0.68
3.50	0.1941	0.71
4.00	0.1777	0.42
4.50	0.1661	0.36
5.00	0.1580	0.79
6.00	0.1470	1.13
7.00	0.1402	1.21
8.00	0.1357	0.60
9.00	0.1325	0.74
10.00	0.1300	0.91

[1]Theory: Exact for Mach≤5 and 10.0, Hypersonic Similarity for Mach=6-9
(Difference between exact and Hypersonic Similarity<0.5% at Mach=5.0 and 10.0).
[2] based on the curve-fit solution.

Table 12 Five-Hole Probe Calibration Data

p_c/p_{t2}	$Mach^1$	$Mach^2$	$Mach^3$
0.142	7.04	5.52	5.55
0.155	6.45	4.83	4.79
0.229	4.37	3.00	3.01
0.452	2.21	1.72	1.72

[1]conical flow theory, [2]normal shock relationship,[3]recalibrated curve fit

Table 13 Parameters used to process PIV images and vectors

Image processing:
Mode: Cross-correlation (1 camera)
Int. window size and shift:
Adaptive multi-pass (4 passes) with decreasingly smaller sizes were used Initial int. window size: 64 × 64 Final int. window size: 32 × 32 [iteration: 3] Overlap: 50% Initial shift: 0
Correlation Function [Initial and Final passes]:
Standard 11*12 (via FFT, no zero padding) Deformed int. window: off
Multi-pass:
Relative vector range restriction: reference ± cell-size / 8 AND absolute vector range restriction: reference ± 4 pixels Overlap for initial passes: 50%
VECTOR POST PROCESSING
Median Filter: Strongly remove and iteratively replace
Remove if > 1.5 * RMS of neighbors Remove if < 3 neighbors Insert if < 2 * RMS of neighbors
Remove groups with less than: 10 vectors
Smooth: 3 × 3
Allowed vector range:
Vx: -400 to 700 m/s Vy: -400 to 700 m/s for Mach 3 injection case Vy: -400 to 400 m/s for sonic injection case

Table 14 Boundary Layer Separation Distance

Model	T_j/T_∞	De, mm	MPR	Pj/Pinf	Separation Distance (Δ/De)
M3A-HP	1.0	2.45	0.09	18.82	2.81
			0.05	9.38	2.08
M3A-LP	1.0	8.18	0.06	1.09	1.88
			0.03	0.59	1.61
M3H	11.9	6.86	0.05	1.21	2.22
			0.03	0.66	1.75
M1A	2.3	4.76	0.02	3.10	1.76
			0.02	2.68	1.75
M1A	7.3		0.02	3.10	1.83
M1A	2.3	4.76	0.015	8.13	2.03
M1H	13.6	4.76	0.015	6.41	2.16

Table 15 Pressure Transducers and Uncertainties

Transducer Model	Measured pressure	Manufacturer uncertainty ± Pa (psia)	Calibration uncertainty ± Pa (psia)	Resolution uncertainty of acquisition card ± Pa (psia)	Total Uncertainty ± Pa (psia)
Omega PX139-100A4V	p_{t2}	2180 (0.316)	446.8 (0.0648)	413.7 (0.06)	2260 (0.328)
Omega PX139-015A4V	p_{c1}	326.8 (0.0474)	92.4 (0.0134)	62.1 (0.009)	344.7 (0.05)
Omega PX139-015A4V	p_{c2}	326.8 (0.0474)	139.3 (0.0202)	62.1 (0.009)	358.5 (0.052)
Omega PX139-015A4V	p_{c3}	326.8 (0.0474)	122.7 (0.0178)	62.1 (0.009)	351.6 (0.051)
Omega PX139-015A4V	p_{c4}	326.8 (0.0474)	147.6 (0.0214)	62.1 (0.009)	365.4 (0.053)
Omega PX202-100GV	$p_{t\infty}$	1720 (0.25)	176.3 (0.02557)	317.16 (0.046)	1758 (0.255)
Omega PX302-015AV	p_{∞}	258.6 (0.0375)	93.08 (0.0135)	46.88 (0.0068)	275.8 (0.04)

Table 16 High Temperature Thermocouple and Uncertainty

Thermocouple Model	Measurement	Uncertainty ± ^{0}C (^{0}F)
Omega XTA-W5R26-U-125-30-H-HX-6	T_{tj}	0.4 ^{0}C (0.7 ^{0}F)

Table 17 Measurement Uncertainty Summary

Measurement	Uncertainty
M (Five-Hole Probe)	0.13
$P_{t2}/P_{t\infty}$	0.02
$P_1/P_{t\infty}$	0.15
$P_{t1}/P_{t\infty}$	0.10
$\overline{u_i}/u_\infty$ (LaVision PIV)	0.02
$\sqrt{\overline{u_i'}}/u_\infty$	0.02
$\overline{u_i'u_j'}/u_\infty^2$	0.001
$\partial\overline{u_i}/\partial x_j$	1.3
p (PSP)	3.6%
Δ (μm)	25.4

FIGURES

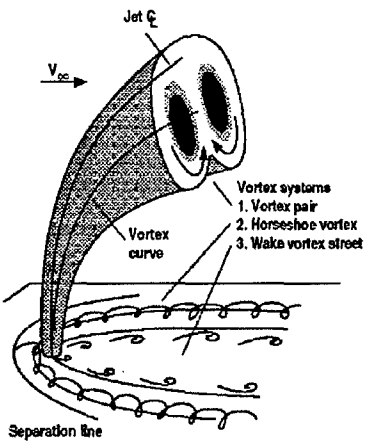

Figure 1 Low-Speed Jet Interaction Flowfield [Margason (1993)]

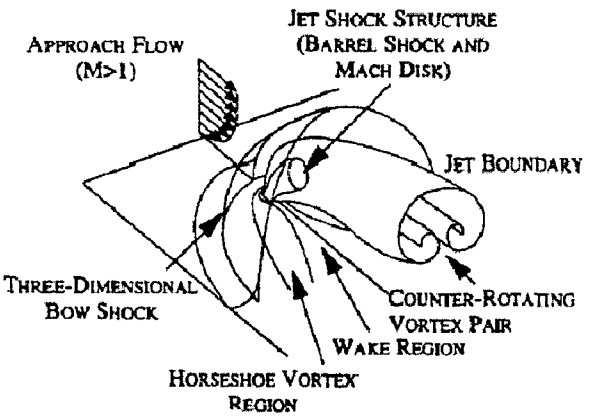

(a) Issuing from a flat surface [Gruber et al (1997)]

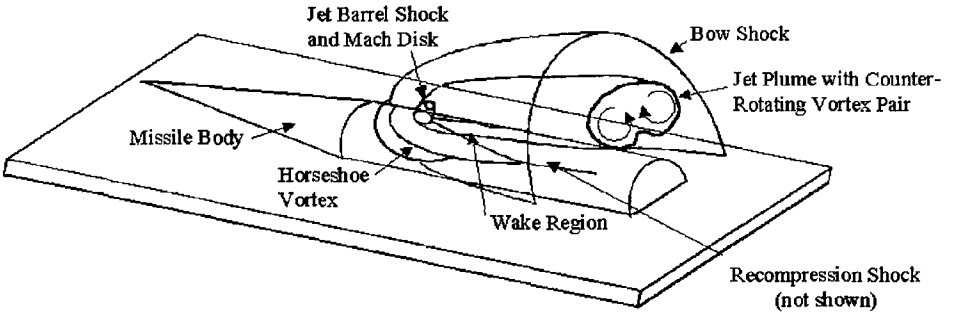

(b) Issuing from the present blended body of revolution

Figure 2 Supersonic Jet Interaction Flowfield (Flat Plate & Blended Missile Body)

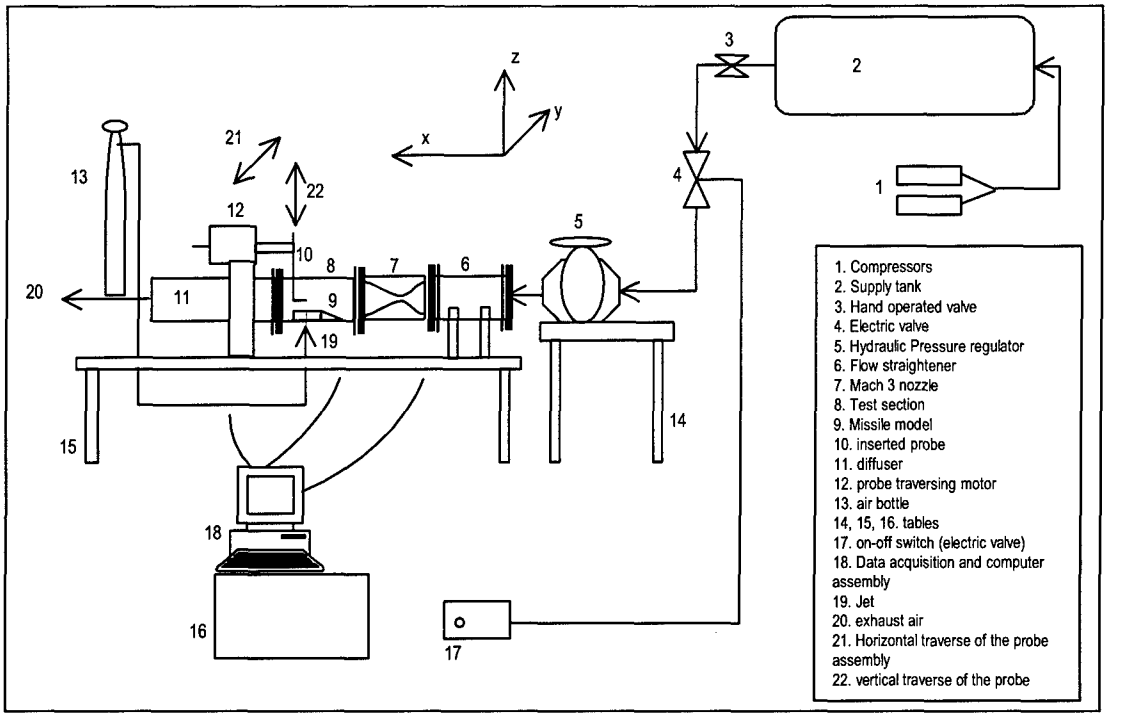

(a) Schematic

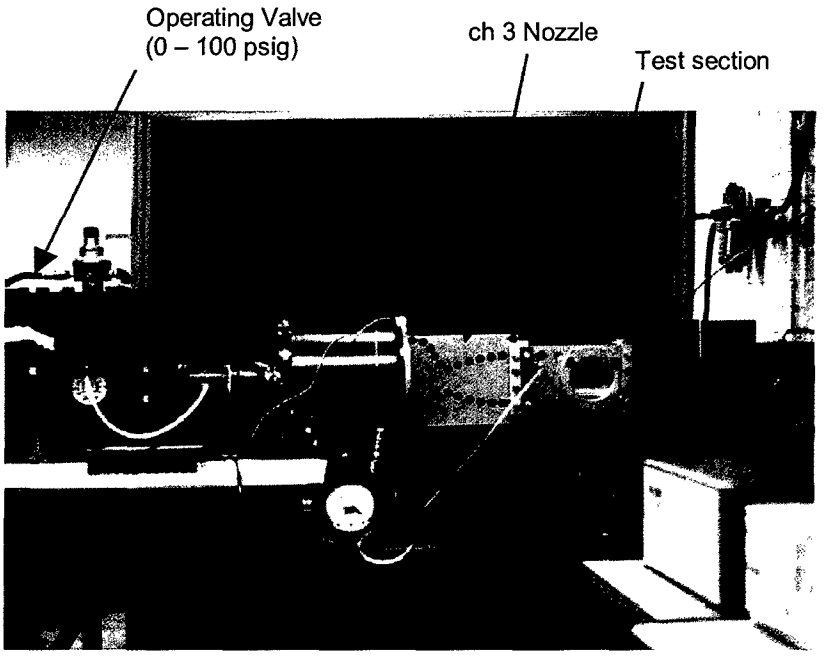

(b) Photograph

Figure 3 Mach 3.0 Wind Tunnel (schematic and photograph)

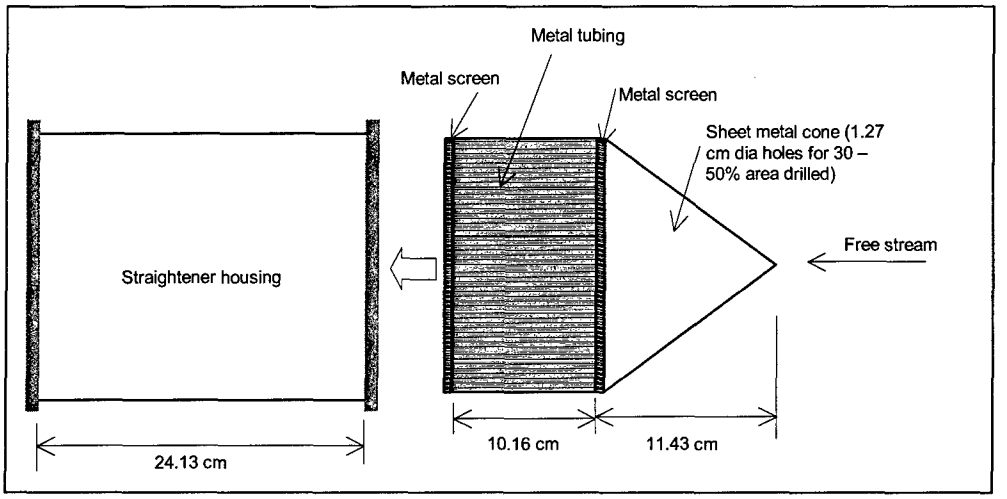

Figure 4 Flow Straightener (schematic)

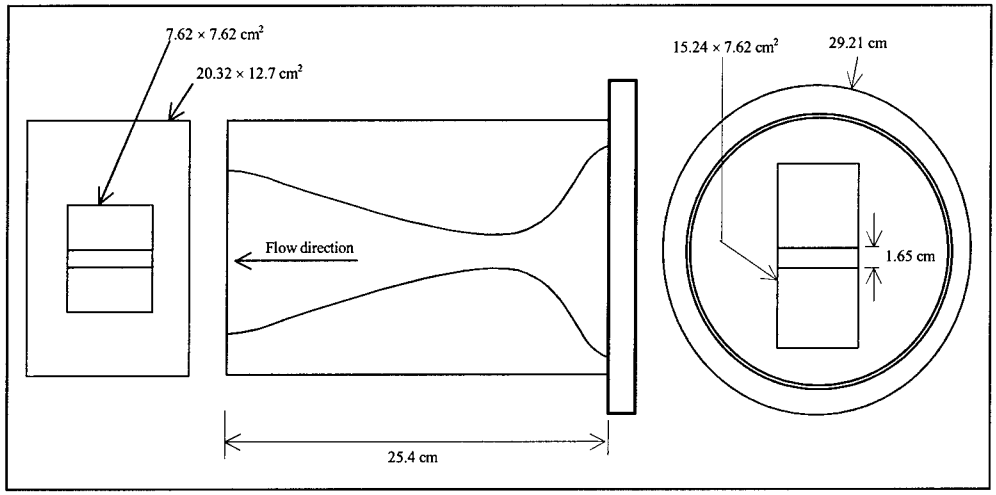

Figure 5 Sketch of the Mach 3 Nozzle
(Not to Scale)

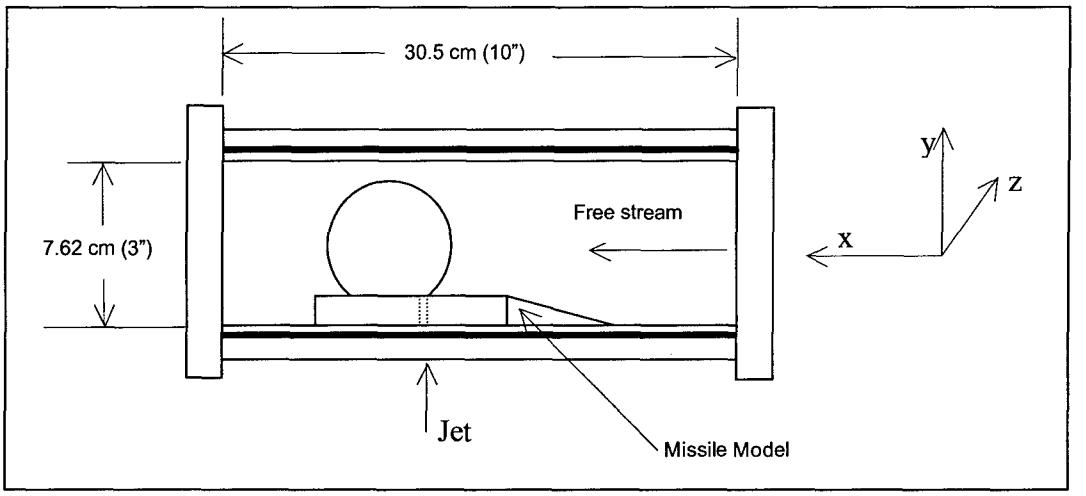

(a) Schematic

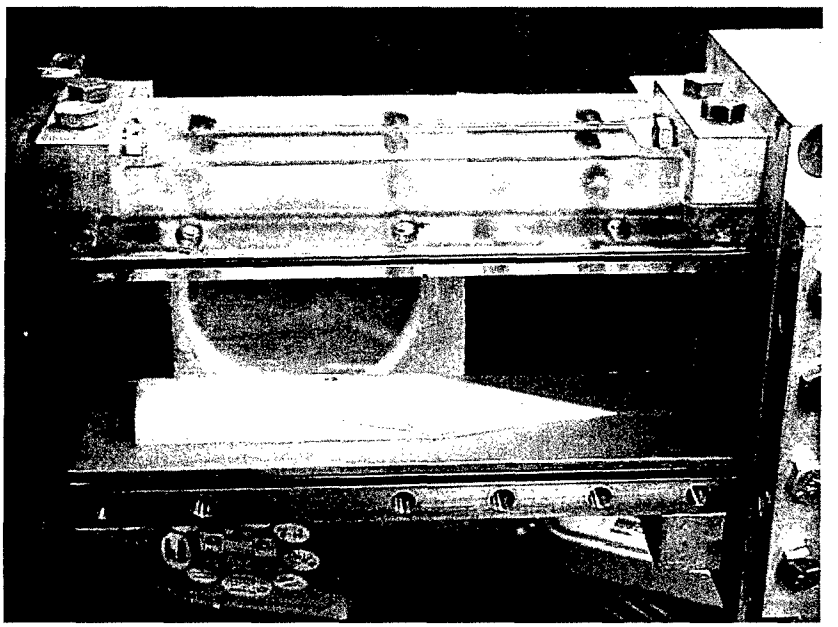

(b) Photograph

Figure 6 Test section with a model (schematic and photograph)

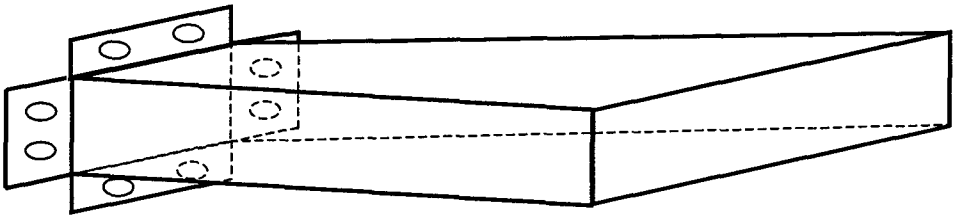

(a) Sketch

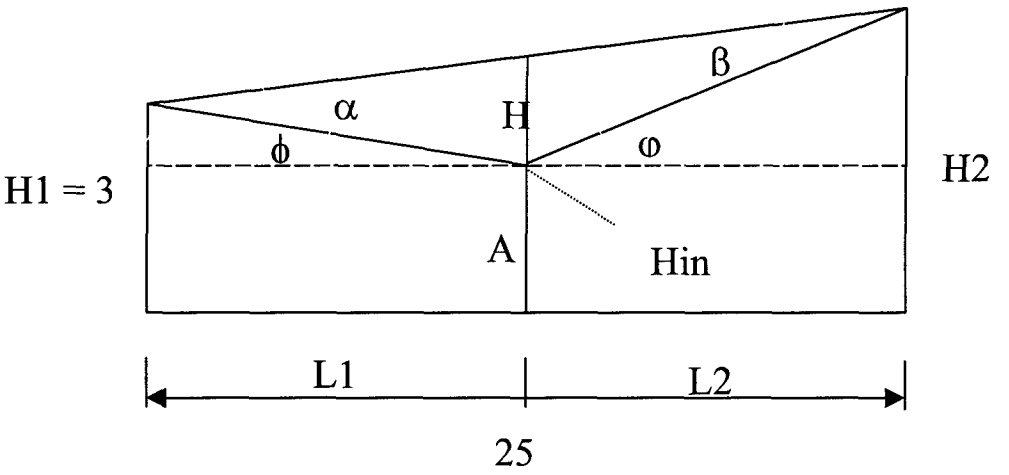

(b) Dimensions (see Table 3.3)

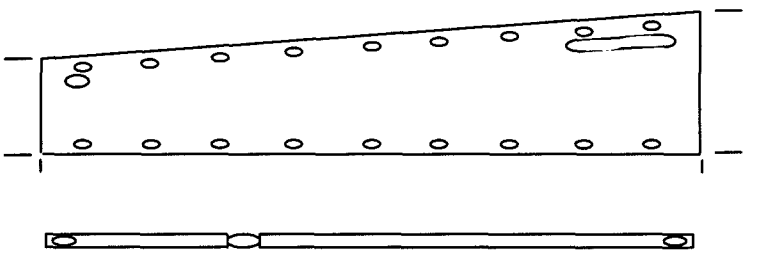

(c)

(c) Side-View
Figure 7 Diffuser

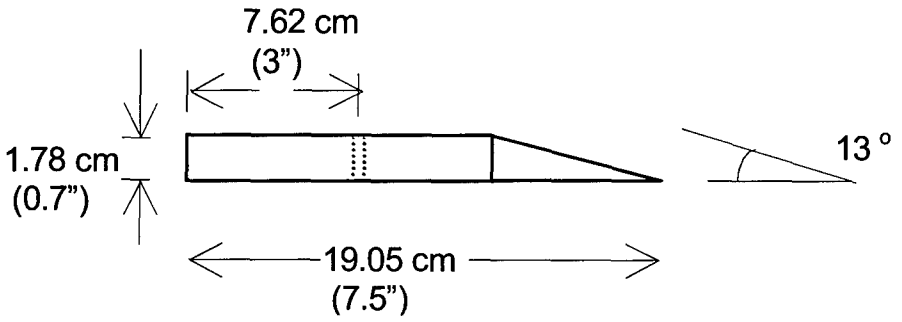

Figure 8 Missile Model Schematic

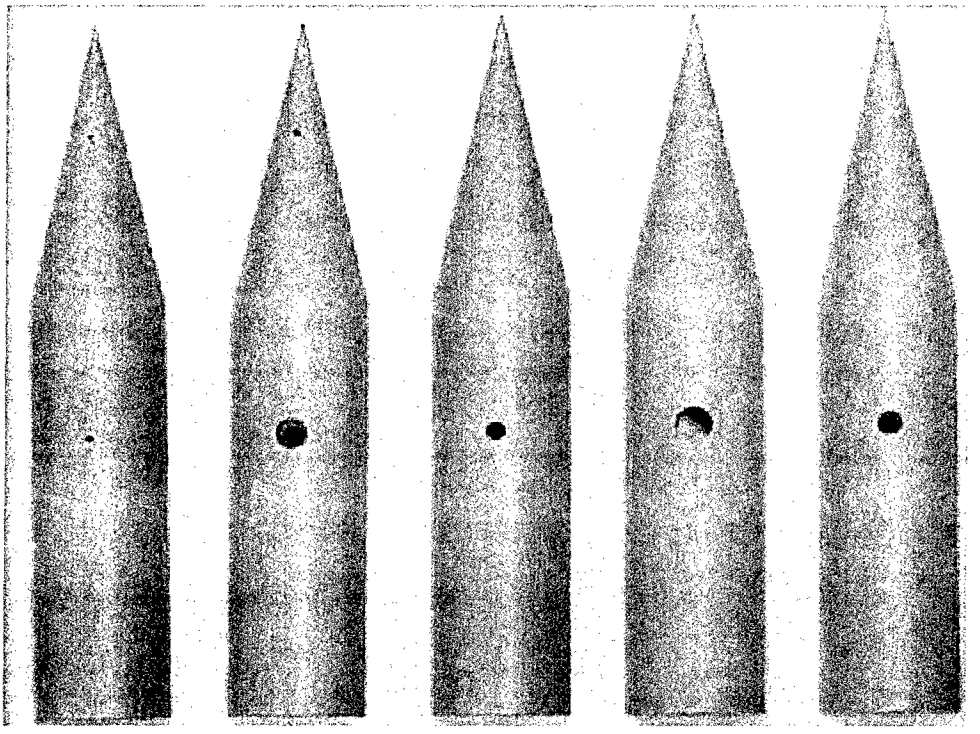

Figure 9 Model Photographs

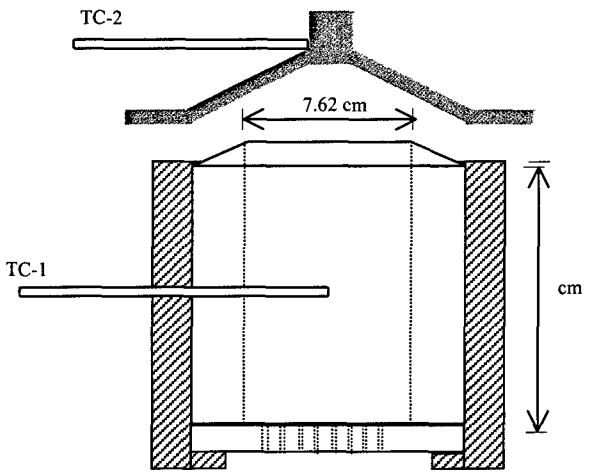

Figure 10 Pebble bed heater (schematic)

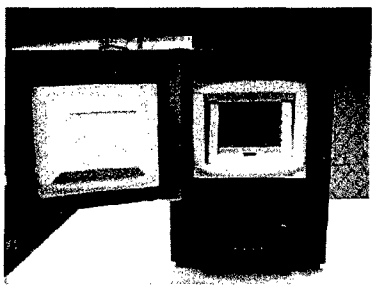

(a) Electric Furnace

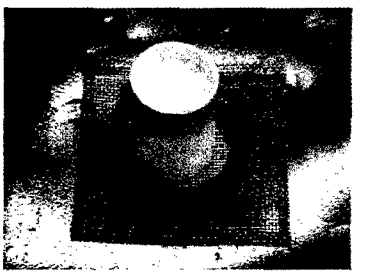

(b) Hot Ceramic Pebbles

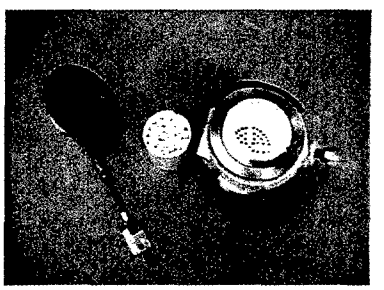

(c) Pebble Bed Housing

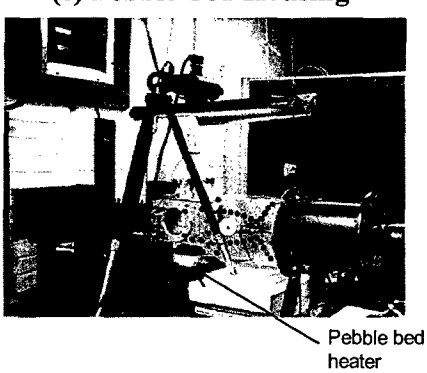

(d) Pebble Bed and Tunnel
Figure 11 Pebble Bed Heater

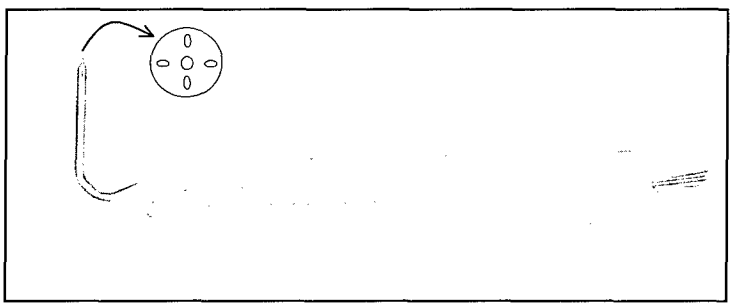

Figure 12 Photograph of 5-hole Pitot Probe

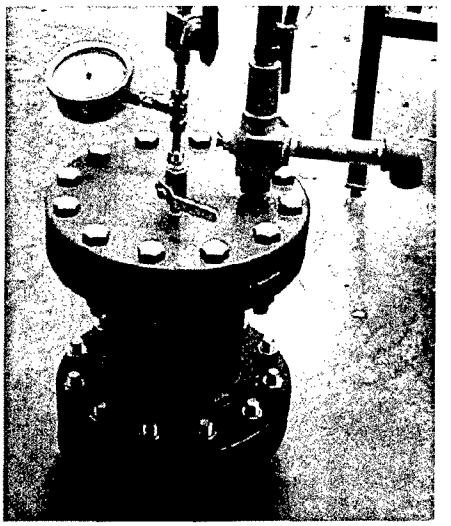

(a) PIV Seeder Tank

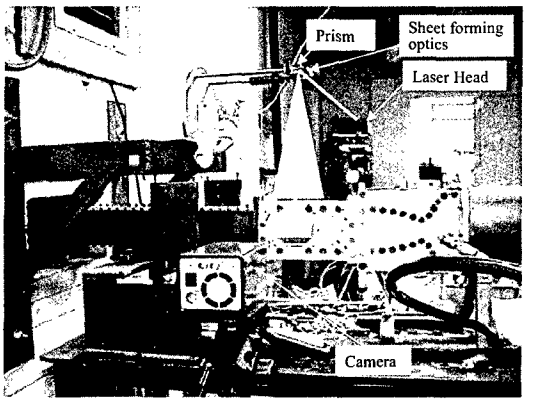

(b) LaVision PIV system
Figure 13 LaVision PIV Apparatus

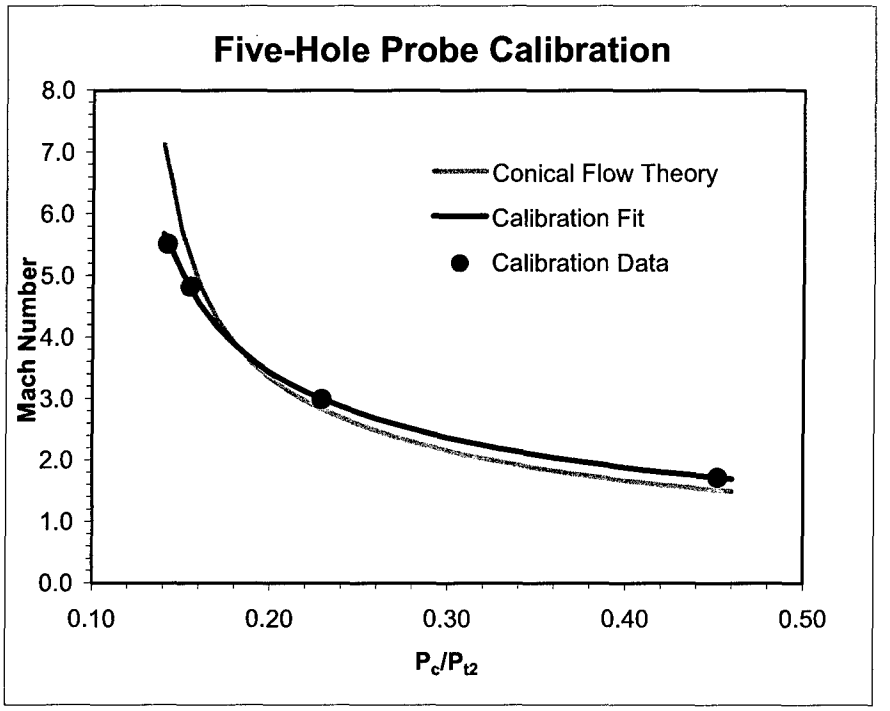

Figure 14 Five-Hole Probe Calibration

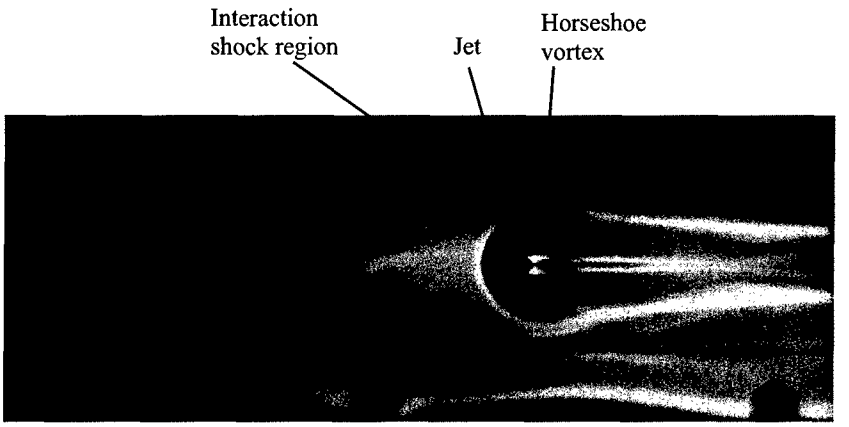

Figure 15 General Flow Features

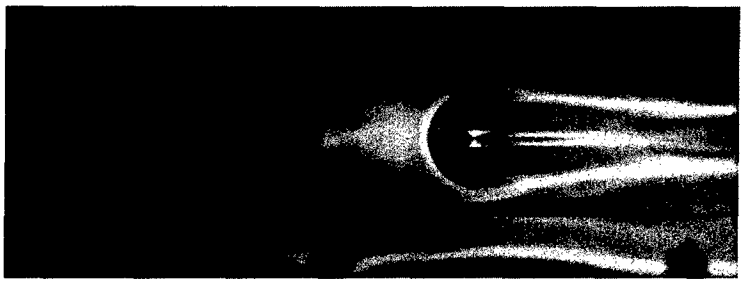

(a) Model M1A, MPR 0.006

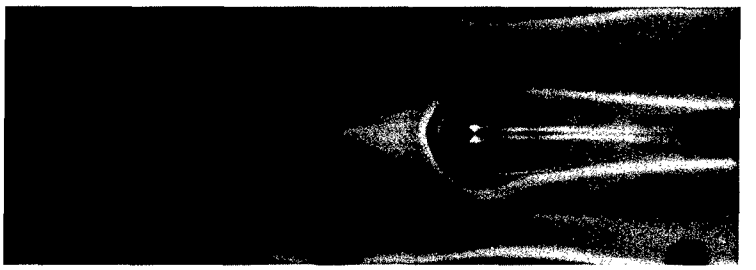

(b) Model M1A, MPR 0.005

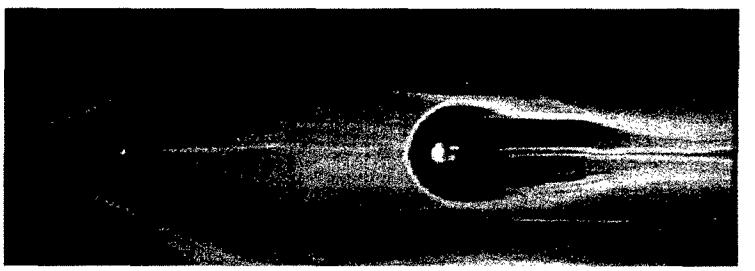

(c) Model M1A, MPR 0.006, at 922 K

Figure 16 Surface Oil Flow Visualizations for Model M1A

(a) Model M3A-LP, MPR 0.03

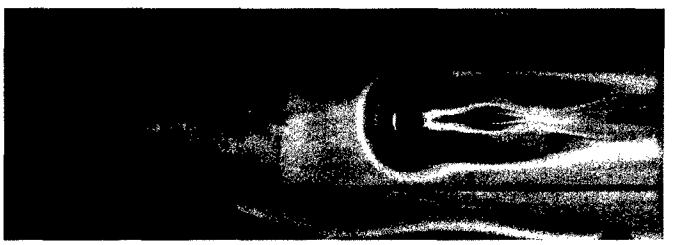

(b) Model M3A-LP, MPR 0.06

Figure 17 Surface Oil Flow Visualizations for Model M3A-LP

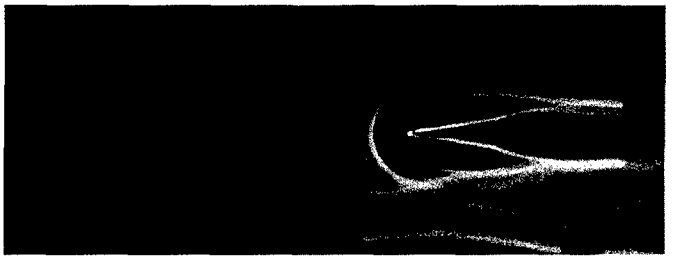

(a) Model M3A-HP, MPR 0.05

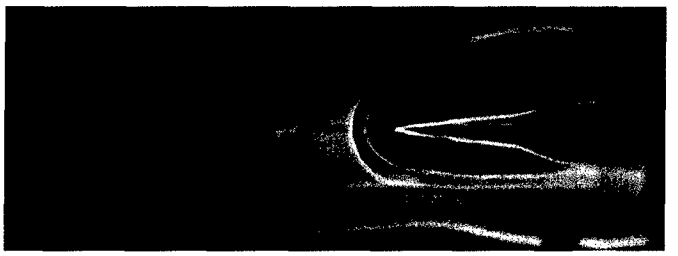

(a) Model M3A-HP, MPR 0.09

Figure 18 Surface Oil Flow Visualizations for Model M3A-HP

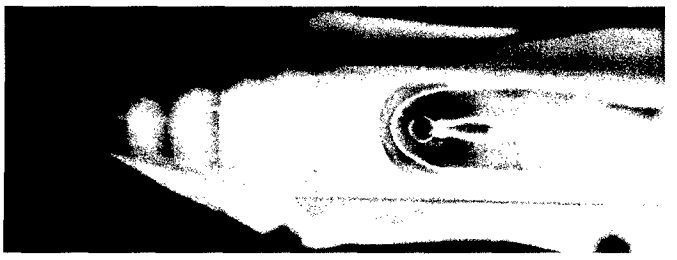

(a) Model M3H, MPR 0.03

(b) Model M3H, MPR 0.06

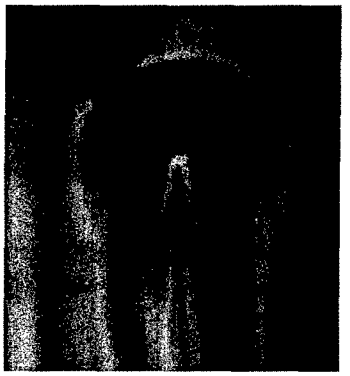

(i) M1A, air injection

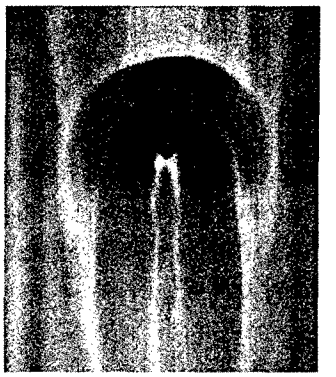

(ii) M1H, Helium injection

(c) MPR 0.015 (air and helium injection)
Figure 19 Surface Oil Flow Visualizations for Model M3H

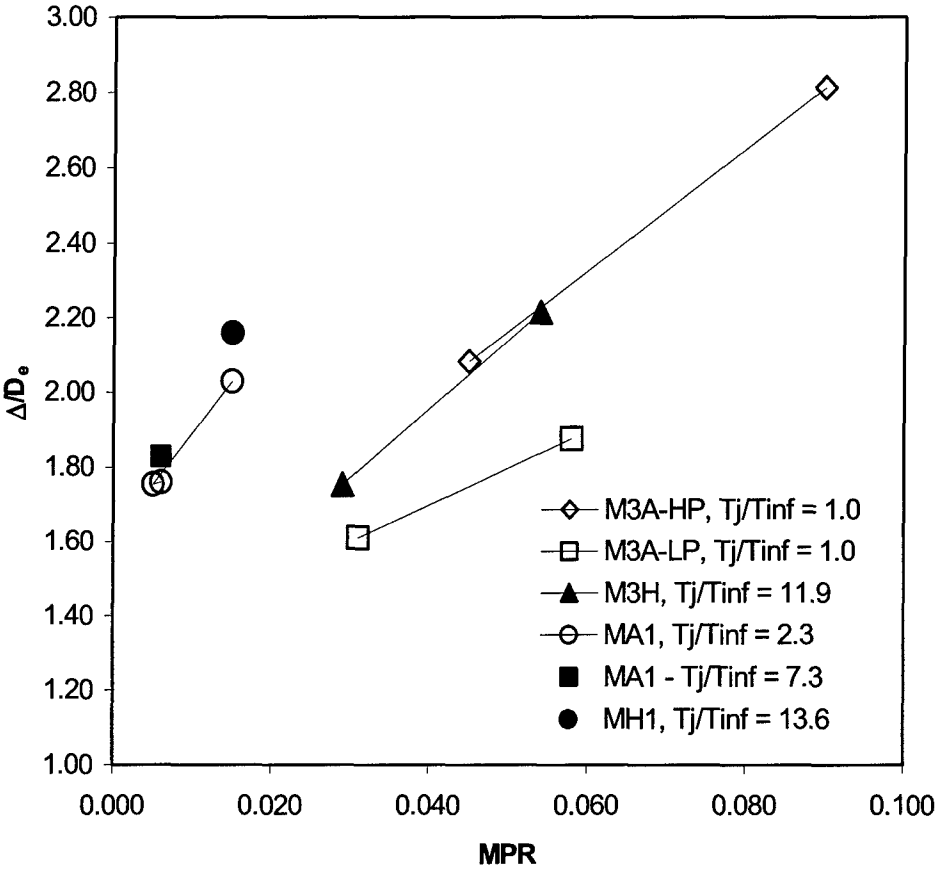

Figure 20 Boundary layer separation distance vs. MPR

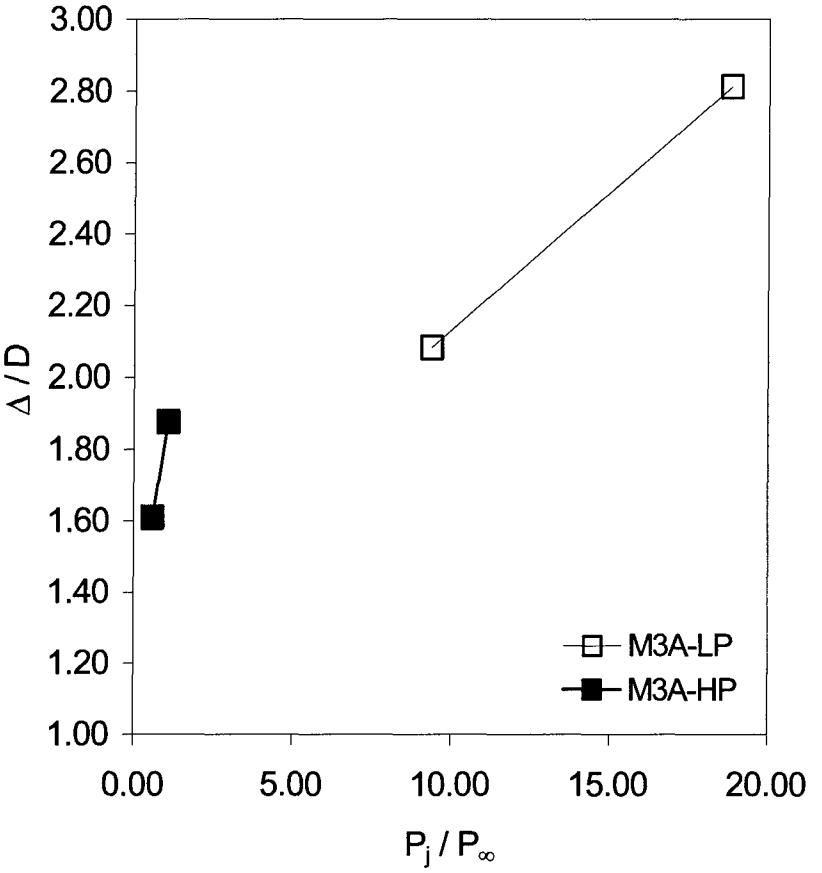

Figure 21 Boundary layer separation distance versus jet Pressure (Model M3A)

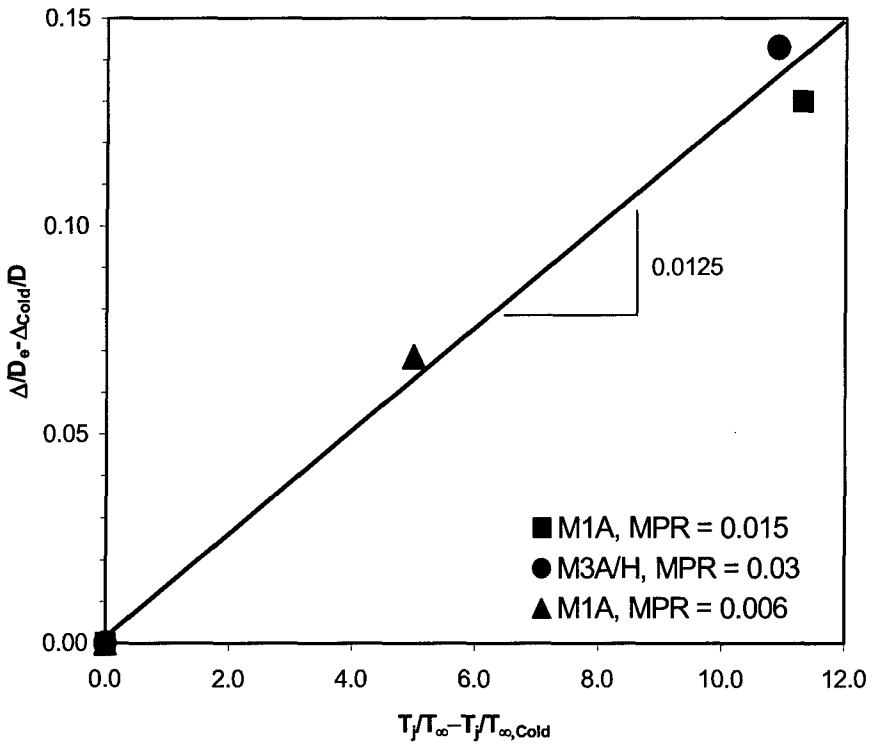

Figure 22 Change in Boundary layer separation distance vs. Change in Temperature

Figure 23 Mie-scattering image, Model M1A, MPR 0.006

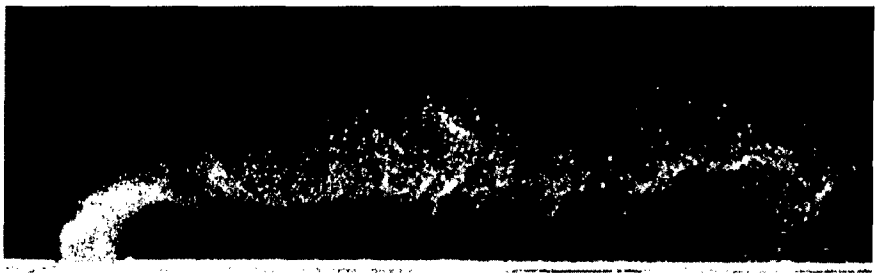

(a) Model M1A at z = 0

(b) Model M1A at z = 1/16 inch

(c) M1A at z = 2/16 inch

Figure 24 Instantaneous Mie-scattering images (Model M1A, MPR 0.006)

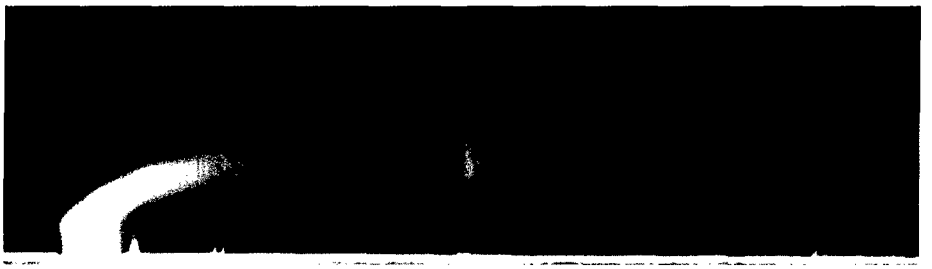

(a) Average PIV image at station z = 0

(b) Average PIV image at station z = 1.59 mm

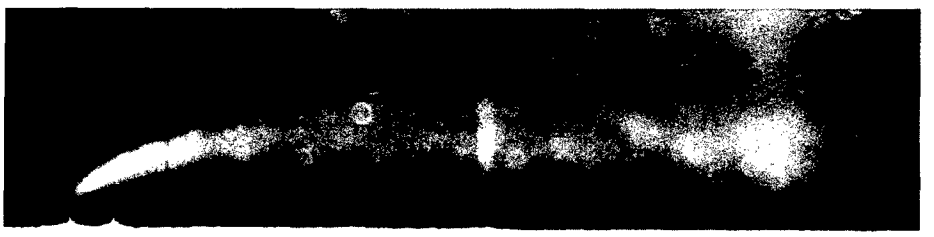

(c) Average PIV image at station z = 3.18 mm

Figure 25 Average Mie-scattering images (Model M1A, MPR 0.006)

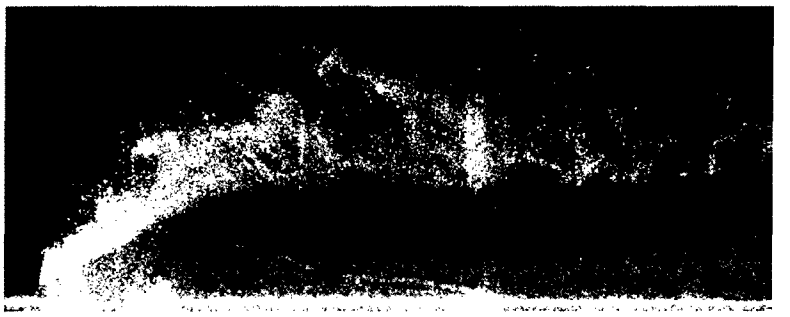

(a) Instantaneous particle image at station z = 0

(b) Instantaneous particle image at station z = 1.59 mm

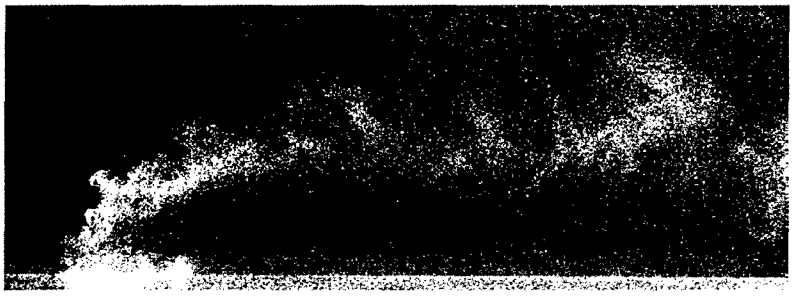

(c) Instantaneous particle image at station z = 3.18 mm

Figure 26 Instantaneous Mie-scattering images (Model M3A-LP, MPR 0.06)

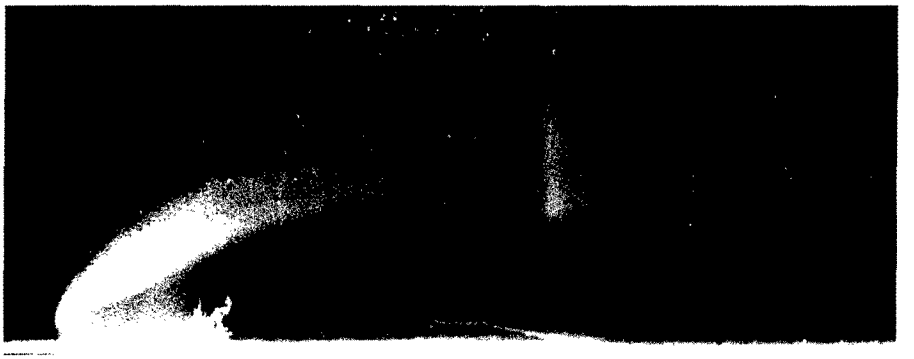

(a) Average PIV image at station z = 0

(b) Average PIV image at station z = 1.59 mm

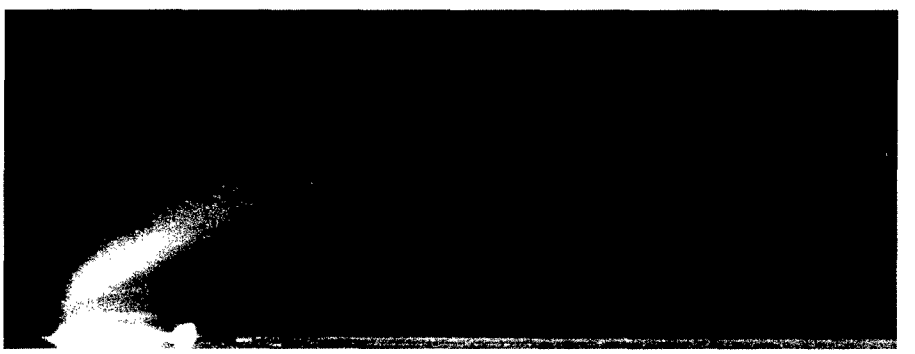

(c) Average PIV image at station z = 3.18 mm

Figure 27 Average Mie-scattering images (Model M3A-LP, MPR 0.06)

(a) Instantaneous Mie-scattering at station z = 0

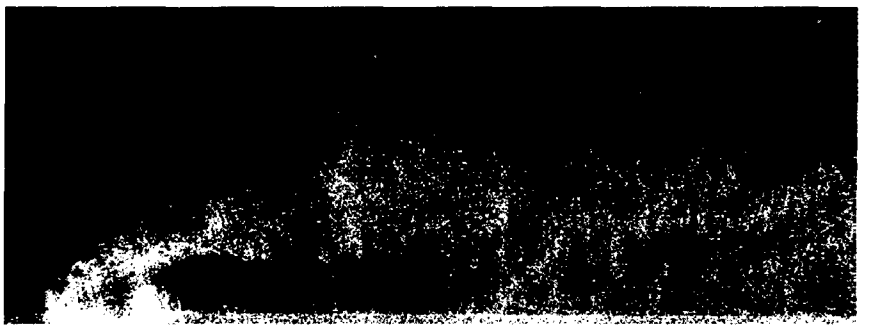

(b) Instantaneous Mie-scattering at station z = 1.59 mm

(c) Instantaneous Mie-scattering at station z = 3.18 mm

Figure 28 Instantaneous Mie-scattering images (Model M3A-LP, MPR 0.03)

(a) Average PIV image at station z = 0

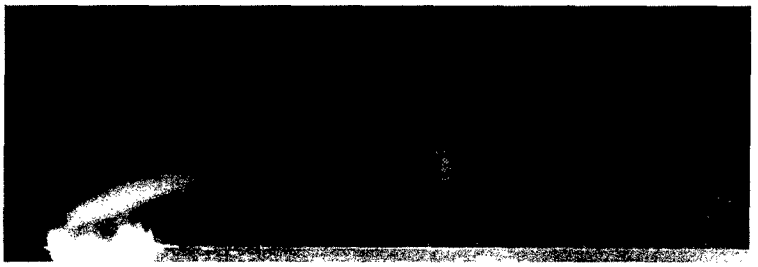

(b) Average PIV image at station z = 1.59 mm

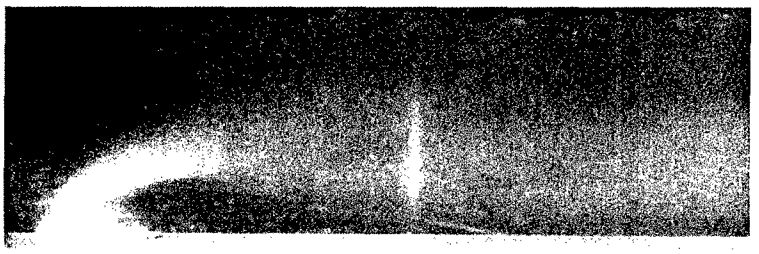

(c) Average PIV image at station z = 3.18 mm

Figure 29 Average Mie-scattering images (Model M3A-LP, MPR 0.03)

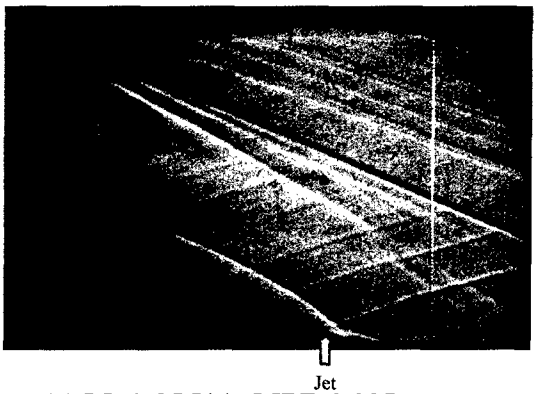

(a) Model M1A, MPR 0.005

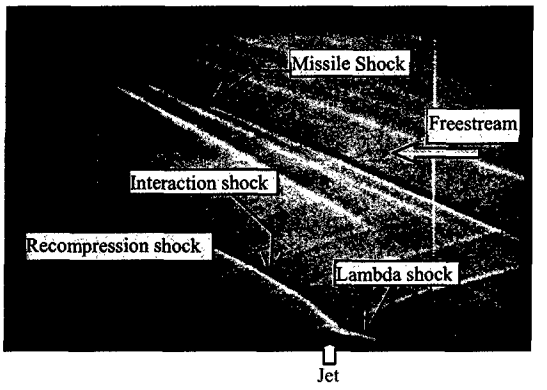

(b) Model M1A, MPR 0.006

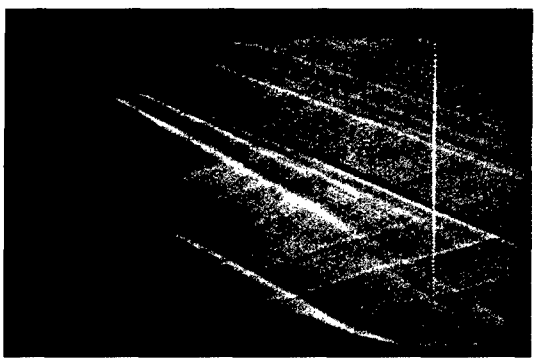

(c) Model M1A-L, MPR 0.003

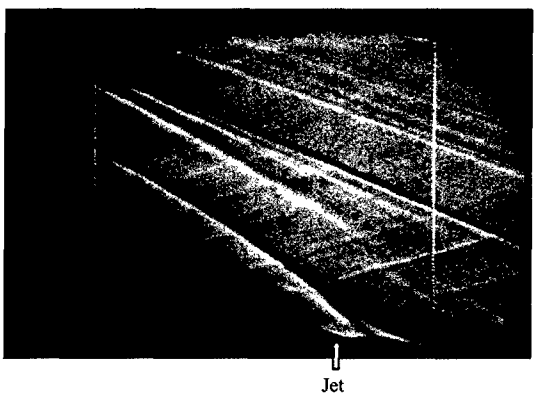

(d) Model M1A-L, MPR 0.006

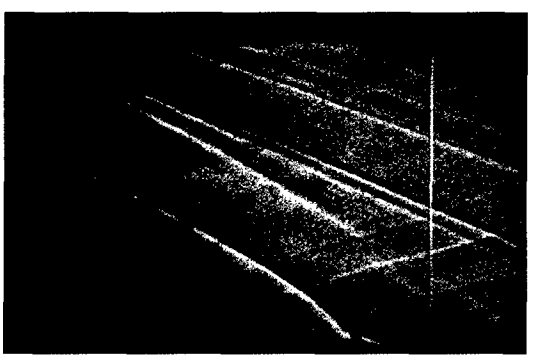

(e) Model M3A-LP, MPR 0.03

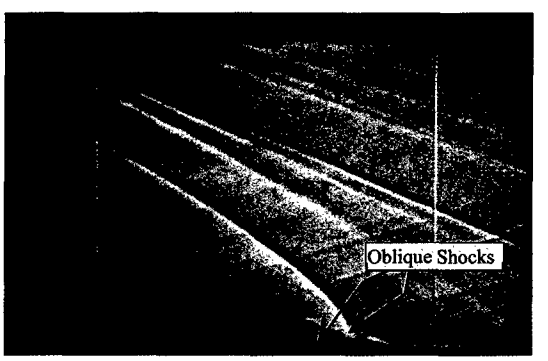

(f) Model M3A-LP, MPR 0.06

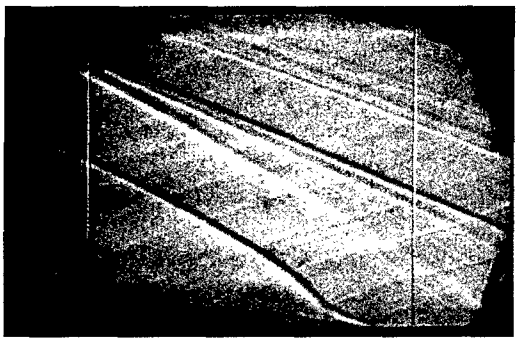

(g) Model M3H, MPR 0.03

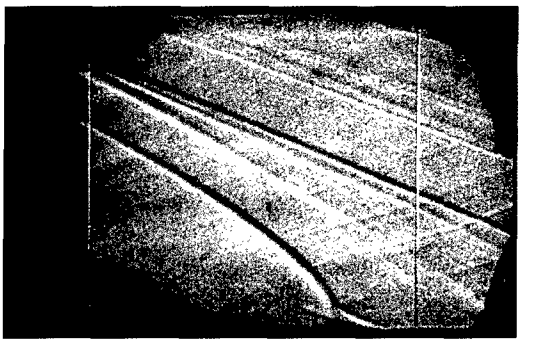

(h) Model M3H, MPR 0.06

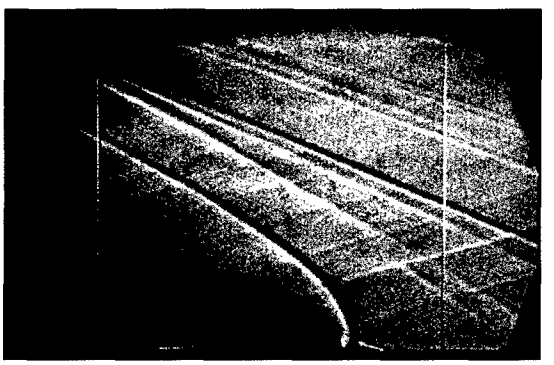

(i) Model M3A-HP, MPR 0.05

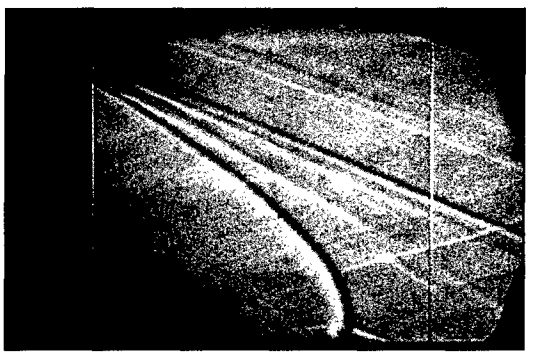

(j) Model M3A-HP, MPR 0.09

Figure 30 Shadowgraph images

(a) Model M1A, MPR 0.005

(b) Model M1A, MPR 0.006

(c) Model M3A-LP, MPR 0.03

(d) Model M3A-LP, MPR 0.06

(e) Model M3A-HP, MPR 0.05

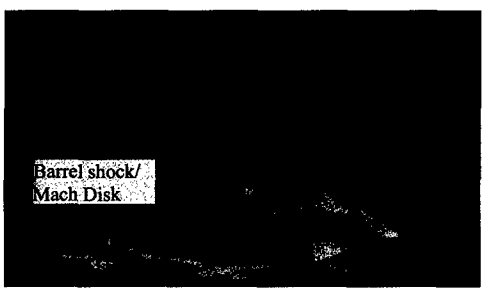

(f) Model M3A-HP, MPR 0.09

Figure 31 Color Schlieren Images

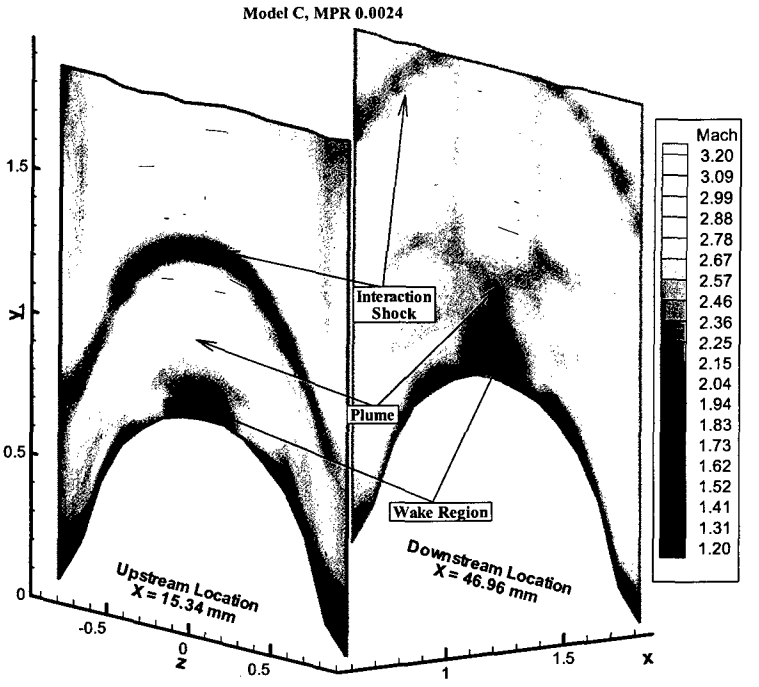

(a) Model M1A, MPR 0.006

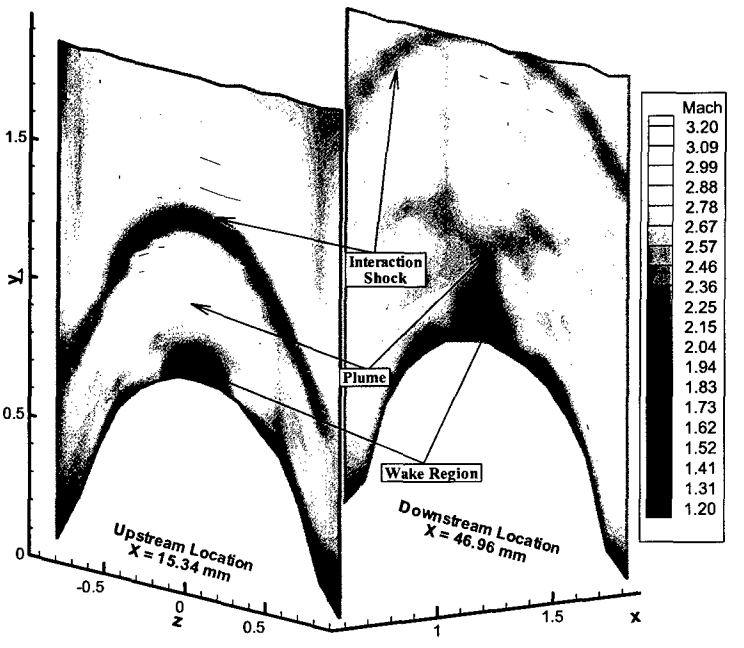

(b) Model M1A, MPR 0.005

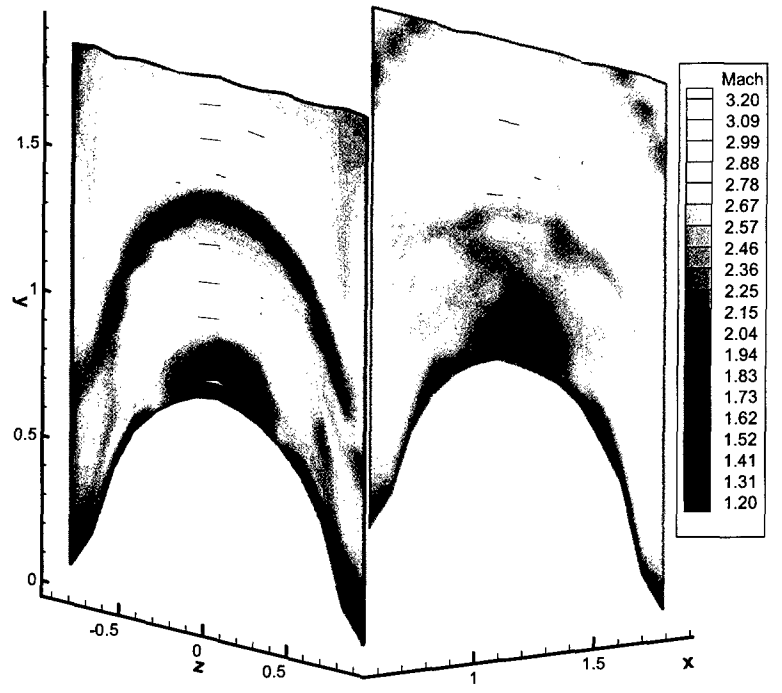

(c) Model M3A-LP, MPR 0.03

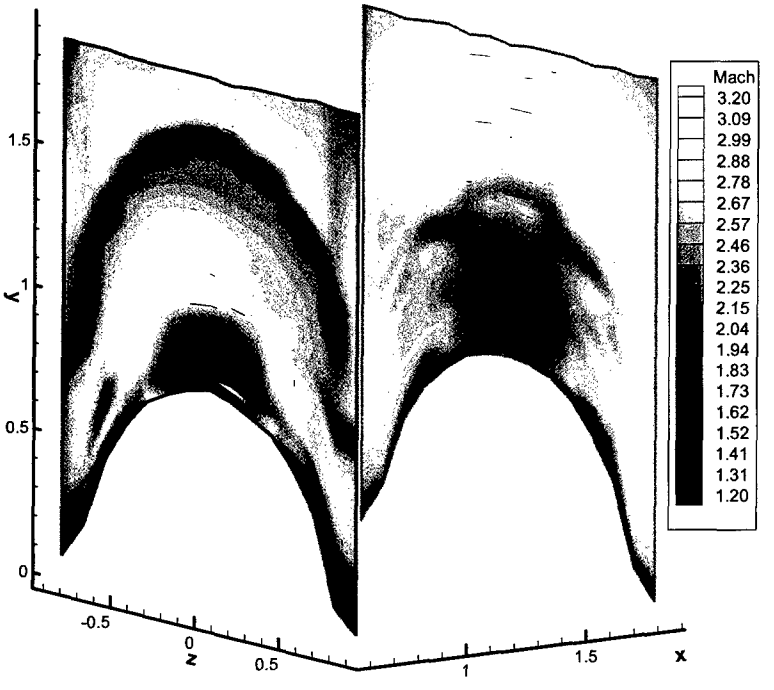

(d) Model M3A-LP, MPR 0.06

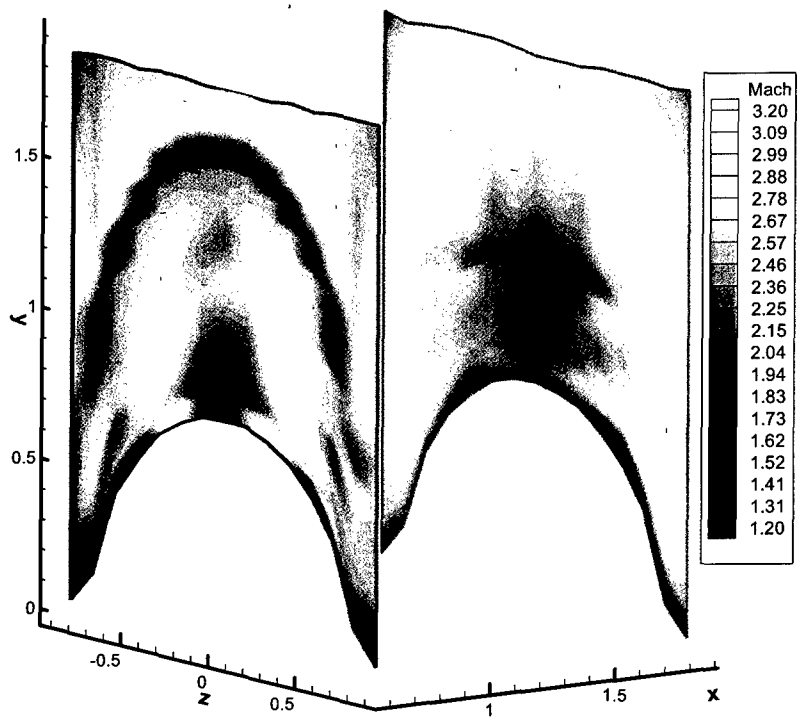

(e) Model M3A-HP, MPR 0.05

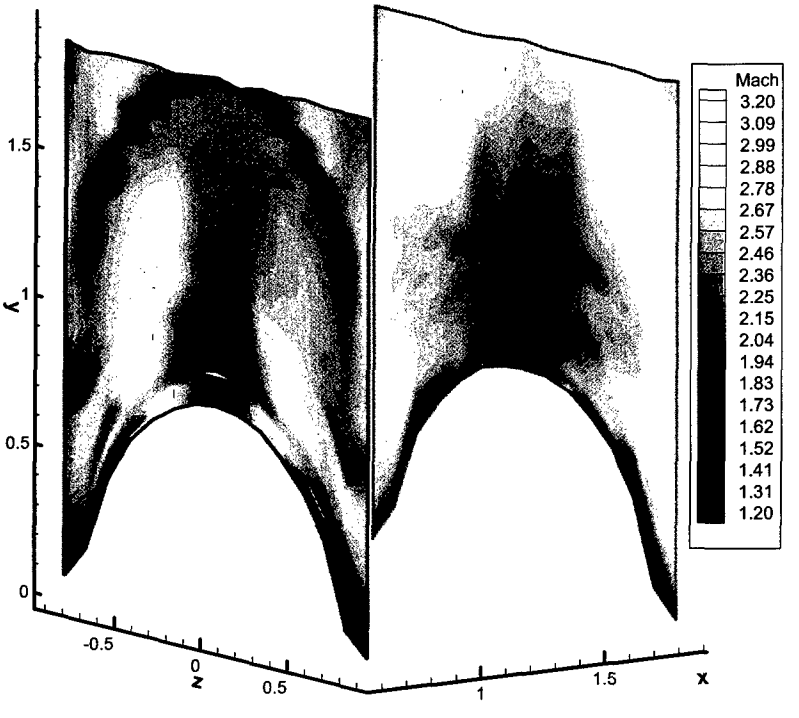

(f) Model M3A-HP, MPR 0.09

Figure 32 Mach Number Contours

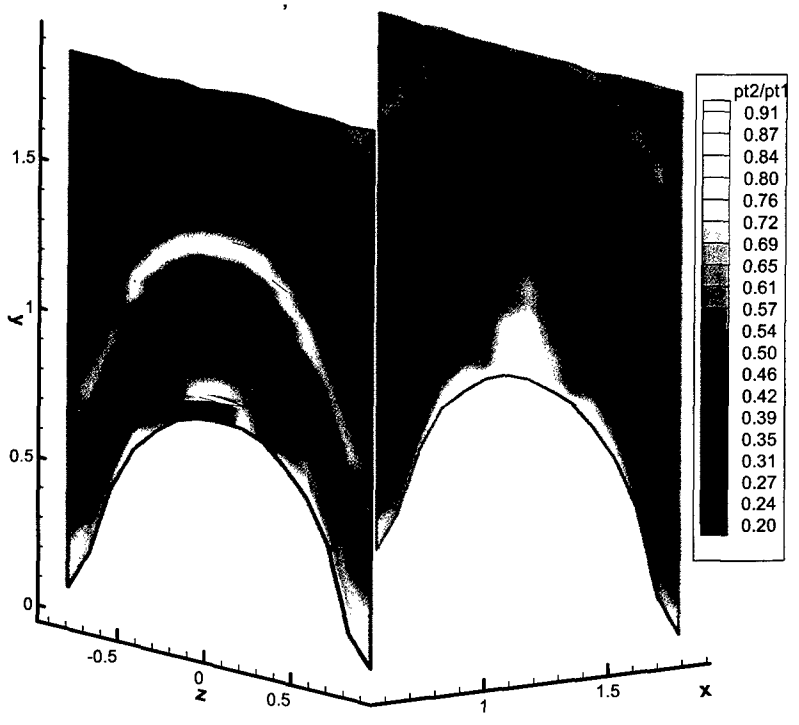

(a) Model M1A, MPR 0.006

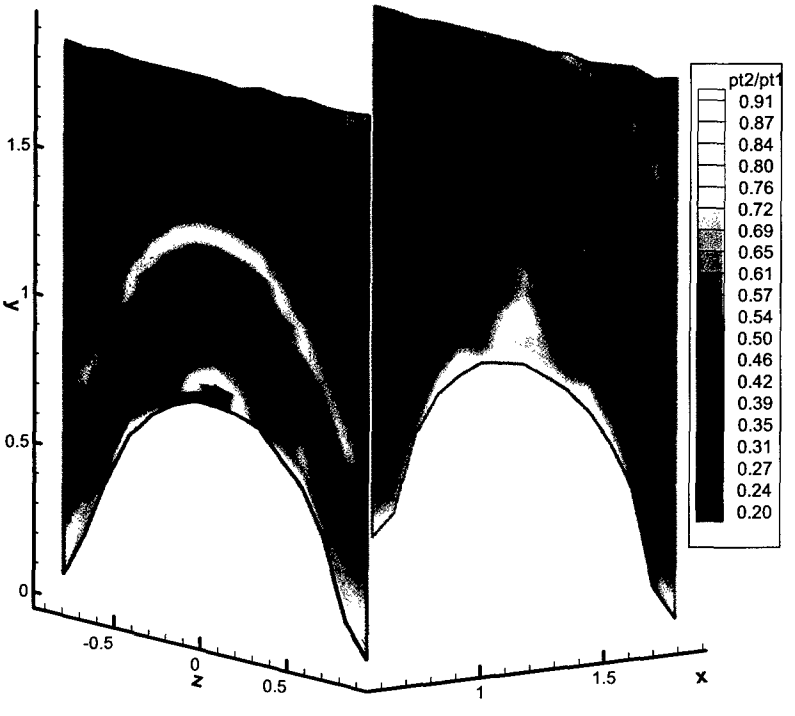

(b) Model M1A, MPR 0.005

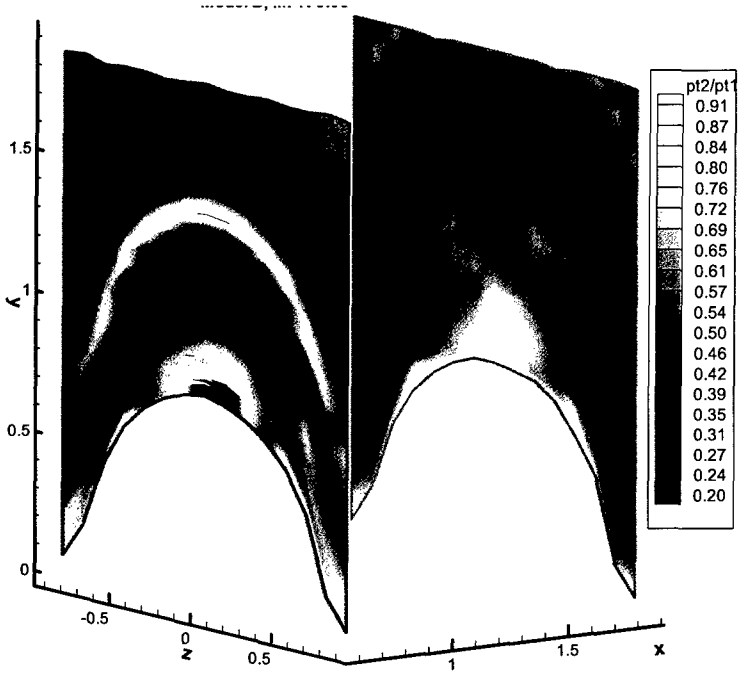

(c) Model M3A-LP, MPR 0.03

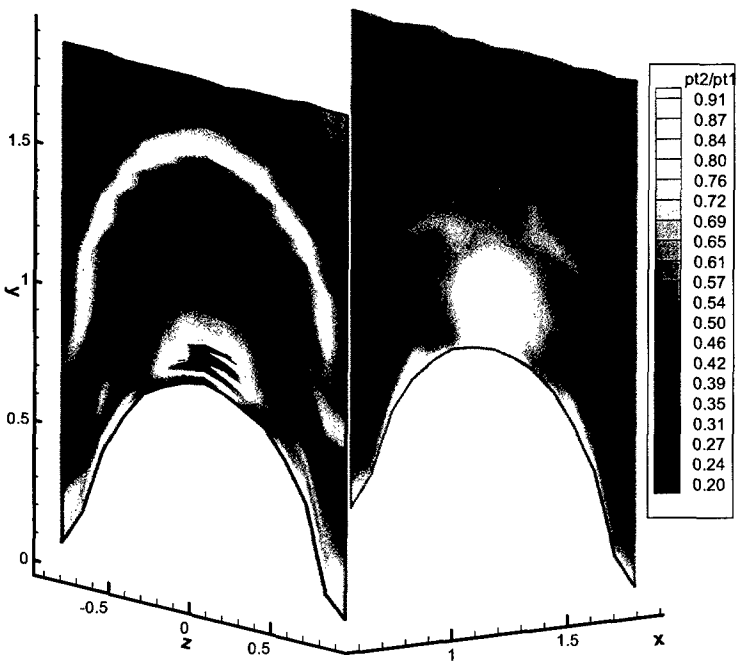

(d) Model M3A-LP, MPR 0.06

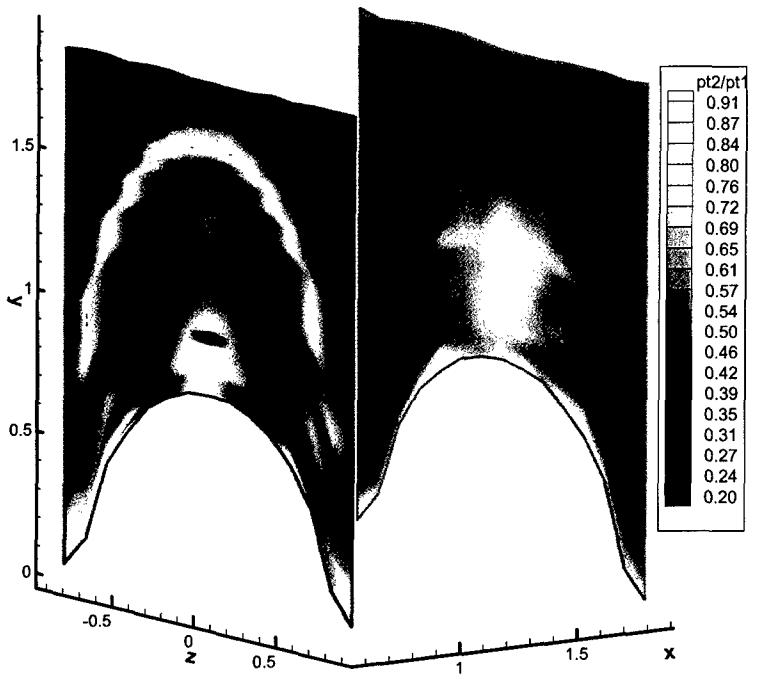

(e) Model M3A-HP, MPR 0.05

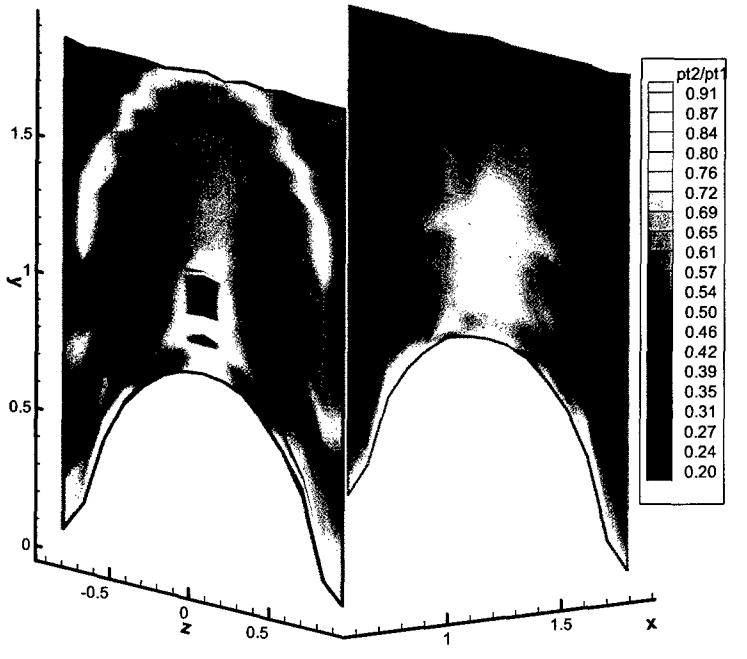

(f) Model M3A-HP, MPR 0.09

Figure 33 Contours of the total pressure ratio (P_{t2}/P_{t1}) across the Pitot probe shock

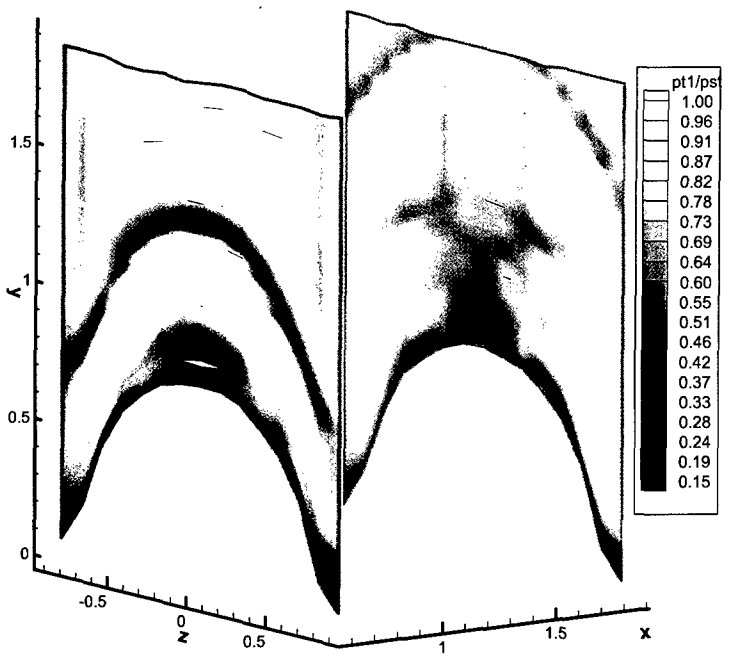

(a) Model M1A, MPR 0.006

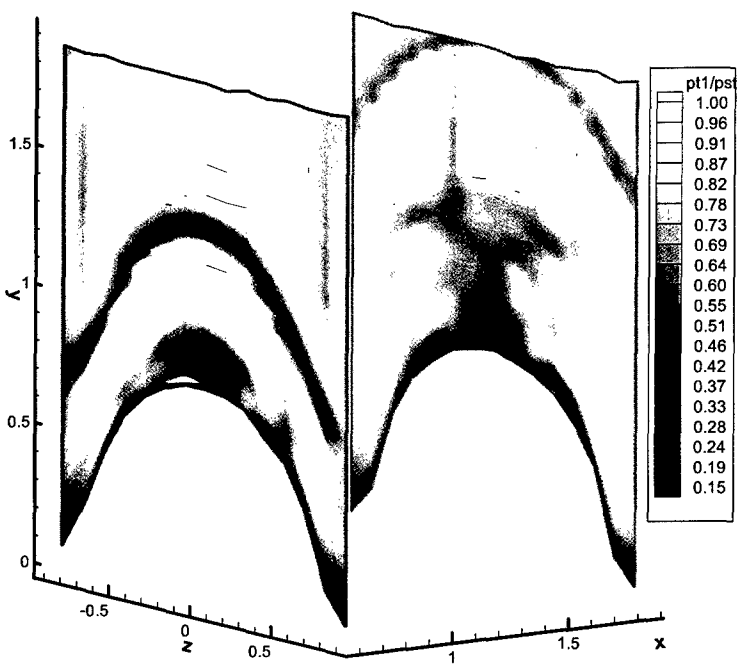

(b) Model M1A, MPR 0.005

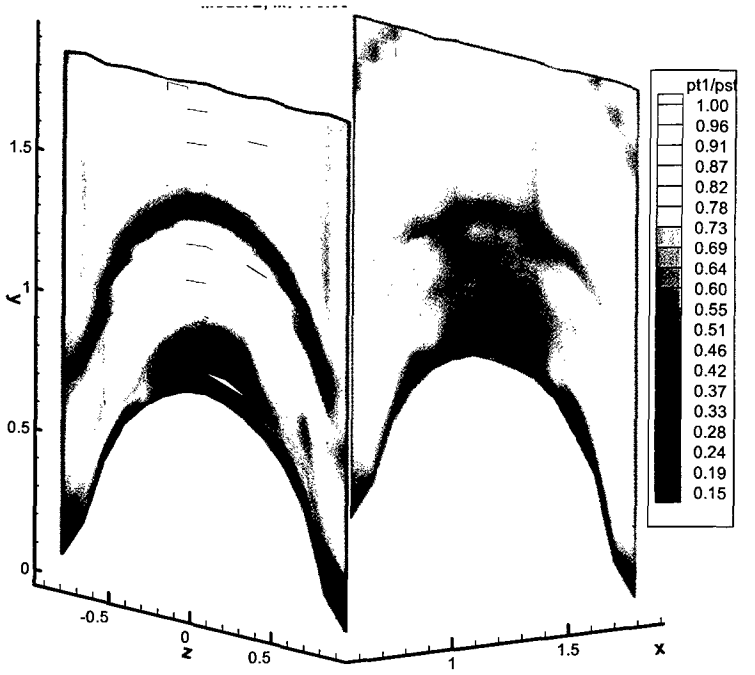

(c) Model M3A-LP, MPR 0.03

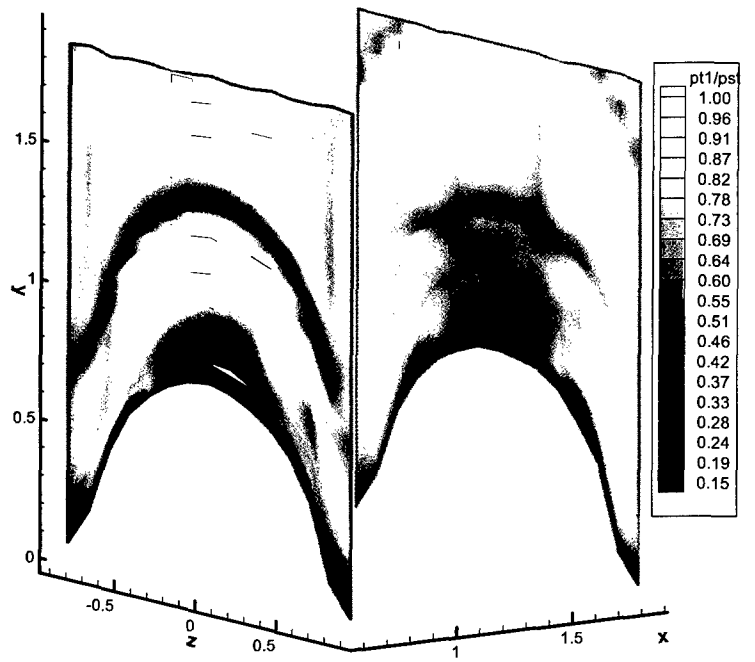

(d) Model M3A-LP, MPR 0.06

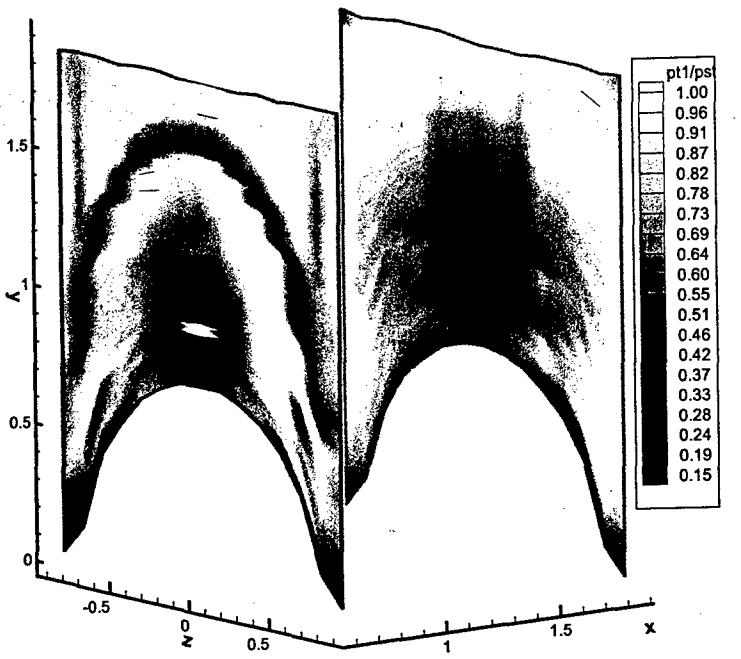

(e) Model M3A-HP, MPR 0.05

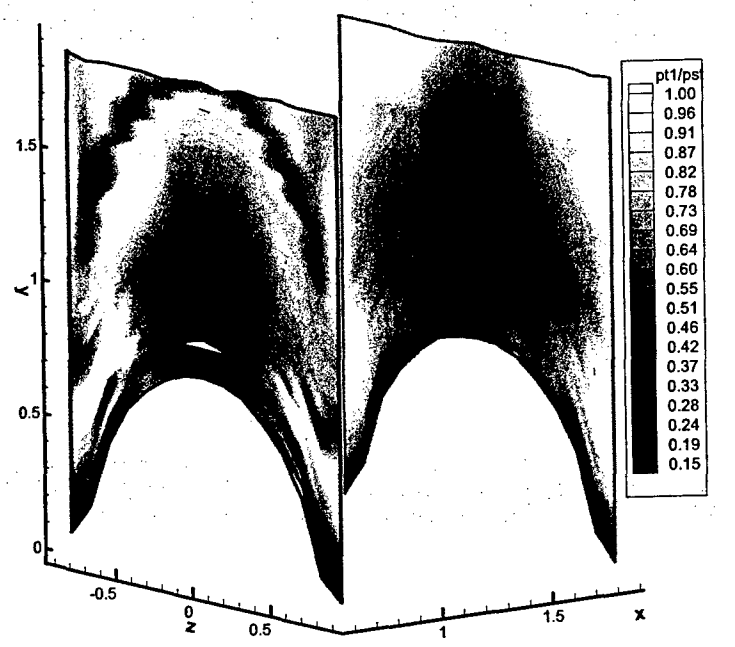

(f) Model M3A-HP, MPR 0.09

Figure 34 Total Pressure ($P_{t1}/P_{t\infty}$) Contours

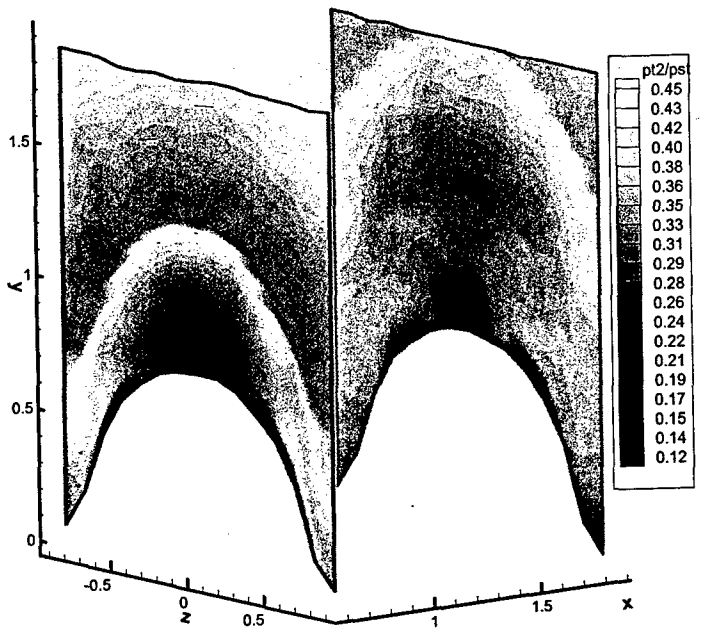

(a) Model M1A, MPR 0.006

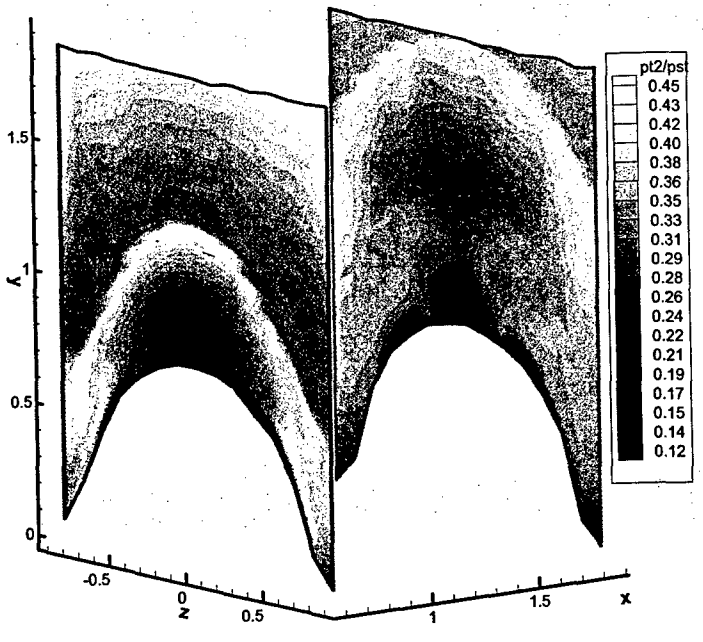

(b) Model M1A, MPR 0.005

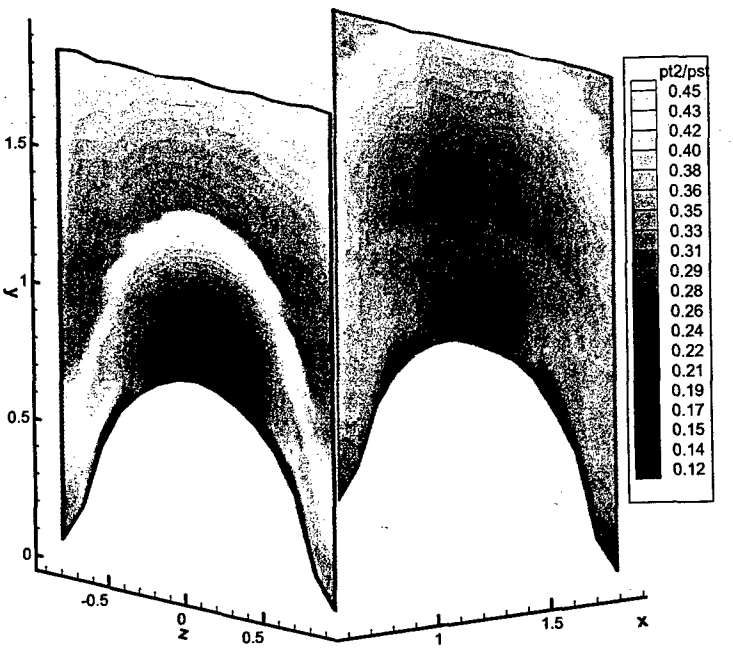

(c) Model M3A-LP, MPR 0.03

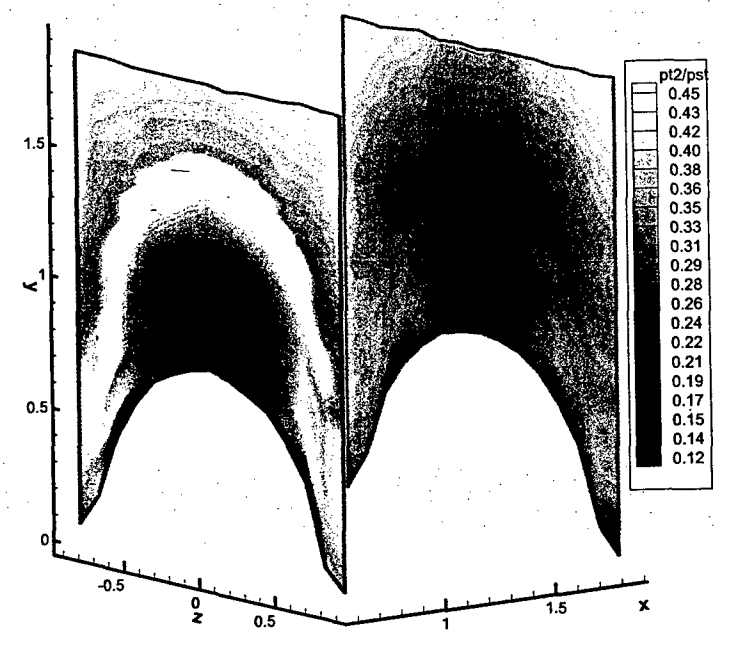

(d) Model M3A-LP, MPR 0.06

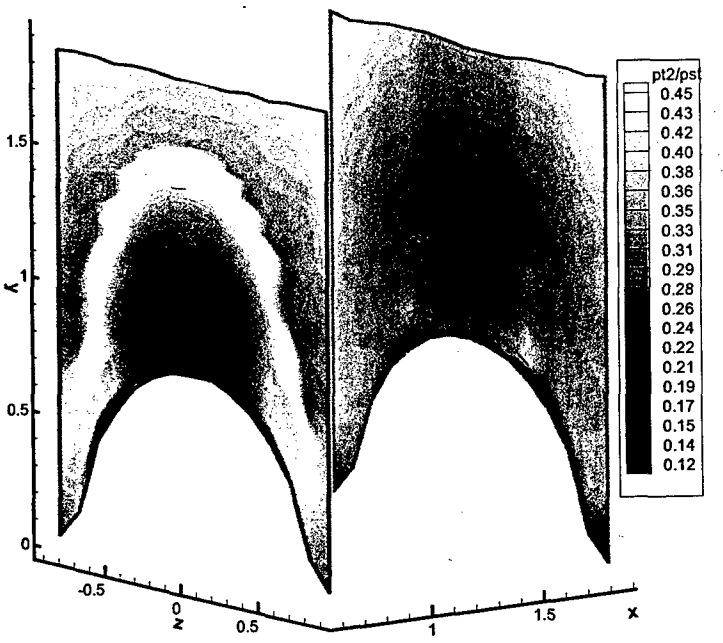

(e) Model M3A-HP, MPR 0.05

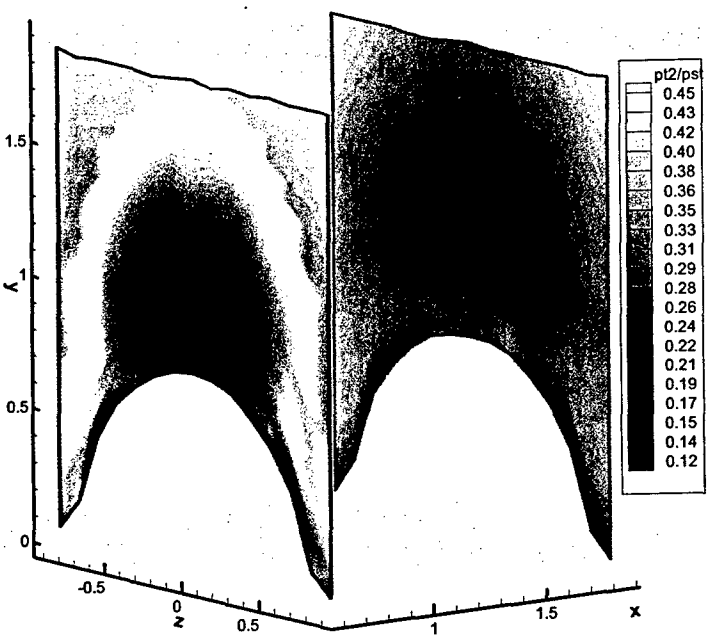

(f) Model M3A-HP, MPR 0.09

Figure 35 Pitot Pressure ($P_{t2}/P_{t\infty}$) Contours

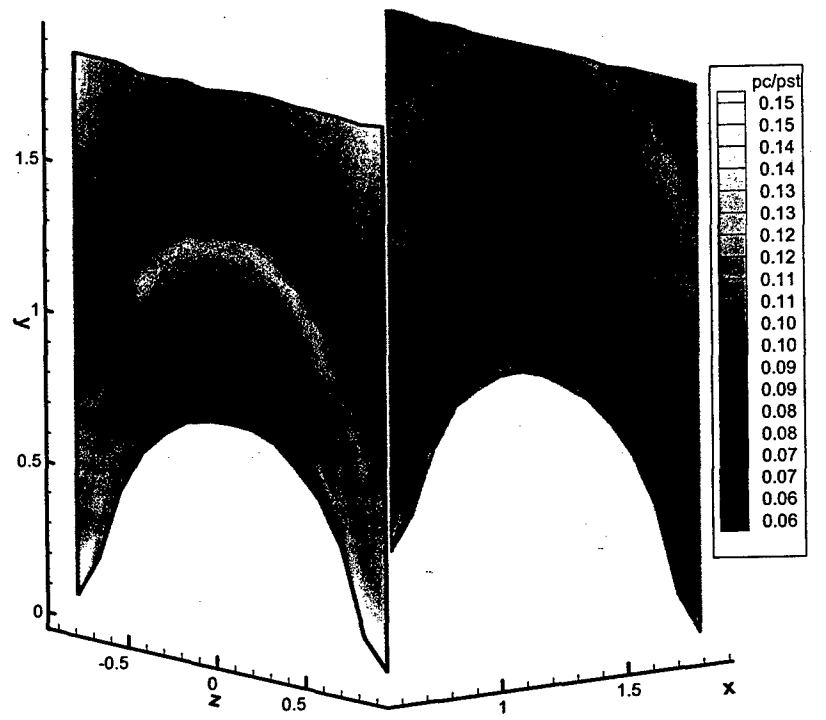

(a) Model M1A, MPR 0.006

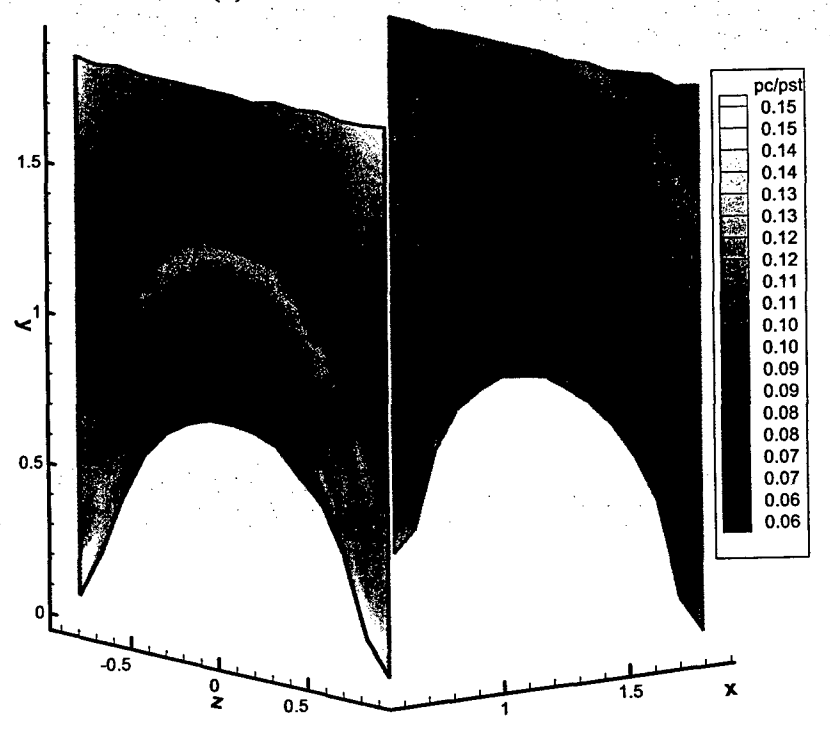

(b) $P_c/P_{t\infty}$ contour, model M1A, MPR 0.005

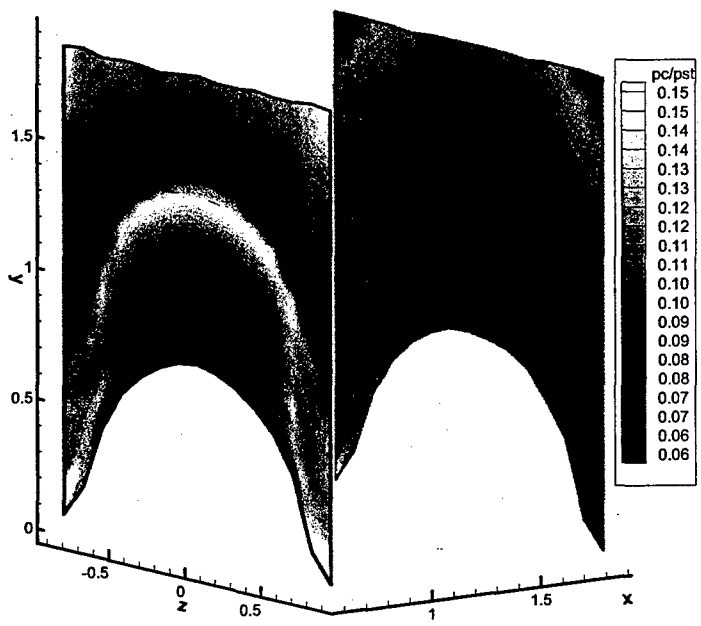

(c) Model M3A-LP, MPR 0.03

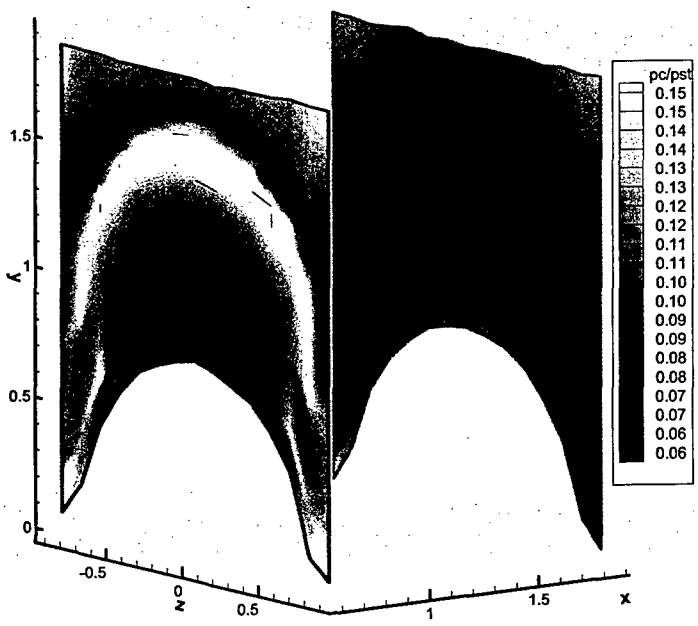

(d)Model M3A-LP, MPR 0.06

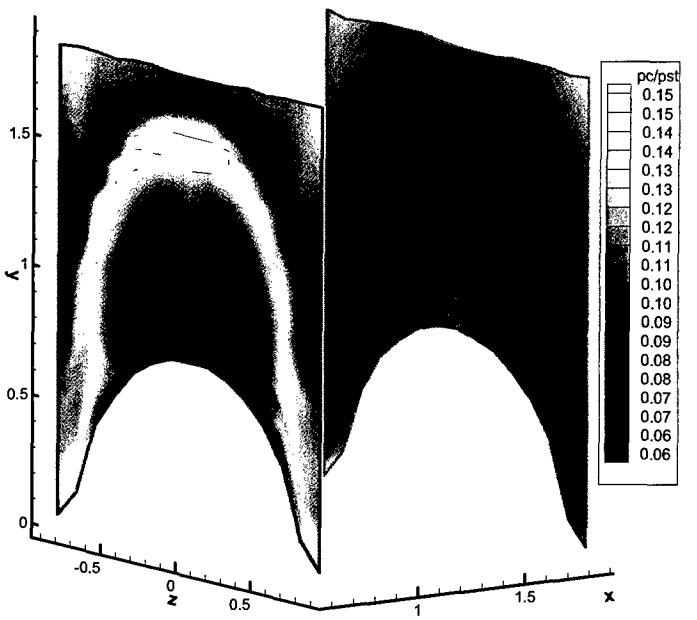

(e) Model M3A-HP, MPR 0.05

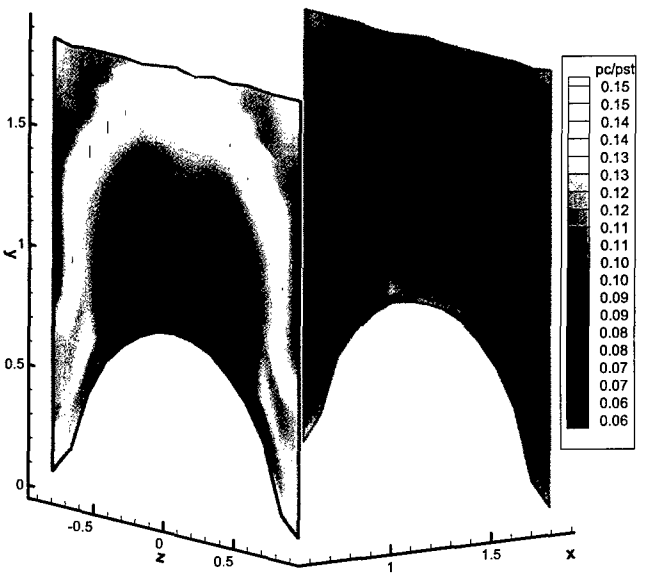

(f) Model M3A-HP, MPR 0.09

Figure 36 Cone-Static Pressure ($P_c/P_{t\infty}$) Contours

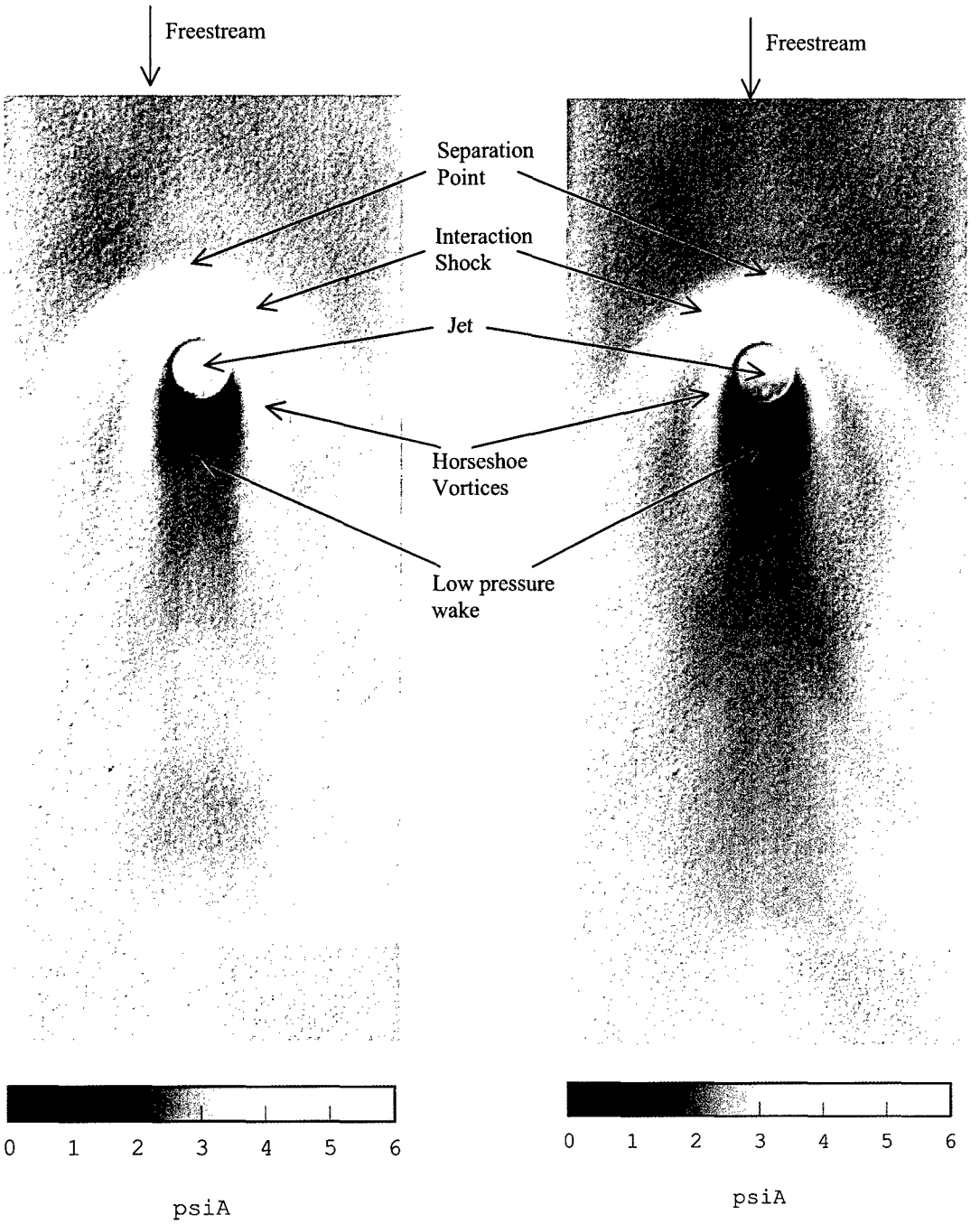

(a) MPR 0.006 **(b) MPR 0.005**

Figure 37 Surface pressure contour (Model M1A)

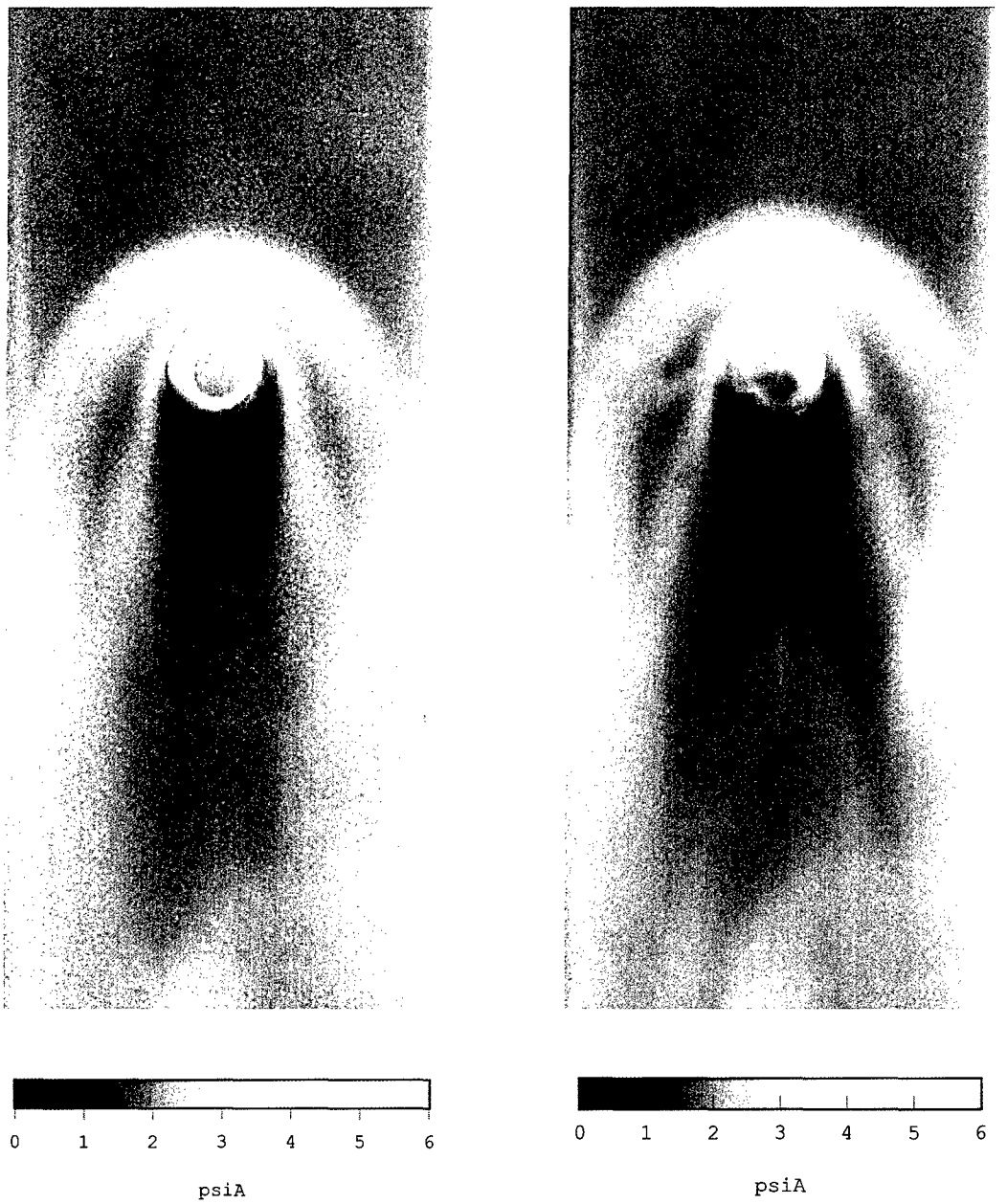

(a) MPR 0.03 **(b) MPR 0.06**

Figure 38 Surface pressure contour (Model M3A-LP)

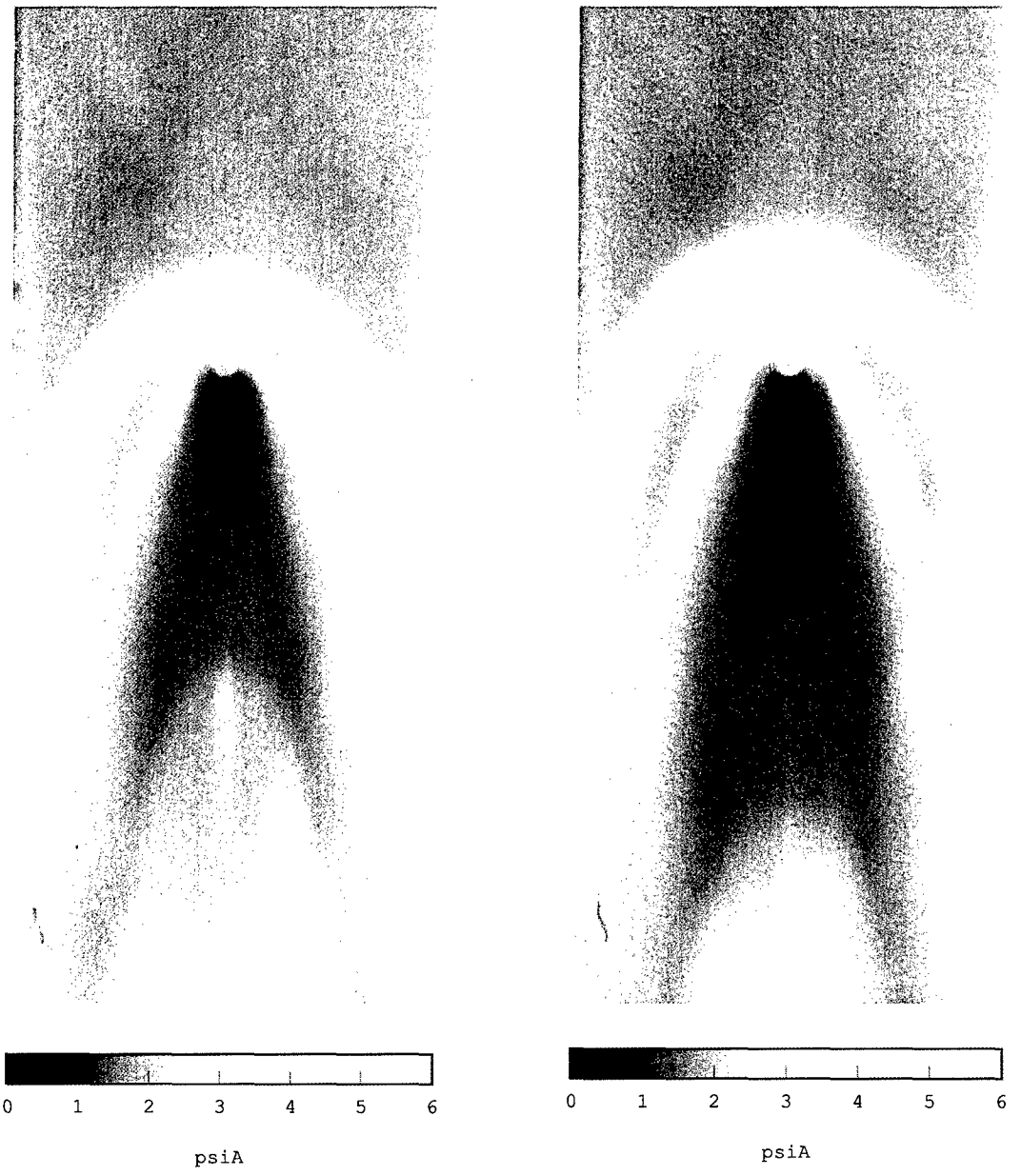

(a) MPR 0.05 **(b) MPR 0.09**

Figure 39 Surface pressure contour (Model M3A-HP)

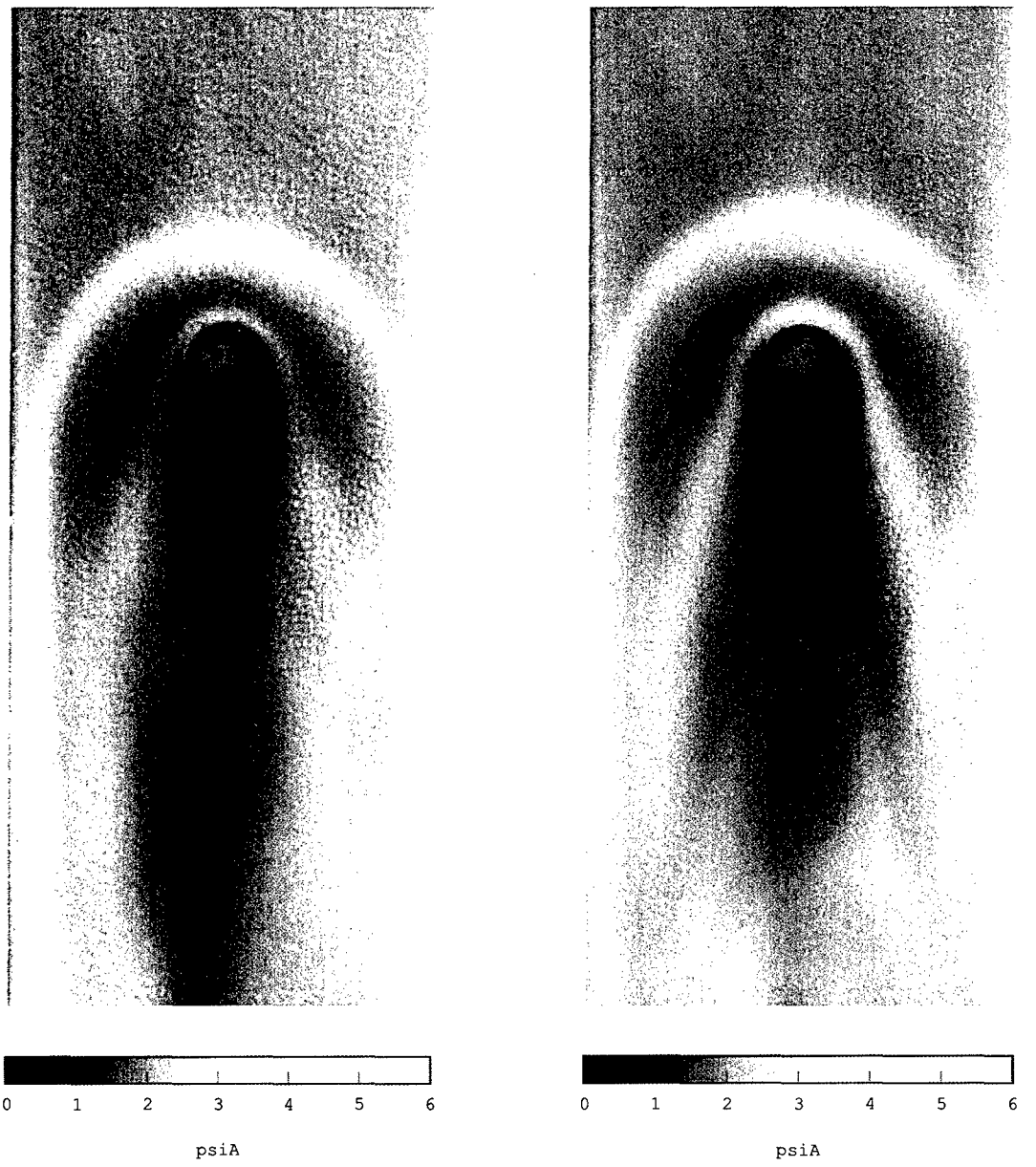

(a) MPR 0.03 **(b) MPR 0.05**

Figure 40 Surface pressure contour (Model M3H)

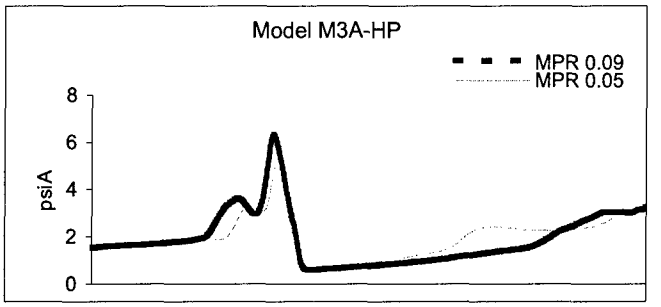

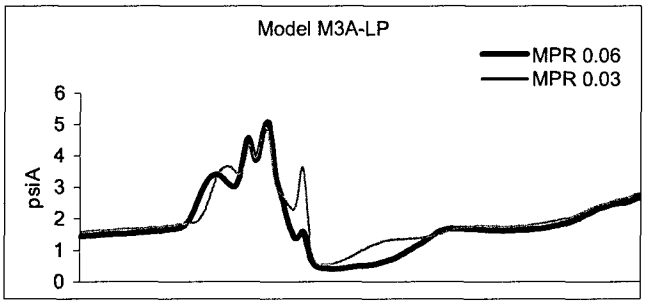

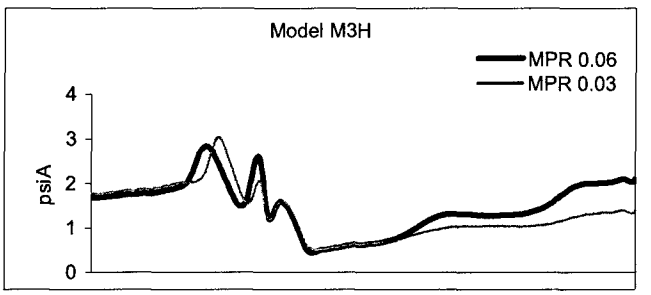

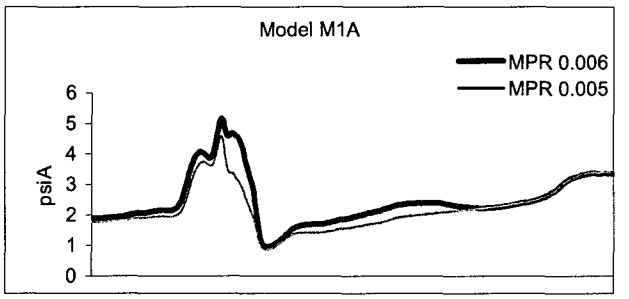

Figure 41 Effect of jet MPR on the centerline surface pressure

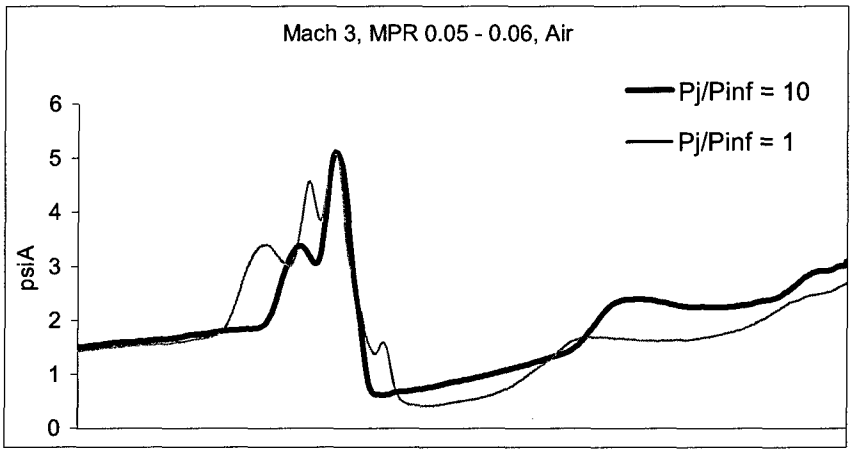

Figure 42 Effect of jet pressure ratio on the centerline surface pressure

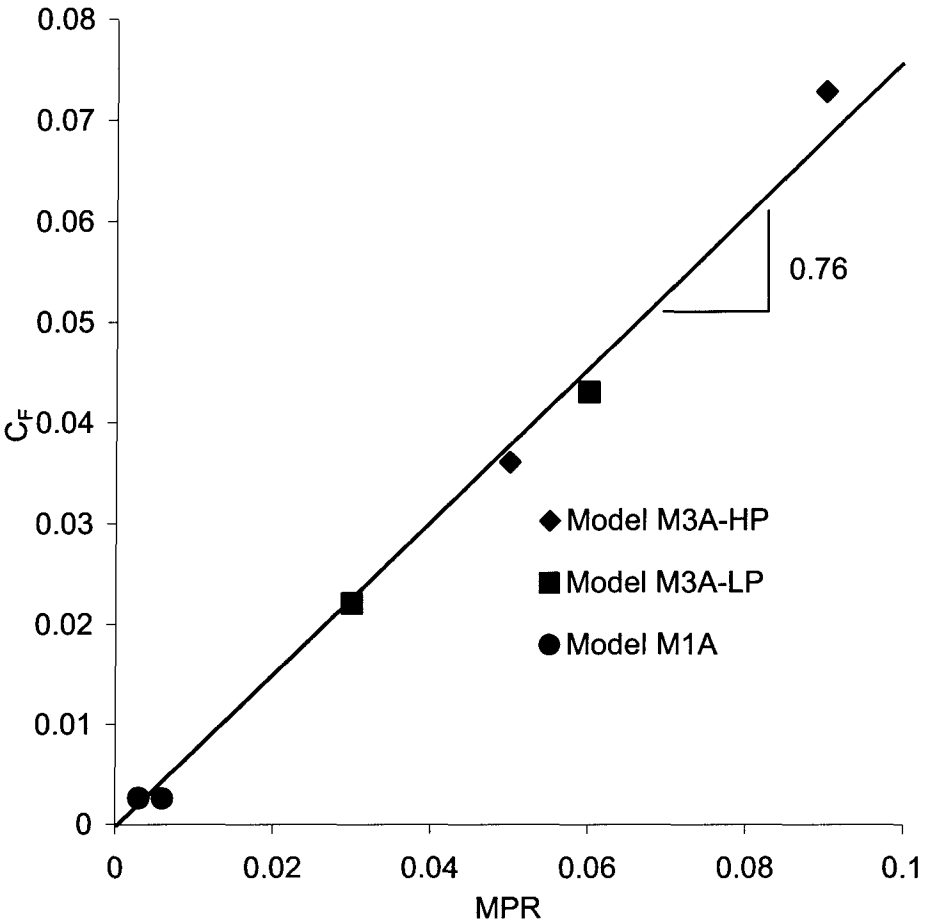

Figure 43 Total Force Coefficient vs. MPR

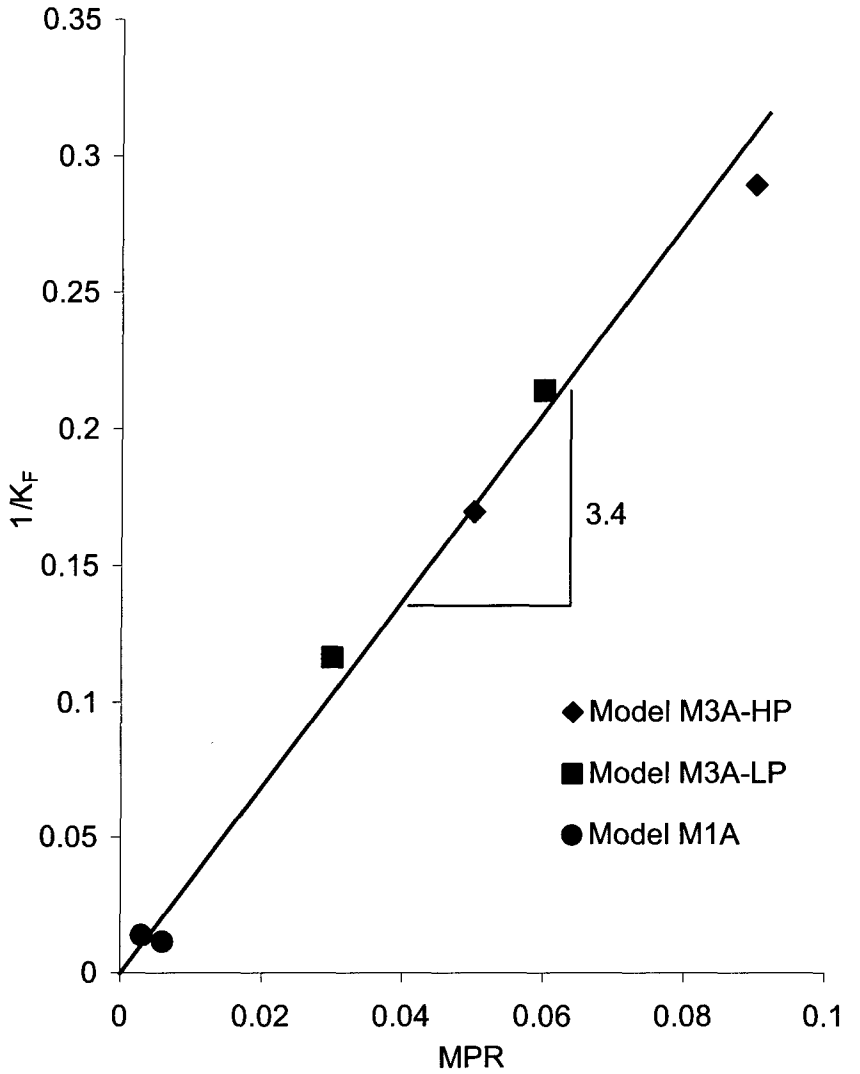

Figure 44 Amplification Factor vs. MPR

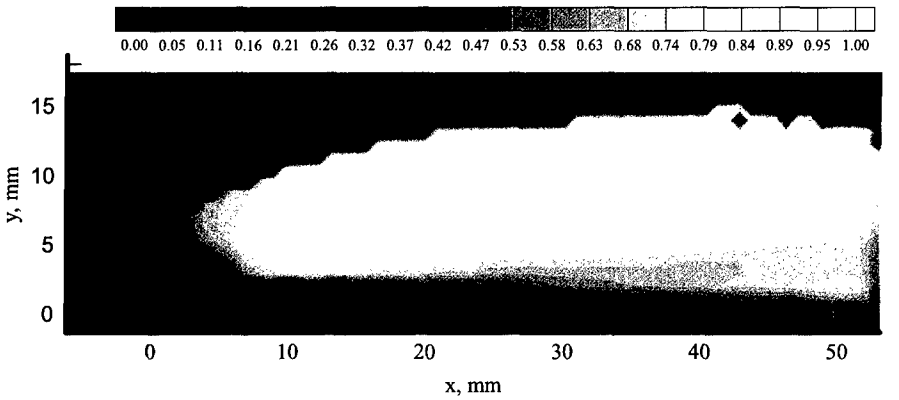

(a) z = 0

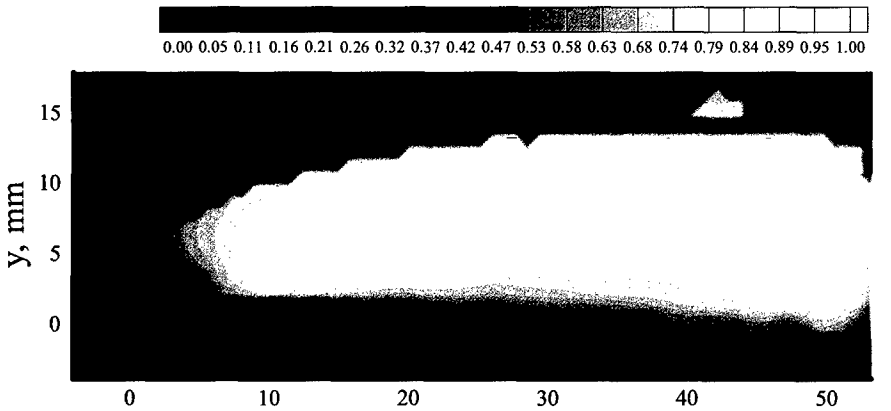

(b) z = 1.59 mm

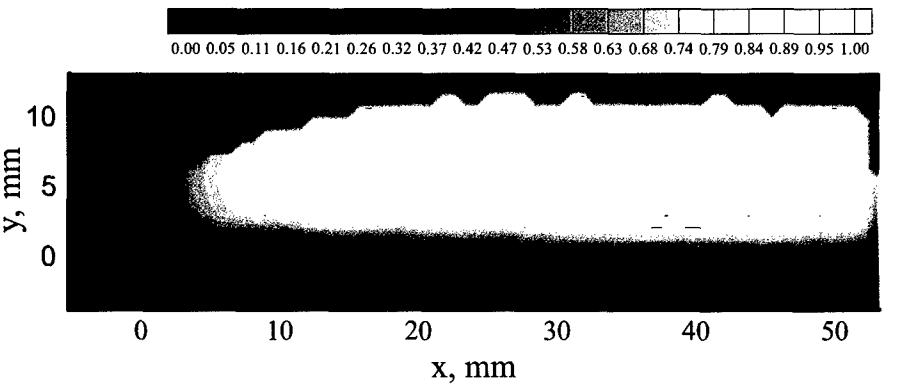

(c) z = 3.18 mm

Figure 45 Mean axial velocity contours, $\overline{u}/u_{\infty}$ (Model M1A, MPR = 0.006)

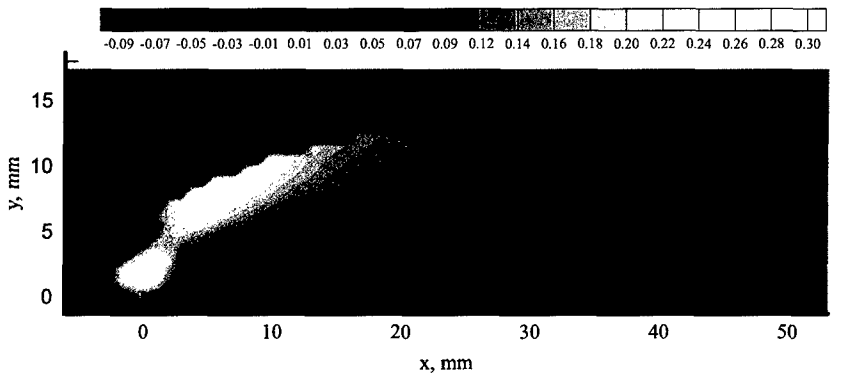

(a) z = 0

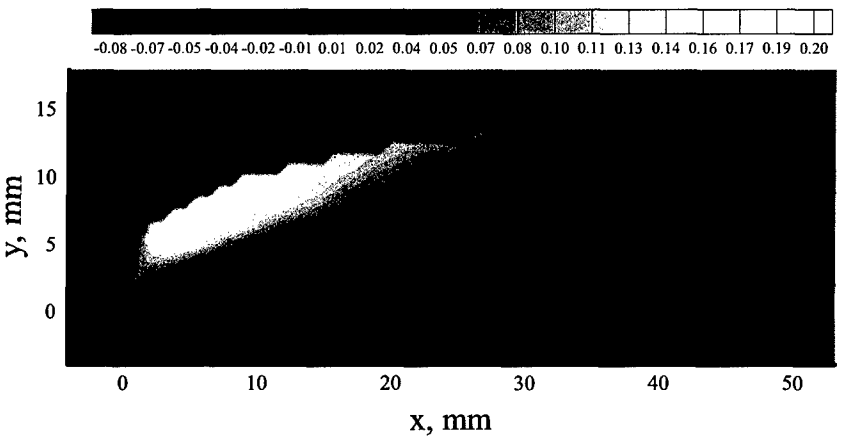

(b) z = 1.59 mm

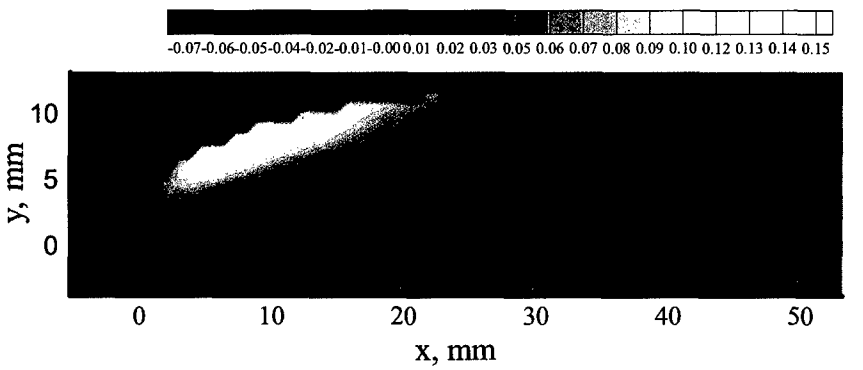

(c) z = 3.18 mm

Figure 46 Mean transverse velocity contours, $\overline{v}/u_\infty$ (Model M1A, MPR = 0.006)

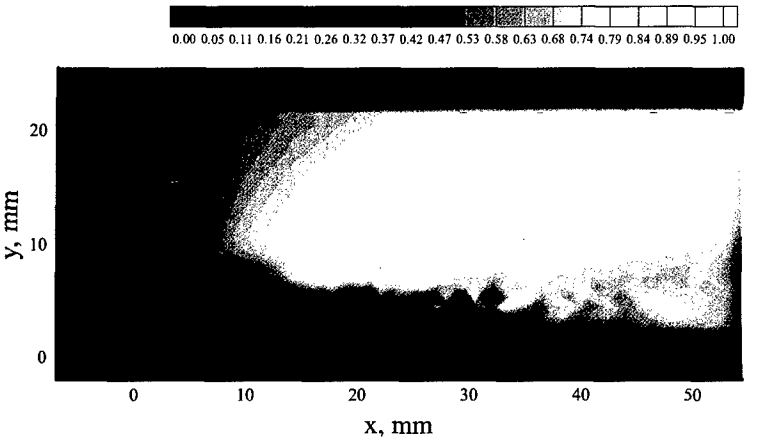

(a) z = 0

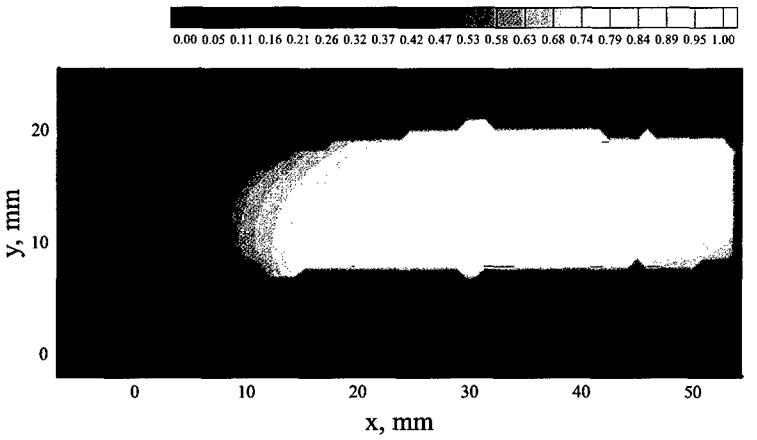

(b) z = 1.59 mm

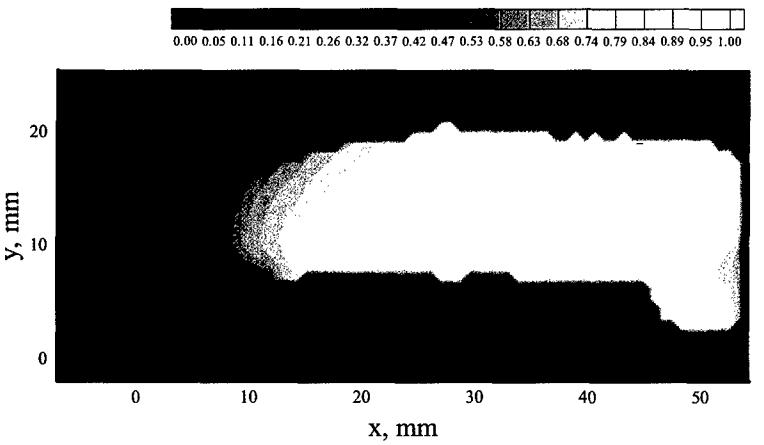

(c) z = 3.18 mm

Figure 47 Mean axial contours, $\overline{u}/u_{\infty}$ (Model M3A-LP, MPR = 0.06)

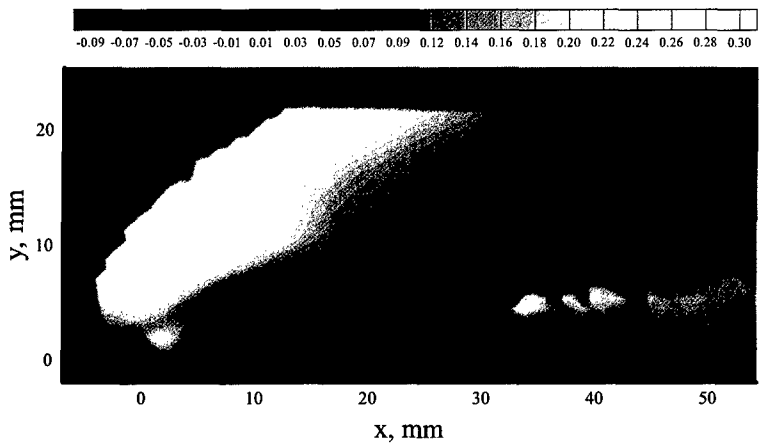

(a) z = 0

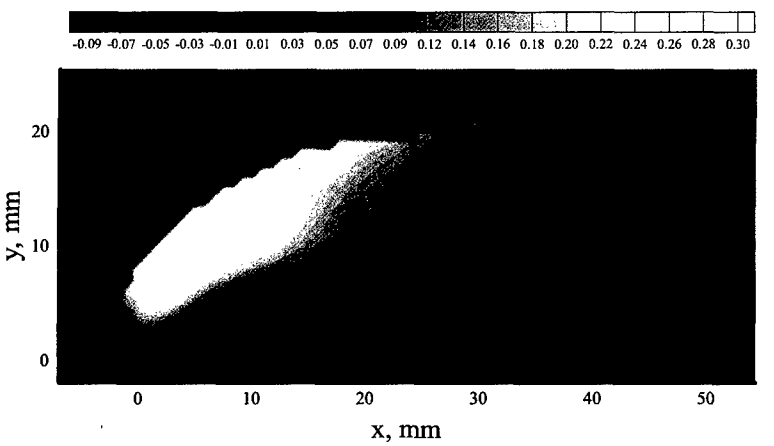

(b) z = 1.59 mm

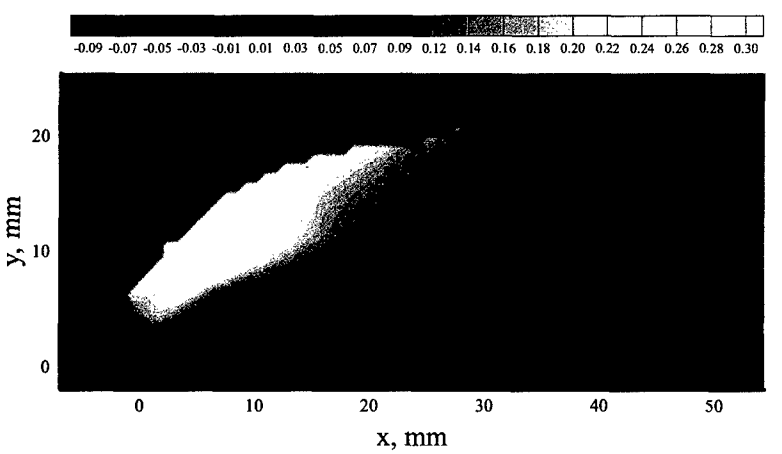

(c) z = 3.18 mm

Figure 48 Mean transverse velocity contours, $\overline{v} / u_{\infty}$ (Model M3A-LP, MPR = 0.06)

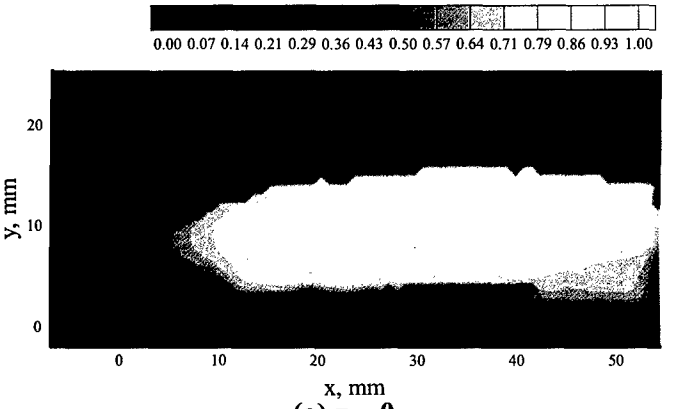

(a) z = 0

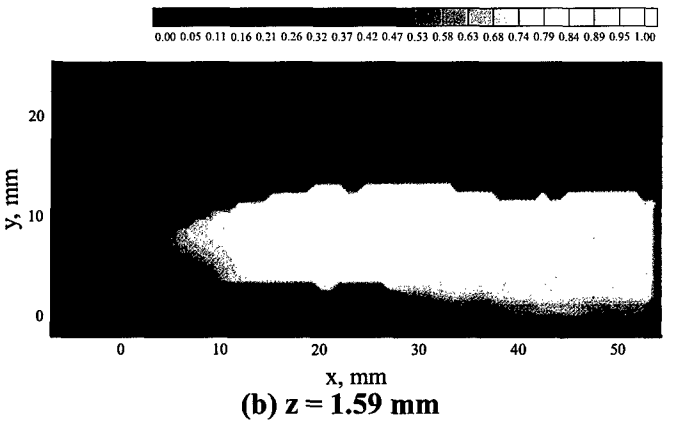

(b) z = 1.59 mm

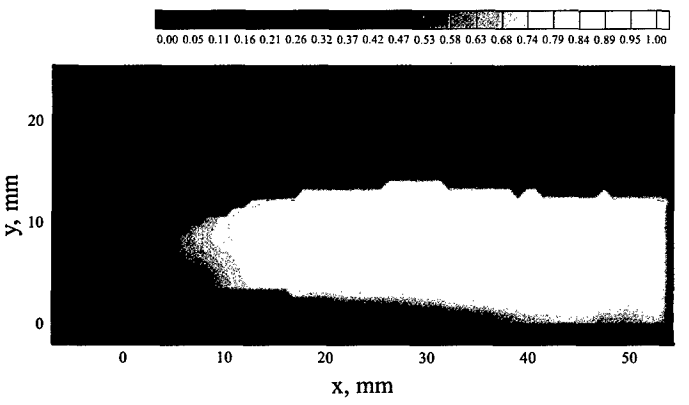

(c) z = 3.18 mm

Figure 49 Axial Velocity Contours, $\bar{u} / u_{\infty}$ (Model M3A-LP, MPR = 0.03)

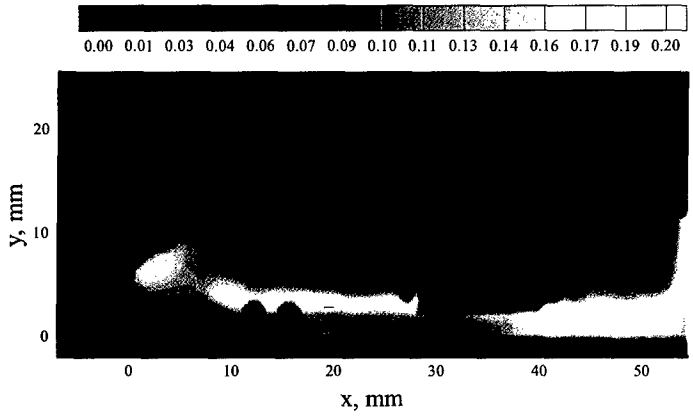

(a) z = 0

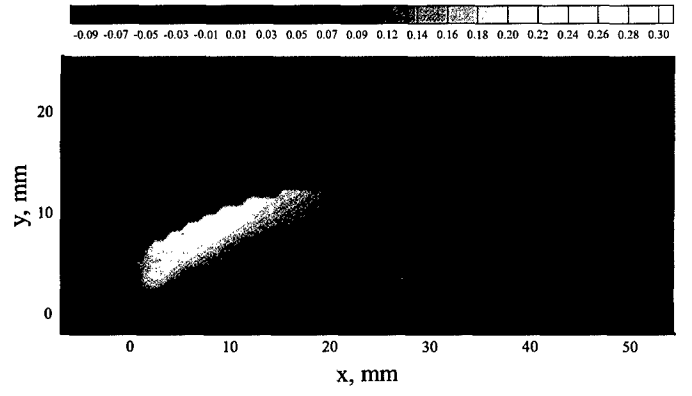

(b) z = 1.59 mm

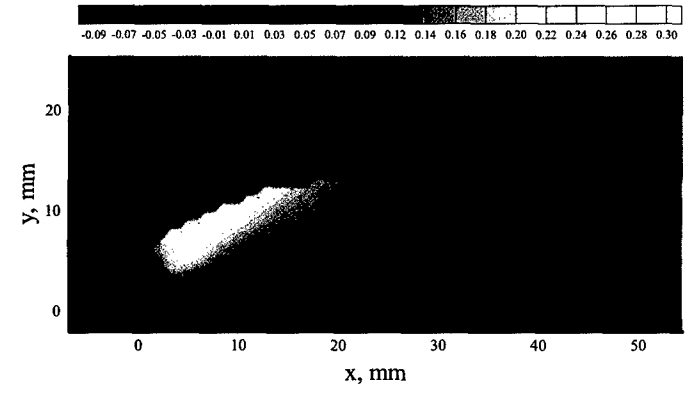

(c) z = 3.18 mm

Figure 50 Mean Transverse Velocity, $\overline{v}/u_\infty$ (Model M3A-LP, MPR = 0.03)

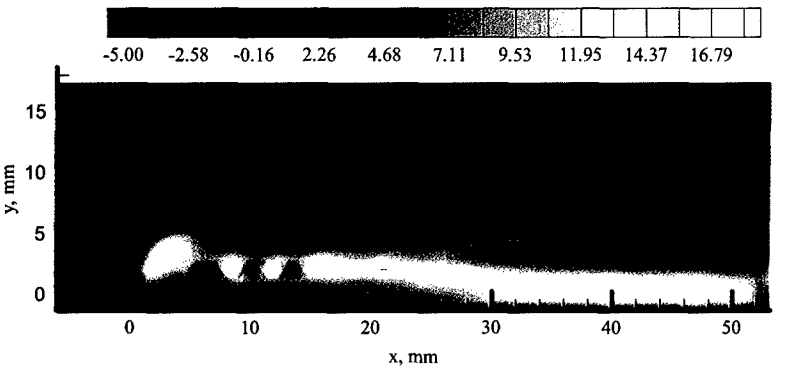

(a) z = 0

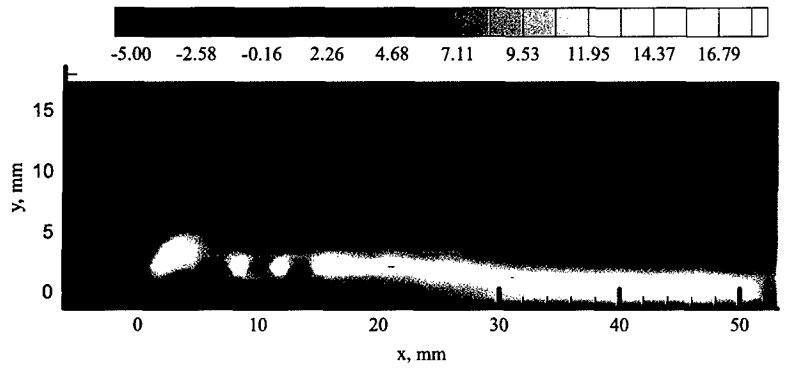

(b) z = 1.59 mm

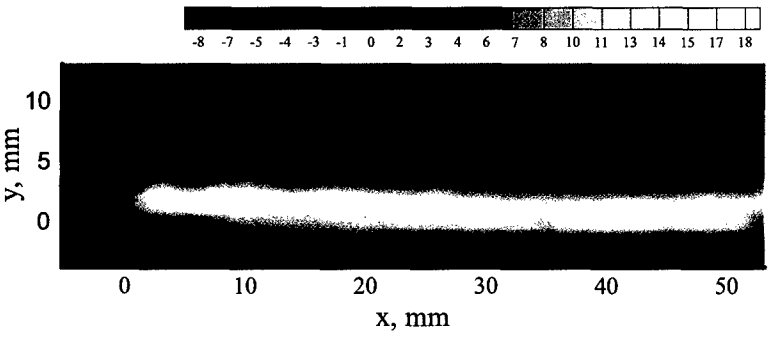

(c) z = 3.18 mm

Figure 51 Vorticity, $(\partial\overline{u}/\partial y - \partial\overline{v}/\partial x)\cdot D/u_\infty$ (Model M1A, MPR = 0.006)

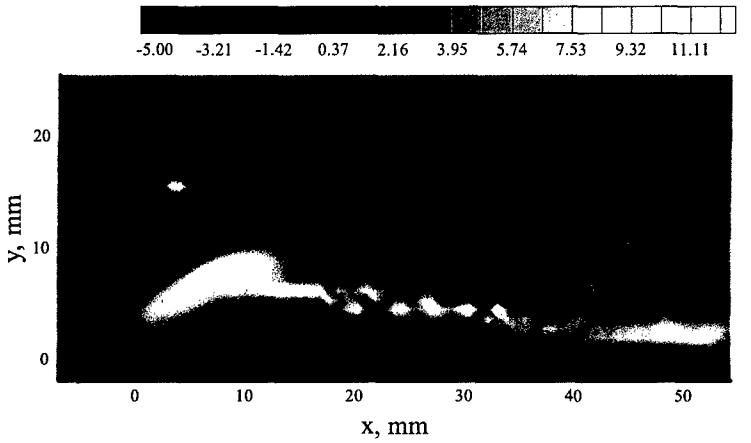

(a) z = 0

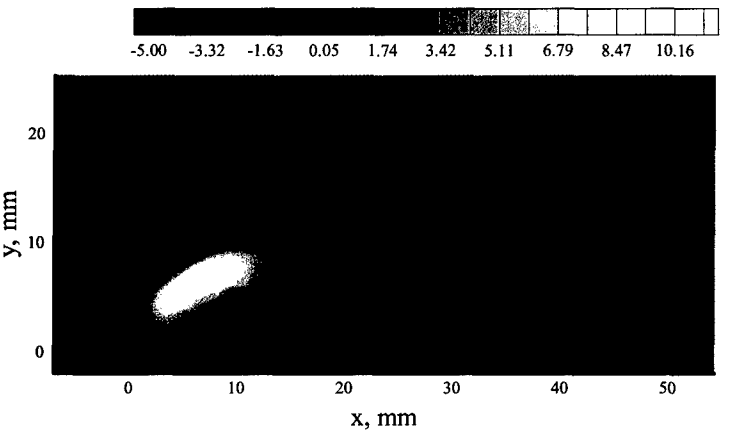

(c) z = 1.59 mm

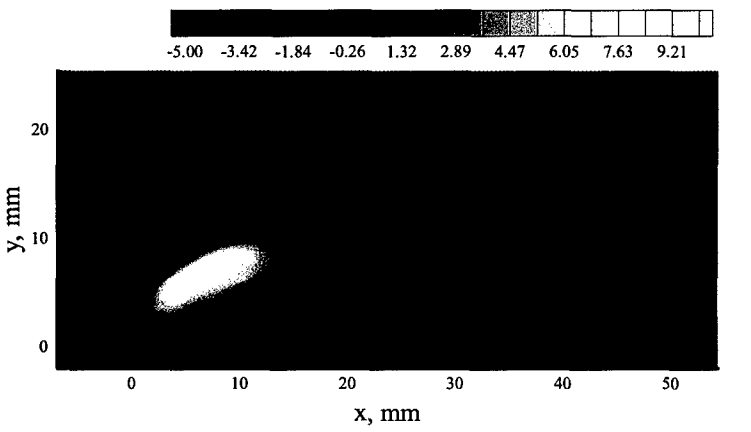

(c) z = 3.18 mm

Figure 52 Vorticity, $(\partial\overline{u}/\partial y - \partial\overline{v}/\partial x)\cdot D/u_\infty$ (Model M3A-LP, MPR = 0.06)

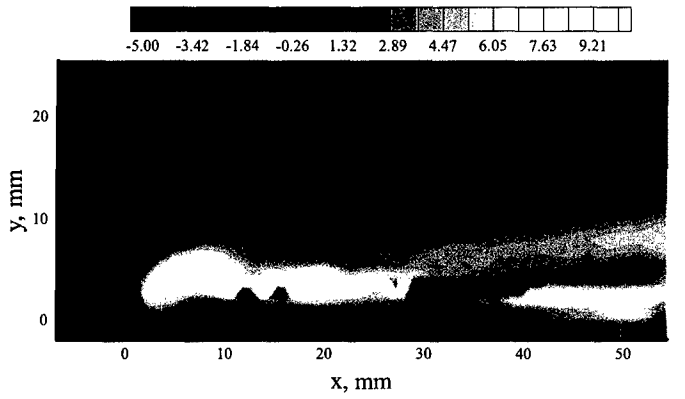

(a) z = 0

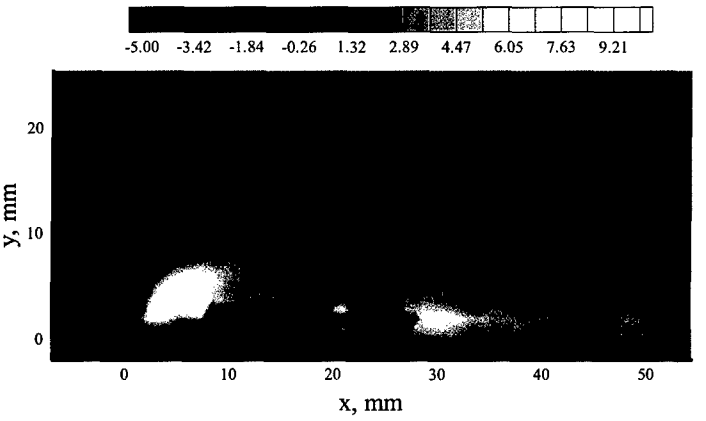

(d) z = 1.59 mm

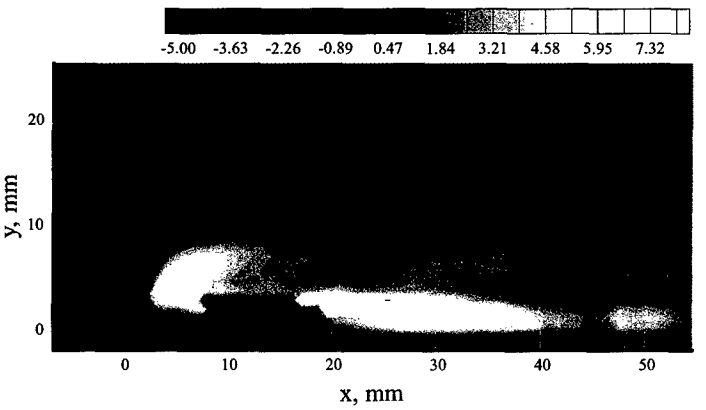

(c) z = 3.18 mm

Figure 53 Vorticity, $(\partial\overline{u}/\partial y - \partial\overline{v}/\partial x)\cdot D/u_\infty$ (Model M3A-LP, MPR = 0.03)

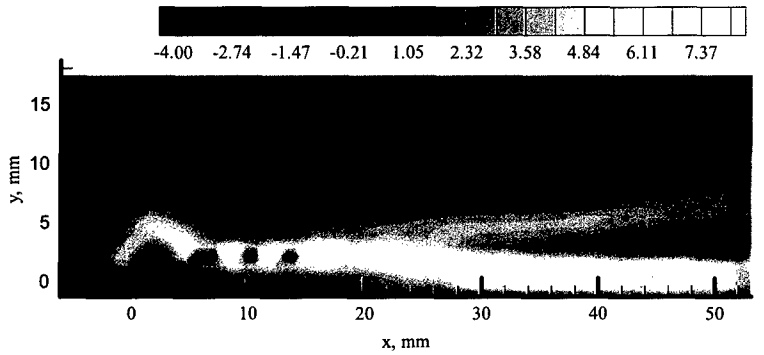

(a) z = 0

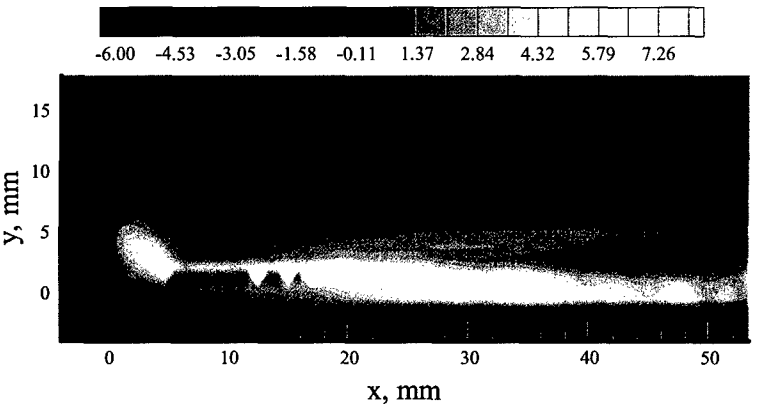

(b) z = 1.59 mm

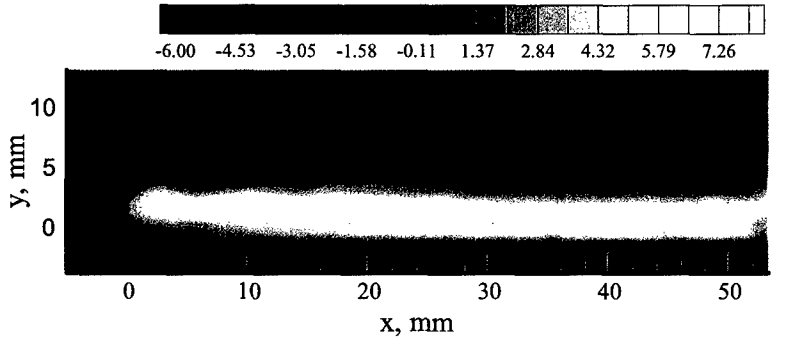

(c) z = 3.18 mm

Figure 54 Shear Strain, $(\partial\overline{u}/\partial y + \partial\overline{v}/\partial x)\cdot D/u_\infty$ (Model M1A, MPR = 0.006)

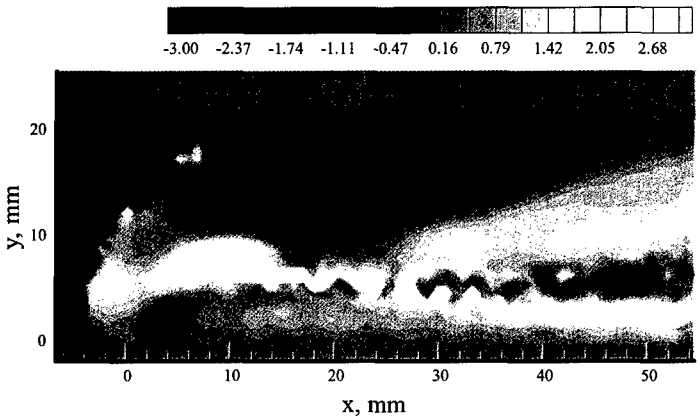

(a) z = 0

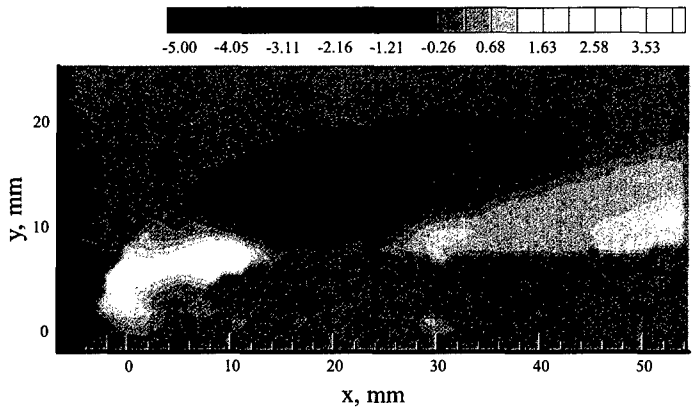

(b) z = 1.59 mm

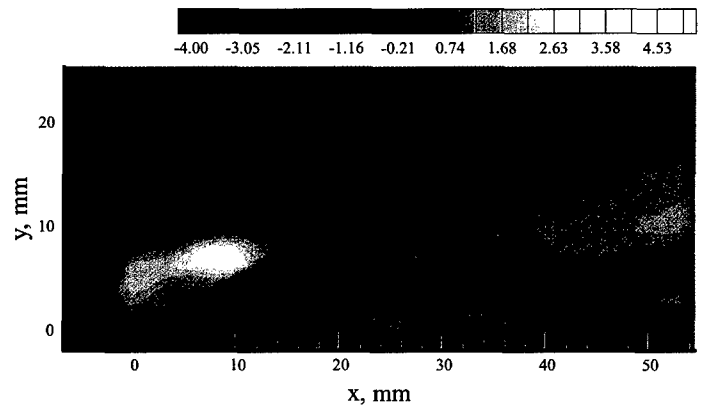

(c) z = 3.18 mm

Figure 55 Shear Strain, $(\partial\overline{u}/\partial y + \partial\overline{v}/\partial x)\cdot D/u_\infty$ (Model M3A-LP, MPR = 0.06)

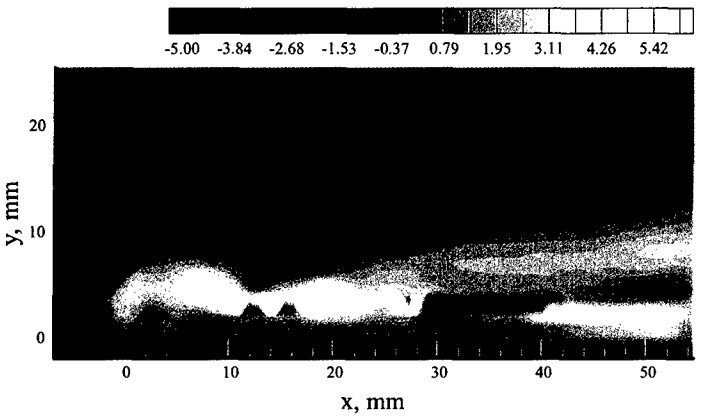

(a) z = 0

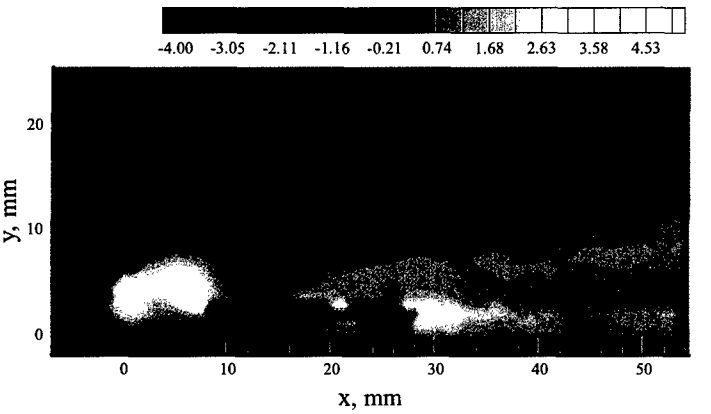

(b) z = 1.59 mm

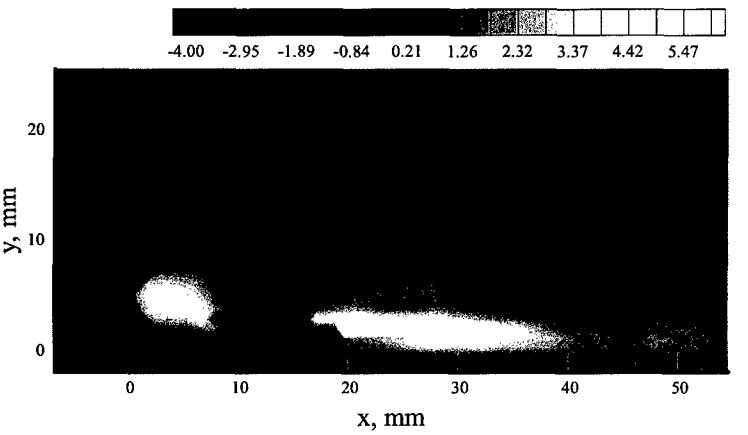

(c) z = 3.18 mm

Figure 56 Shear Strain, $(\partial\overline{u}/\partial y + \partial\overline{v}/\partial x)\cdot D/u_\infty$ (Model M3A-LP, MPR = 0.03)

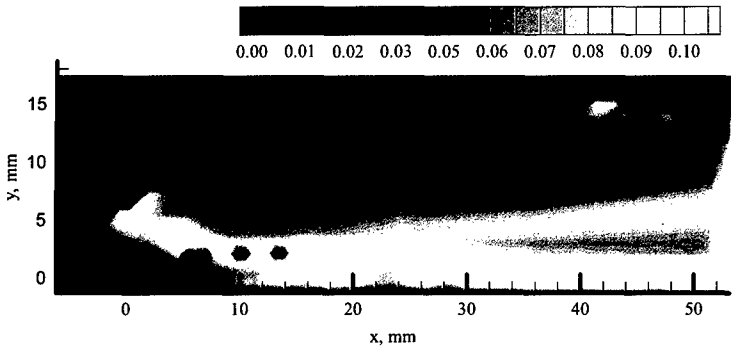

(a) z = 0

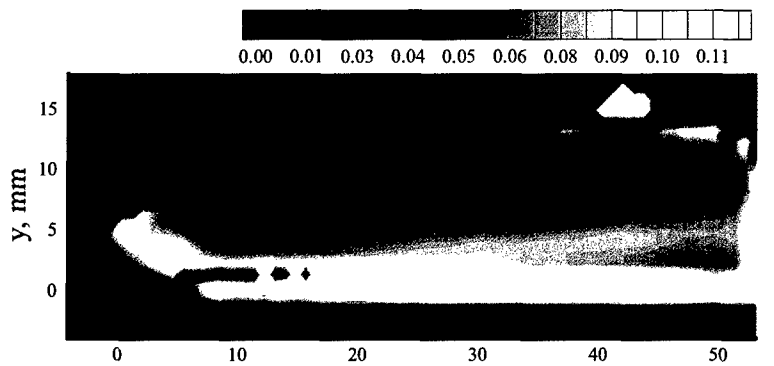

(b) z = 1.59 mm

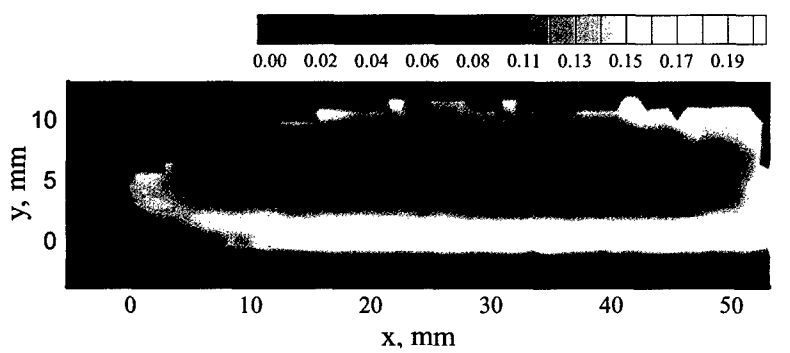

(c) z = 3.18 mm

Figure 57 Axial Turbulence Intensity, $\sqrt{\overline{u'^2}}/u_\infty$ (Model M1A, MPR = 0.006)

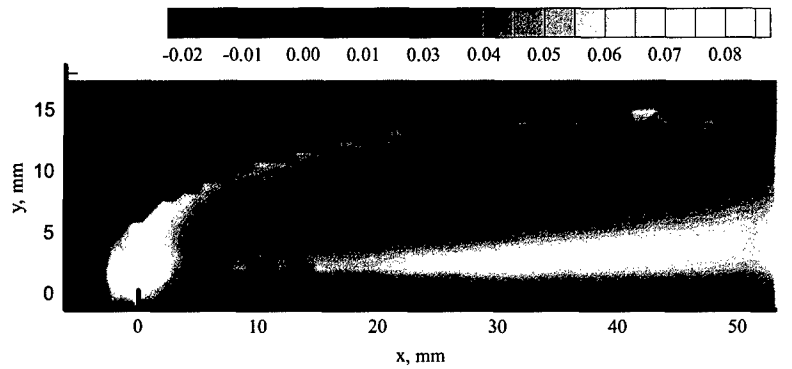

(a) z = 0

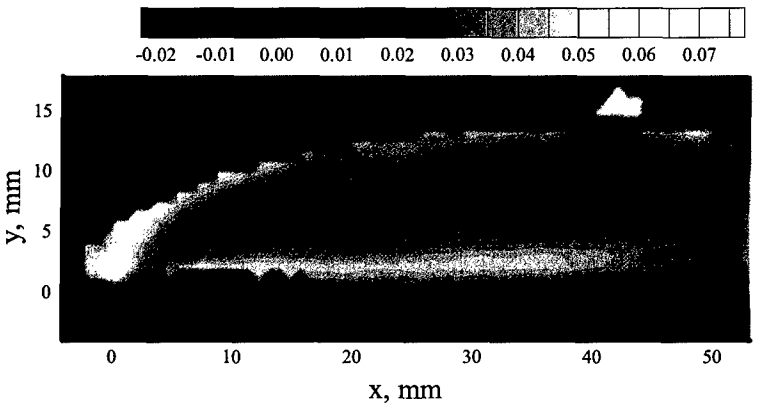

(b) z = 1.59 mm

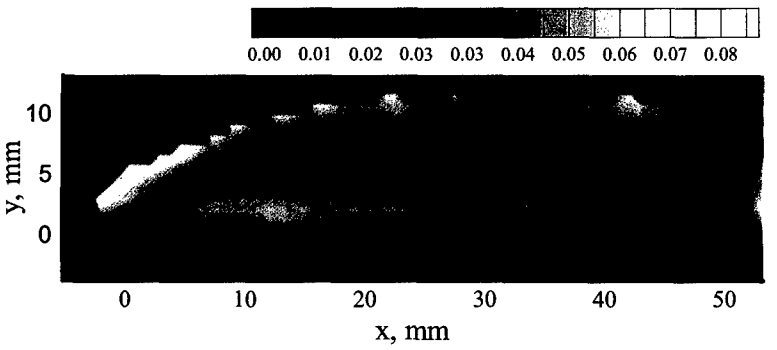

(c) z = 3.18 mm

Figure 58 Transverse Turbulence Intensity, $\sqrt{\overline{v'^2}}/u_\infty$ (Model M1A, MPR = 0.006)

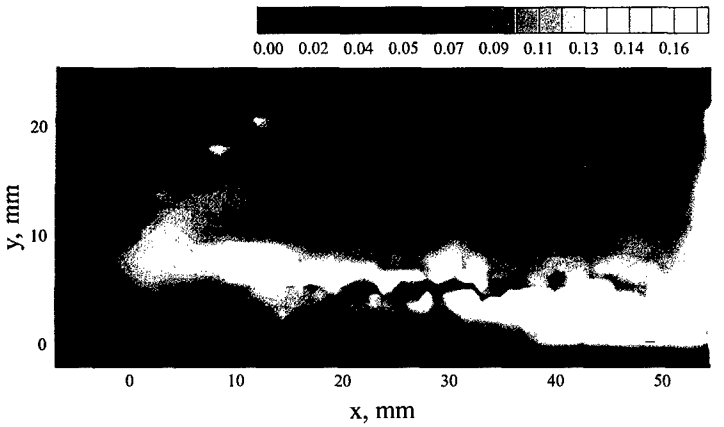

(a) z = 0

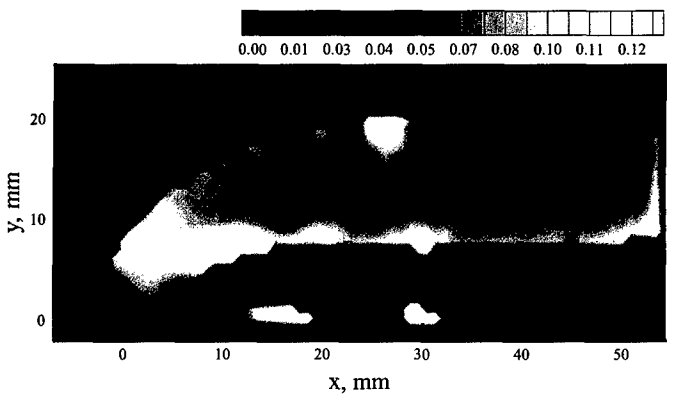

(b) z = 1.59 mm

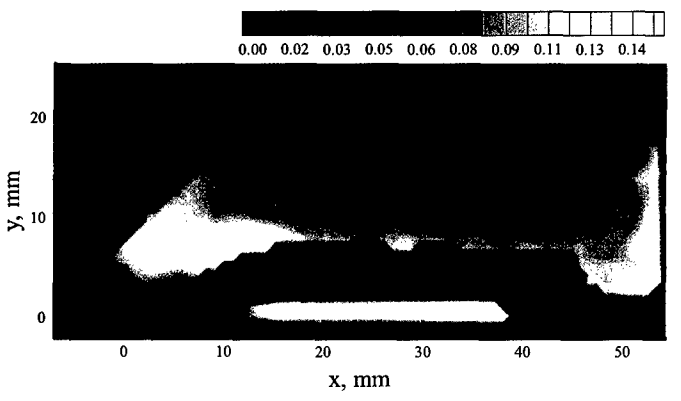

(c) z = 3.18 mm

Figure 59 Axial Turbulence Intensity, $\sqrt{\overline{u'^2}}/u_\infty$ (Model M3A-LP, MPR 0.06)

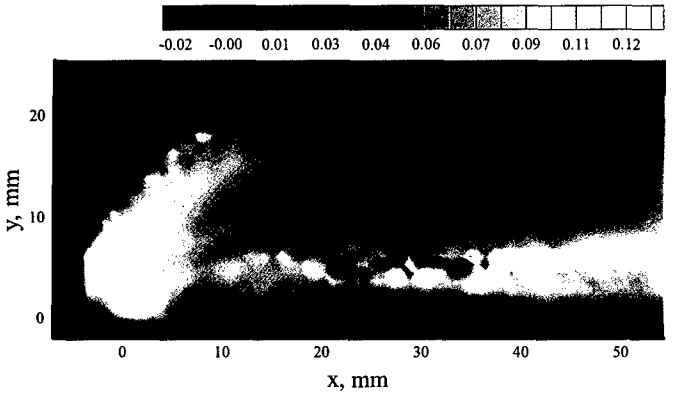

(a) z = 0

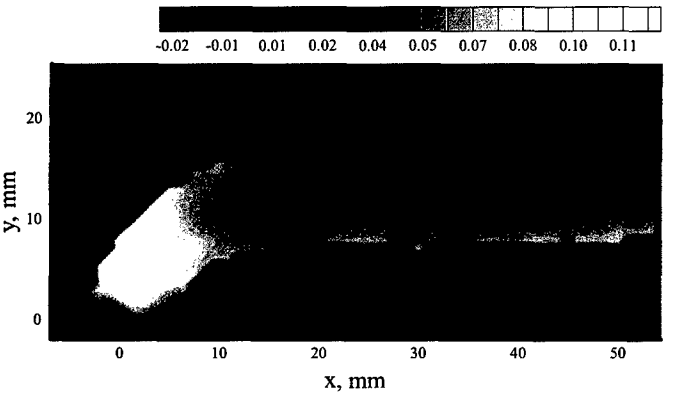

(b) z = 1.59 mm

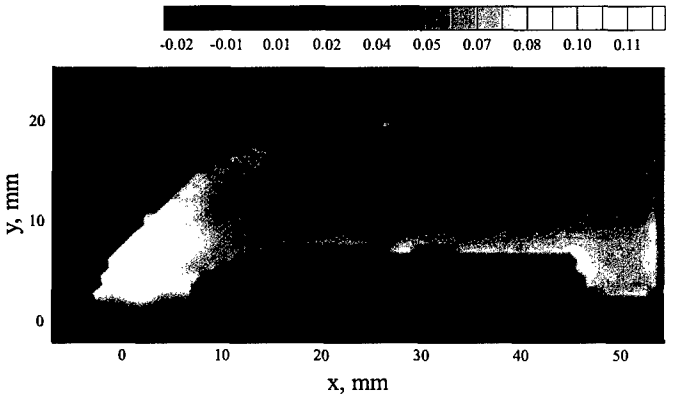

(c) z = 3.18 mm

Figure 60 Transverse Turbulence Intensity, $\sqrt{\overline{v'^2}}/u_\infty$ (Model M3A-LP, MPR 0.06)

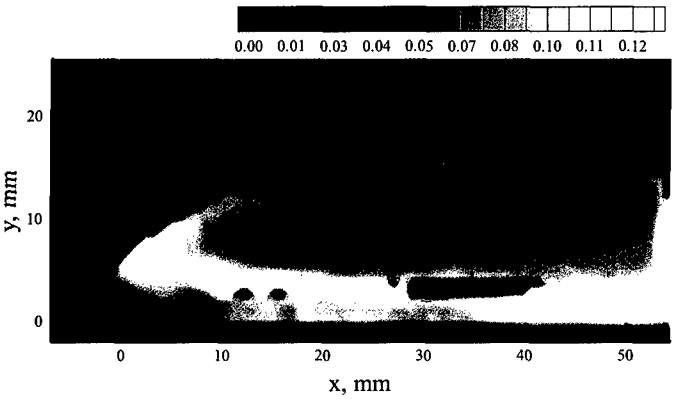

(a) z = 0

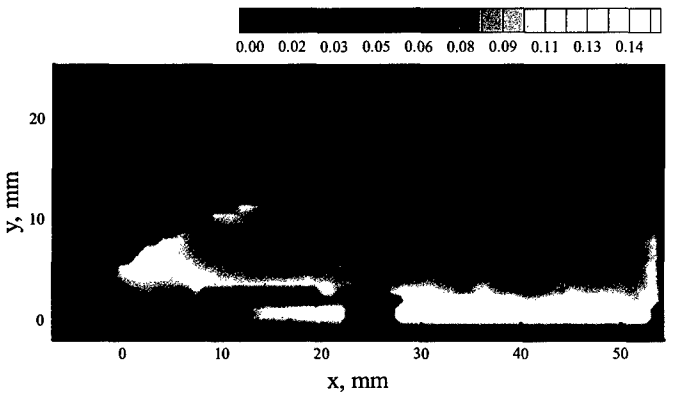

(b) z = 1.59 mm

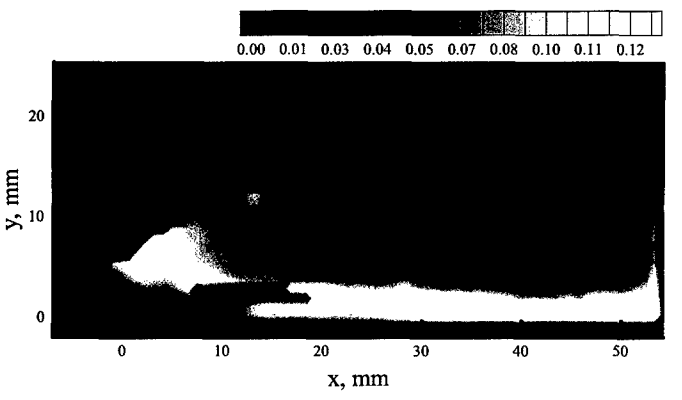

(c) z = 3.18 mm

Figure 61 Axial Turbulence Intensity, $\sqrt{u'^2}/u_\infty$ (Model M3A-LP, MPR 0.03)

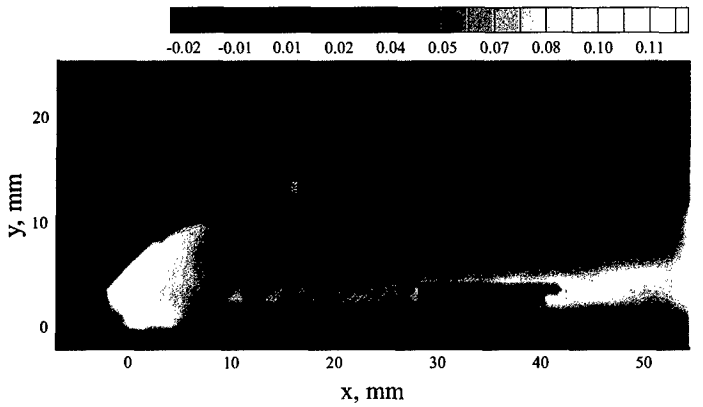

(a) z = 0

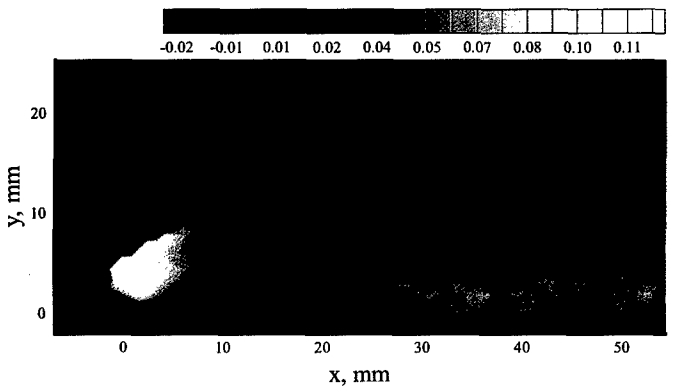

(b) z = 1.59 mm

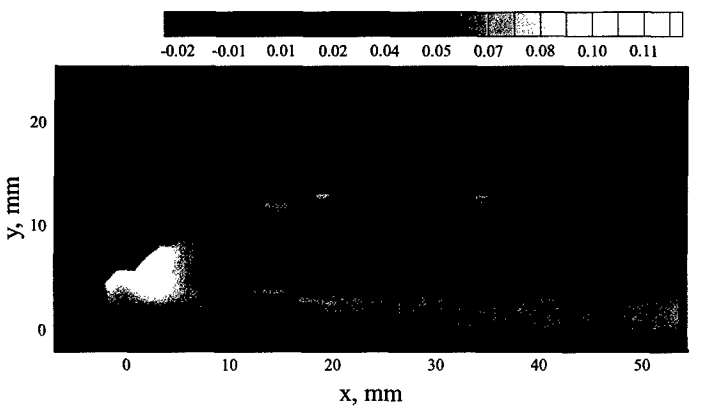

(c) z = 3.18 mm

Figure 62 Transverse Turbulence Intensity, $\sqrt{\overline{v'^2}}/u_\infty$ (Model M3A-LP, MPR 0.03)

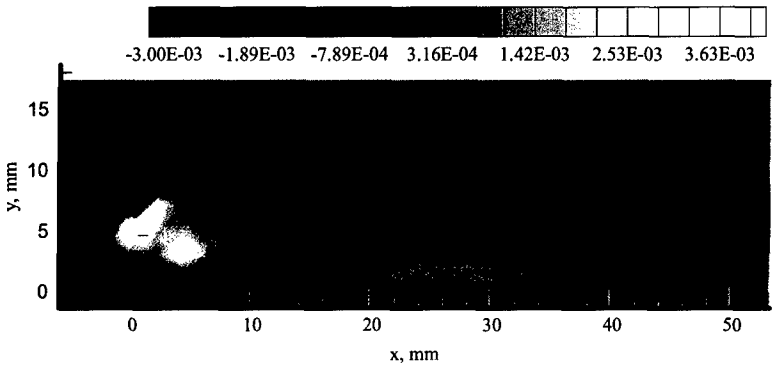

(a) z = 0

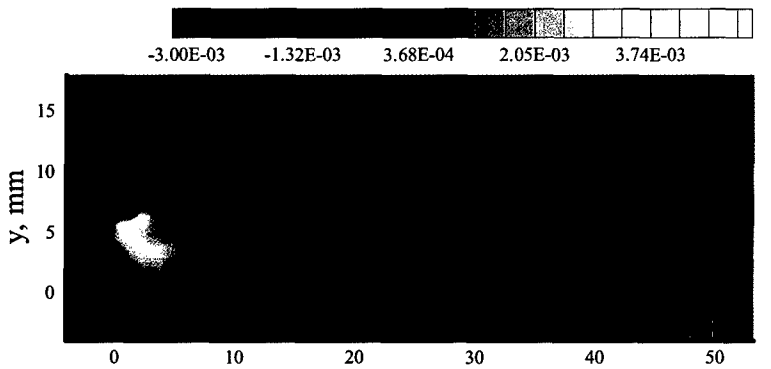

(b) z = 1.59 mm

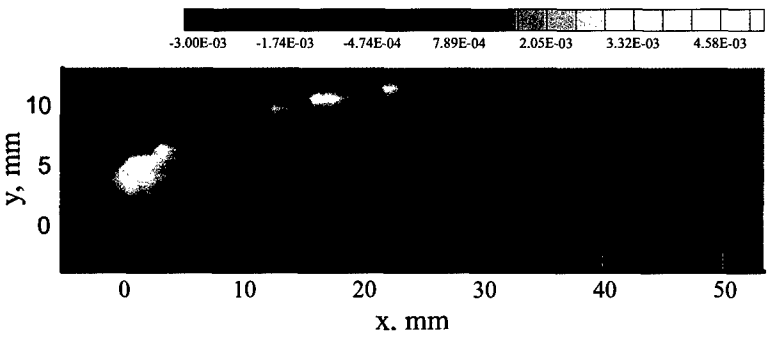

(c) z = 3.18 mm

Figure 63 Reynolds Stress, $\overline{u'v'}/u_\infty^2$ (Model M1A, MPR 0.006)

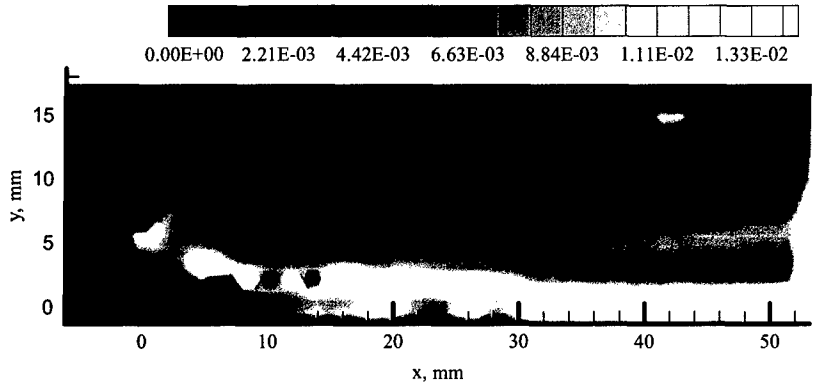

(a) z = 0

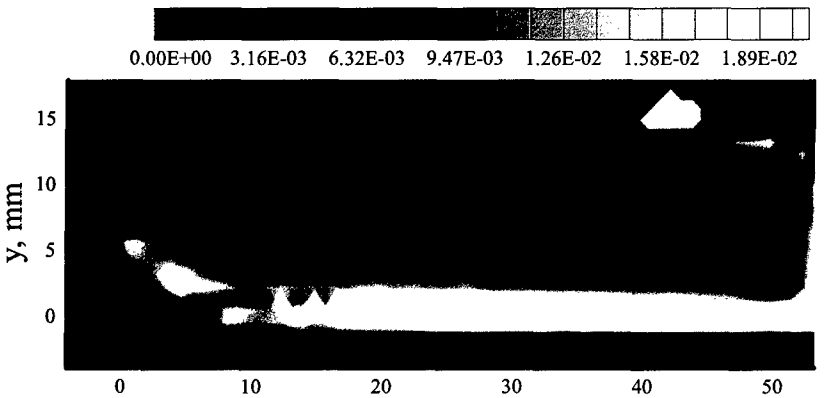

(b) z = 1.59 mm

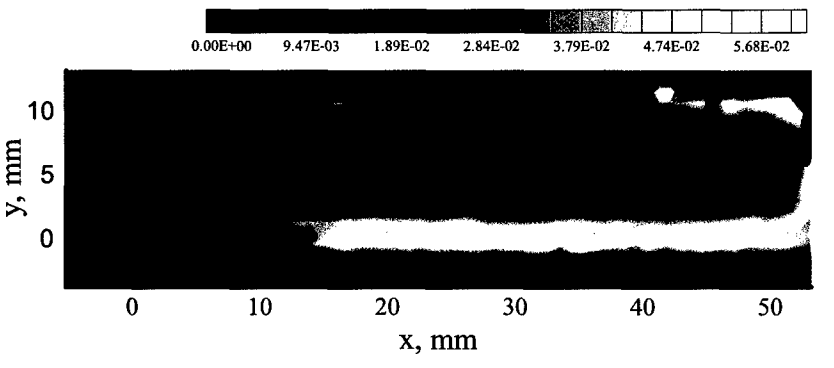

(c) z = 3.18 mm

Figure 64 Axial Stress, $\overline{u'u'}/u_\infty^2$ (Model M1A, MPR 0.006)

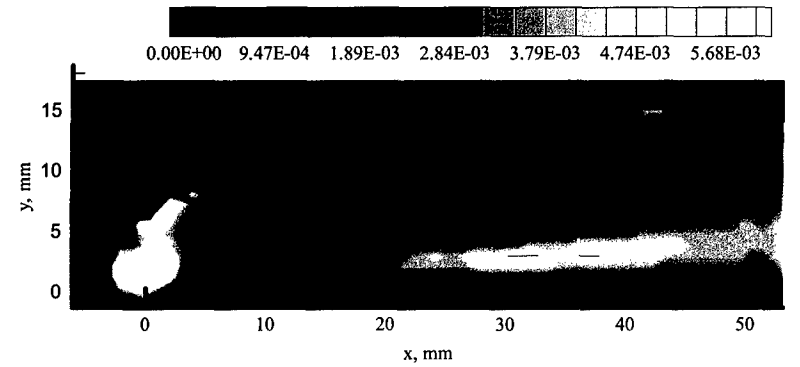

(a) z = 0

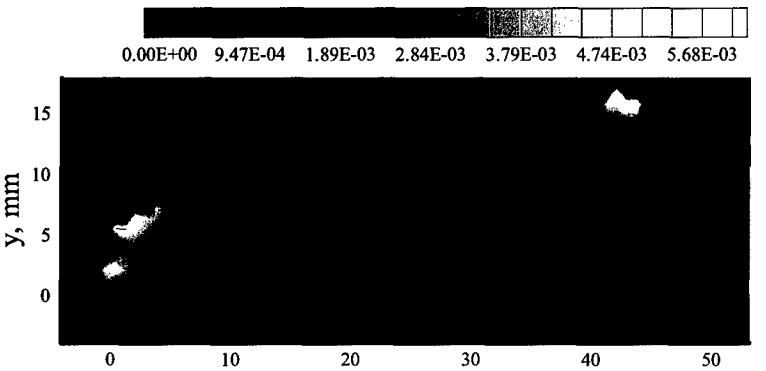

(b) z = 1.59 mm

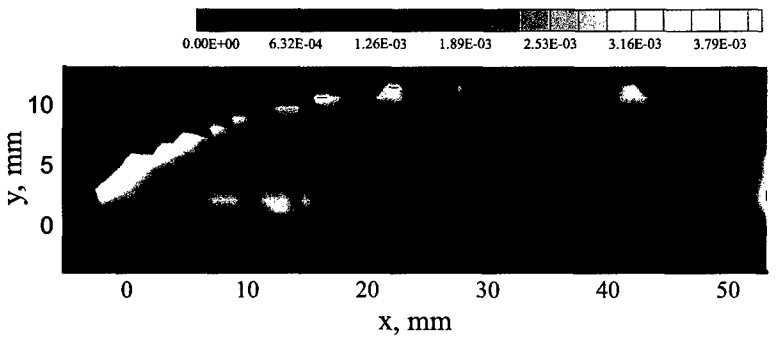

(c) z = 3.18 mm

Figure 65 Transverse Stress, $\overline{v'v'}/u_\infty^2$ (Model M1A, MPR 0.006)

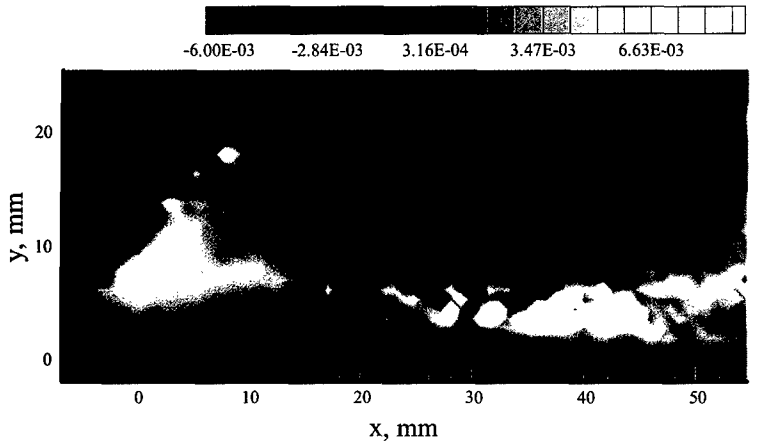

(a) z = 0

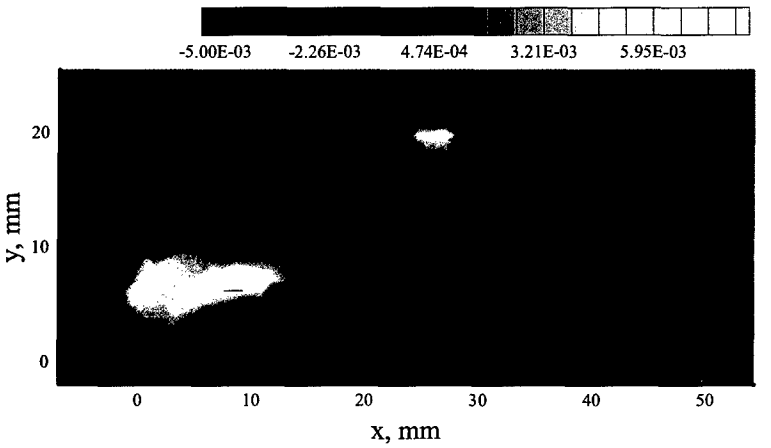

(b) z = 1.59 mm

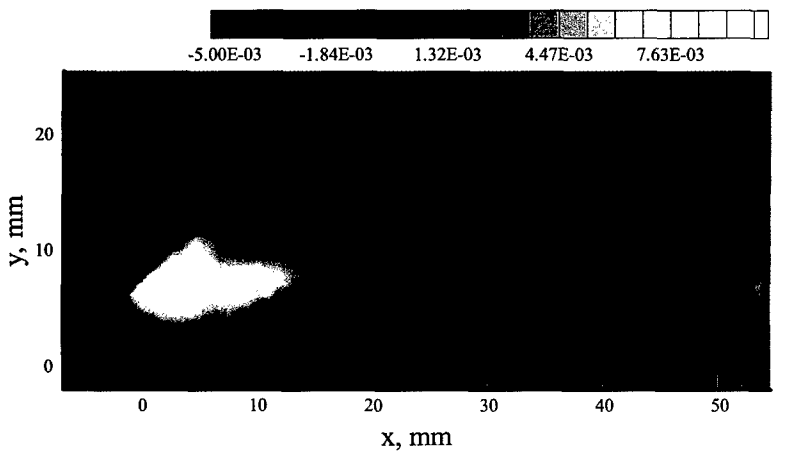

(c) z = 3.18 mm

Figure 66 Reynolds Stress, $\overline{u'v'}/u_\infty^2$ (Model M3A-LP, MPR 0.06)

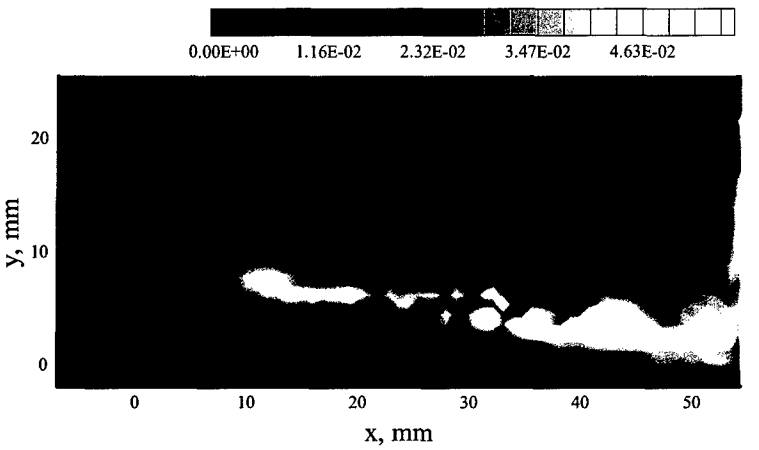

(a) z = 0

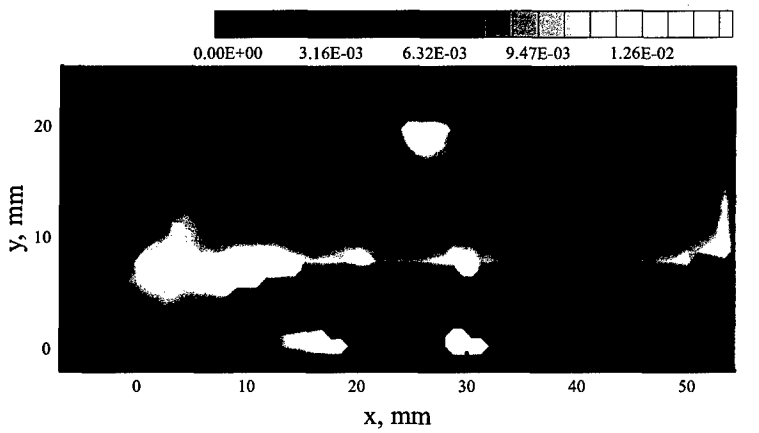

(b) z = 1.59 mm

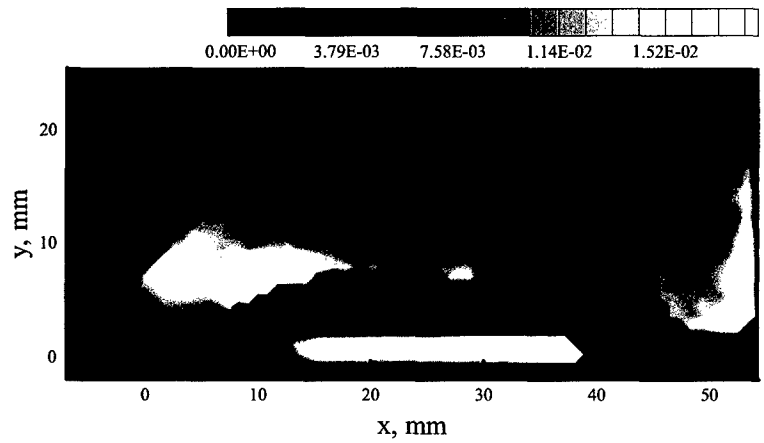

(c) z = 3.18 mm

Figure 67 Axial Stress, $\overline{u'u'}/u_\infty^2$ (Model M3A-LP, MPR 0.06)

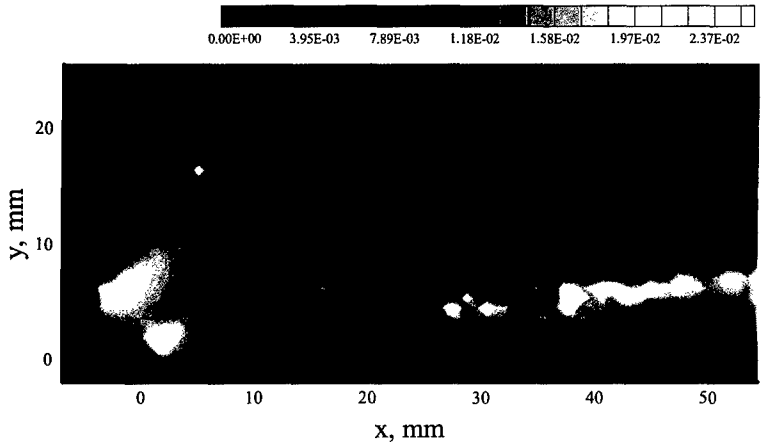

(a) z = 0

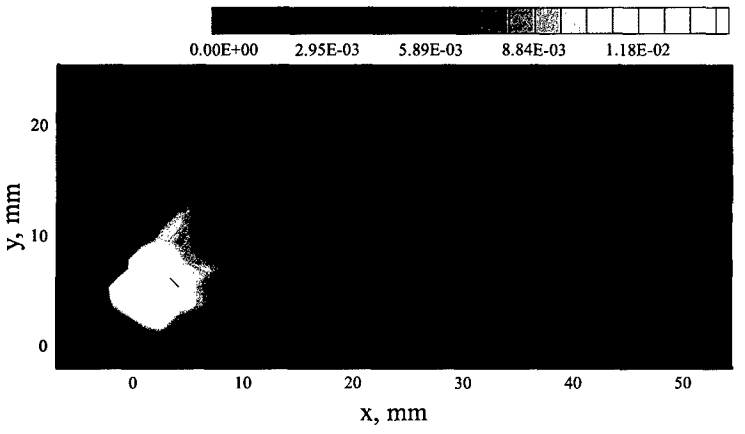

(b) z = 1.59 mm

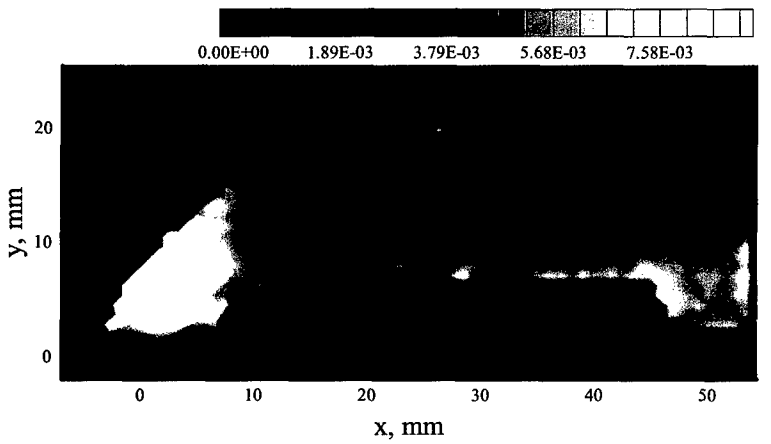

(c) z = 3.18 mm

Figure 68 Transverse Stress, $\overline{v'v'}/u_\infty^2$ (Model M3A-LP, MPR 0.06)

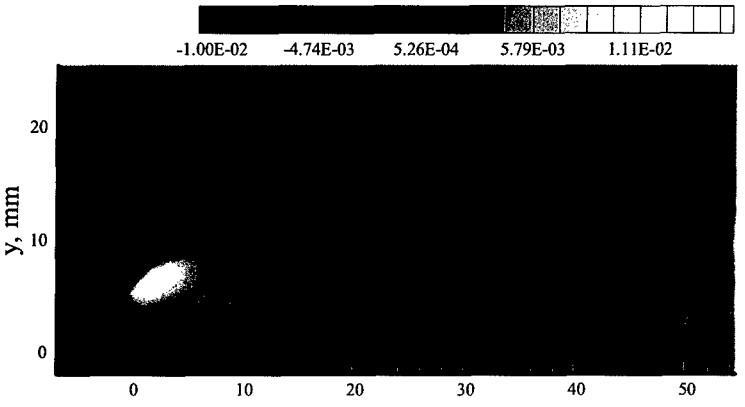

(a) z = 0

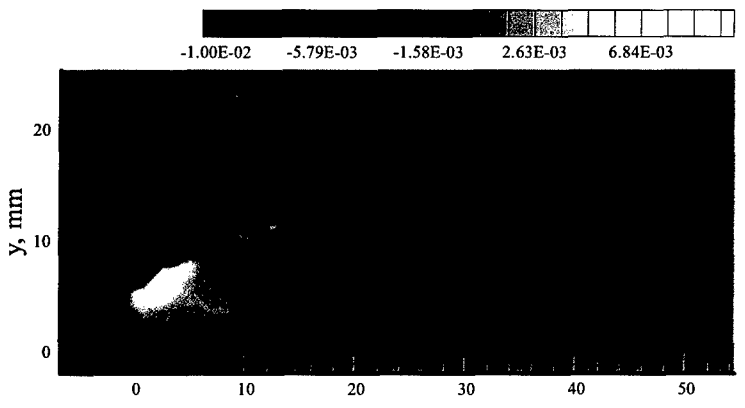

(b) z = 1.59 mm

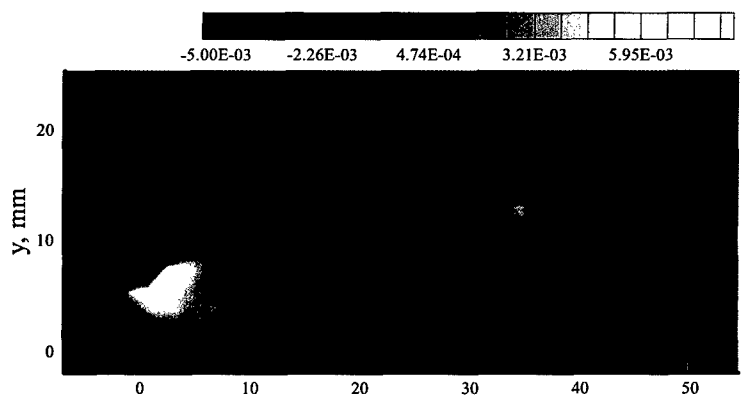

(c) z = 3.18 mm

Figure 69 Reynolds Stress, $\overline{u'v'}/u_\infty^2$ (Model M3A-LP, MPR 0.03)

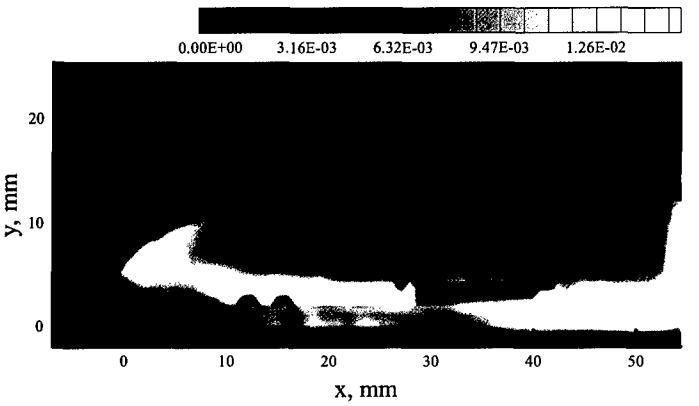

(a) z = 0

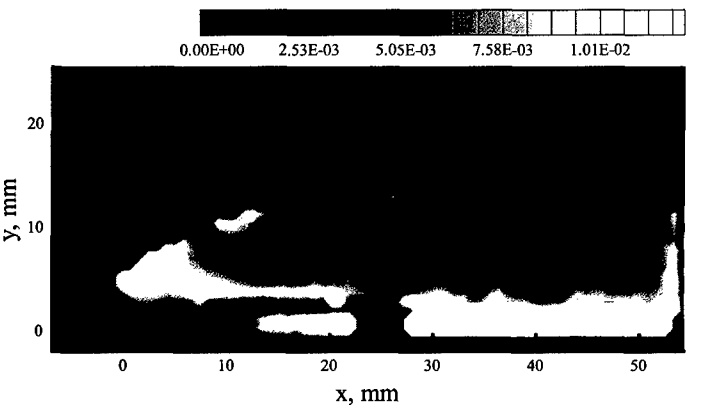

(b) z = 1.59 mm

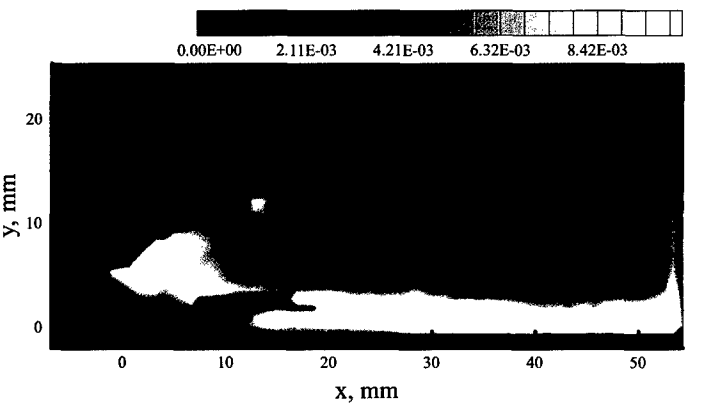

(c) z = 3.18 mm

Figure 70 Axial Stress, $\overline{u'u'}/u_\infty^2$ (Model M3A-LP, MPR 0.03)

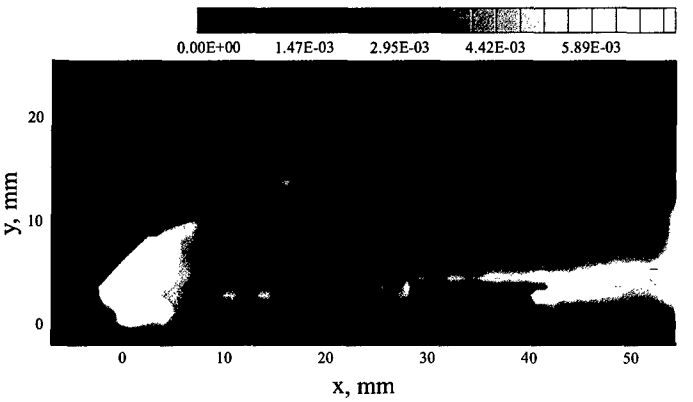

(a) z = 0

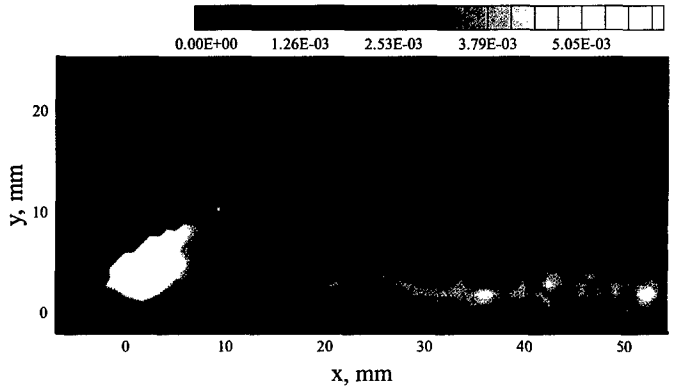

(b) z = 1.59 mm

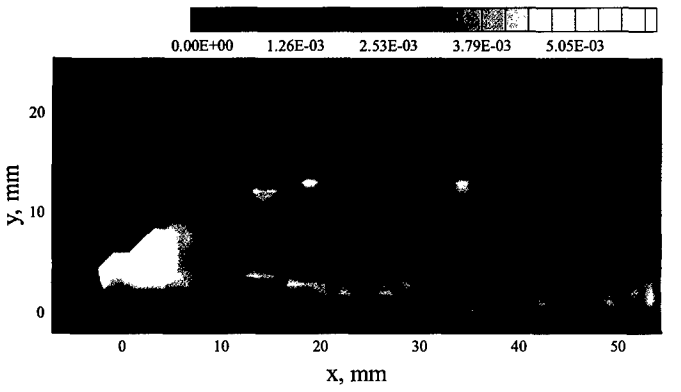

(c) z = 3.18 mm

Figure 71 Transverse Stress, $\overline{v'v'}/u_\infty^2$ (Model M3A-LP, MPR 0.03)

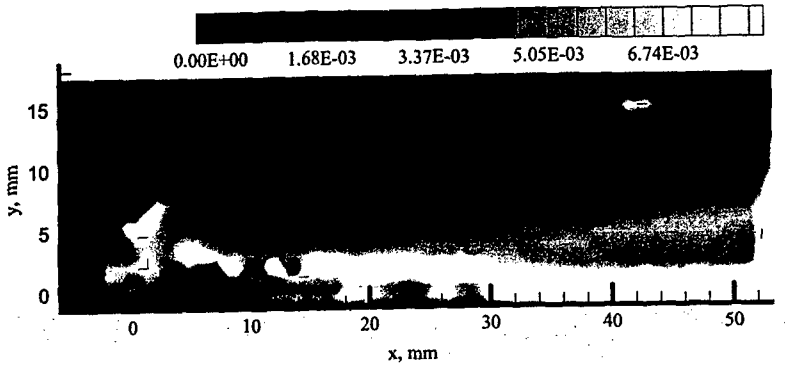

(a) z =0

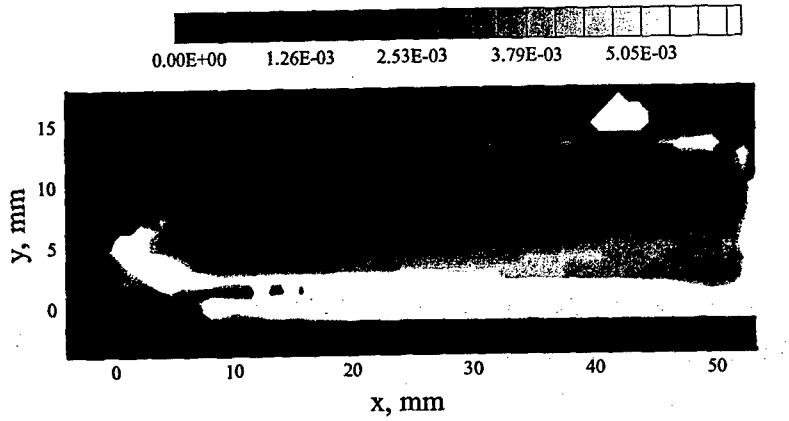

(b) z = 1.59 mm

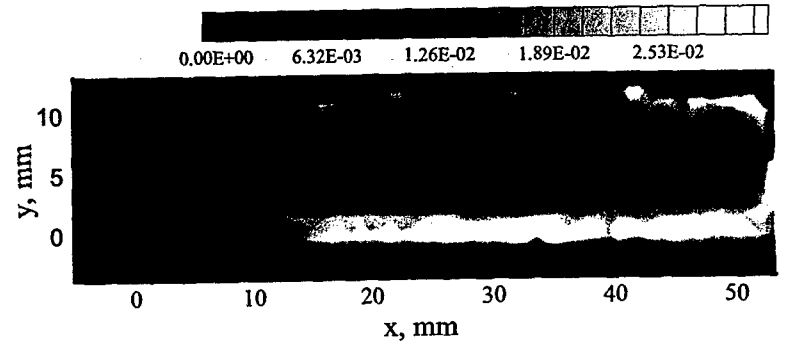

(c) z = 3.18 mm

Figure 72 TKE, $(\overline{u'^2}+\overline{v'^2})/2u_\infty^2$ (Model M1A, MPR 0.006)

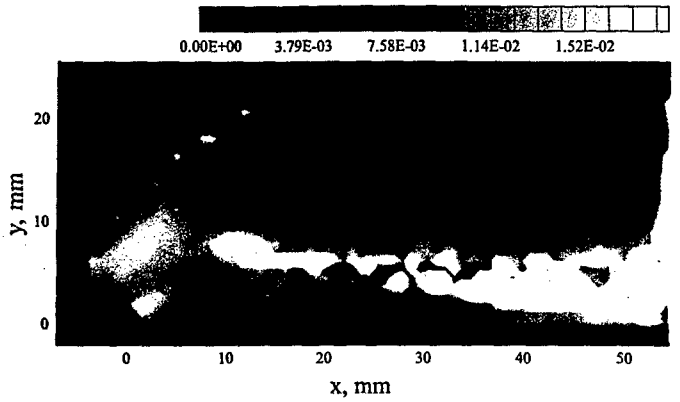

(a) z = 0

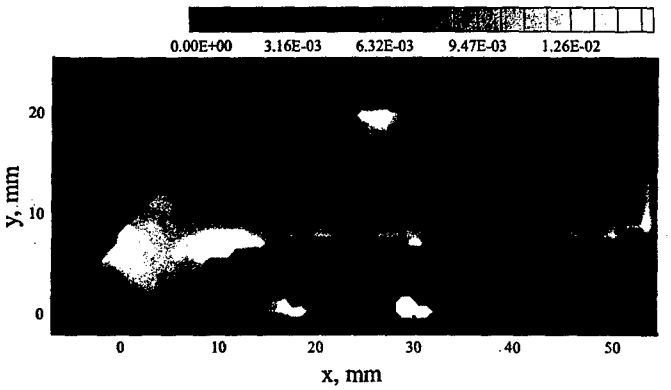

(b) z = 1.59 mm

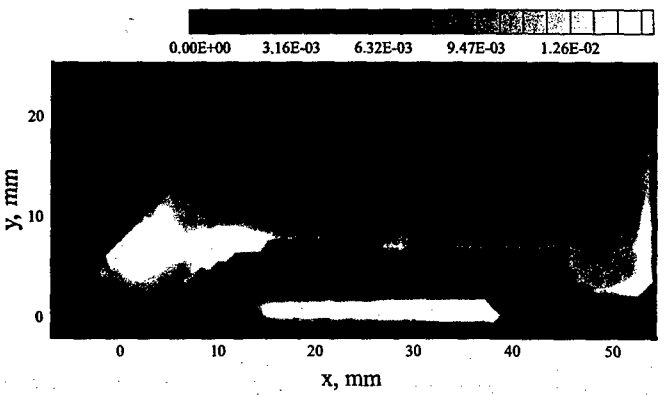

(c) z = 3.18 mm

Figure 73 TKE, $(\overline{u'^2}+\overline{v'^2})/2u_\infty^2$ (Model M3A-LP, MPR 0.06)

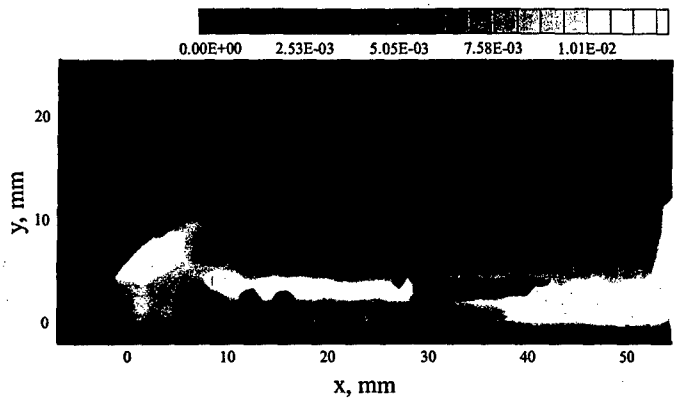

(a) z = 0

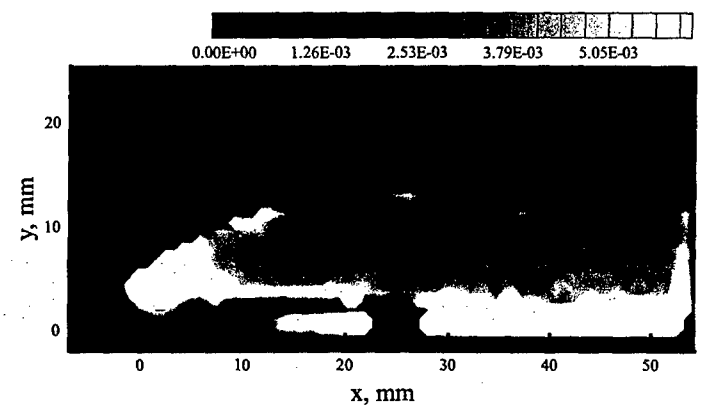

(b) z = 1.59 mm

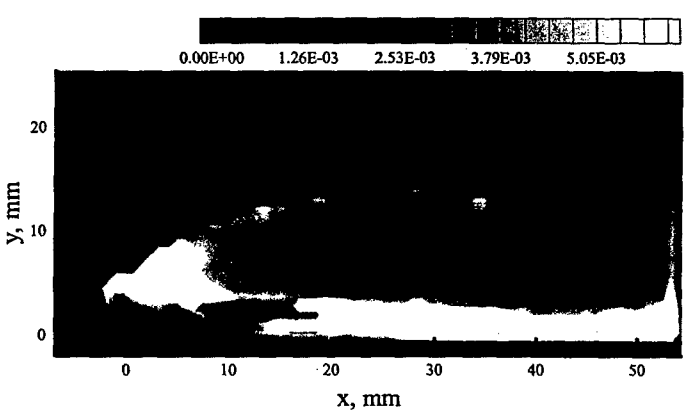

(c) z = 3.18 mm

Figure 74 TKE, $(\overline{u'^2}+\overline{v'^2})/2u_\infty^2$ (Model M3A-LP, MPR 0.03)

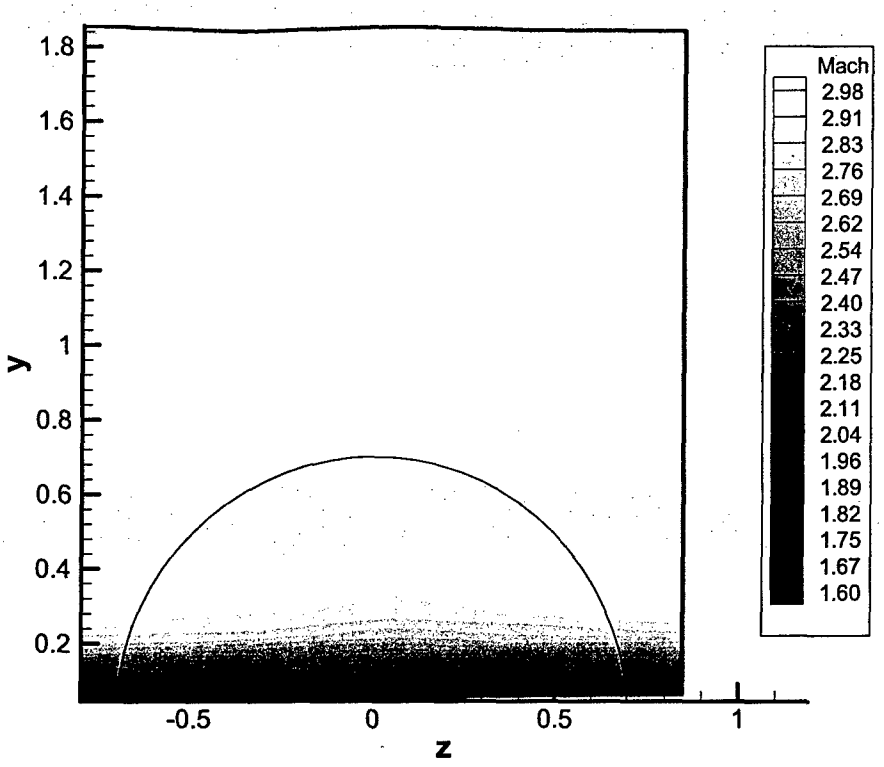

Figure 75 Freestream Mach Number Contour